MODEL STUDIES FOR THE DESIGN OF AN OPEN- OR CLOSED-JET WATER TUNNEL

by

St. Anthony Falls Hydraulic Laboratory
University of Minnesota

Project Report No. 22

Submitted by
Lorenz G. Straub
Director

Prepared by
James S. Holdhusen

June, 1950

Prepared for the
David Taylor Model Basin
Department of the Navy
Washington, D. C.

Bureau of Ships Contract NObs-34208
Task Order 3

PREFACE

Contract NObs-34208 between the University of Minnesota and the Bureau of Ships, Department of the Navy, provides for making hydrodynamic studies in compliance with specific task orders issued by the Taylor Model Basin calling for services to be rendered by the St. Anthony Falls Hydraulic Laboratory. Certain of these task orders related to experiments on a model of a 24-in. water tunnel designed at the Taylor Model Basin.

The findings of these studies relating to the 24-in. water tunnel are embodied in this report, which was written by the project leader, James S. Holdhusen, Instructor in Hydraulics, with the editorial assistance of Lois Fosburgh. The investigational program was under the general direction of Dr. Lorenz G. Straub, Director of the St. Anthony Falls Hydraulic Laboratory; and the experiments were performed under the guidance of John F. Ripken, Associate Professor of Hydraulics, who designed the model tunnel and reviewed the report. Mr. Holdhusen designed the test instruments and supervised the experimental program, which was carried out mainly by Clyde O. Johnson and Harry D. Purdy. The computations for the relaxation process were performed by Dr. C. S. Chao.

INTRODUCTION

In order to execute an experimental analysis of a proposed 24-in. water tunnel designed at the David Taylor Model Basin [1]*, a 1:4-scale model was constructed and tested at the St. Anthony Falls Hydraulic Laboratory of the University of Minnesota. This model was essentially a modified form of the 1:10-scale model of a 60-in. water tunnel previously tested at the St. Anthony Falls Hydraulic Laboratory. The main modifications were made between the downstream end of the contraction and the elbow leading into the pump assembly; the remaining part of the tunnel circuit was modified only by a change in the length of the 18-in. connecting conduit.

The experimental studies were conducted in a similar manner to those of this previous project, and references will be made to both the text and illustrations of the six project reports [2-7] which deal with the model of the 60-in. water tunnel and which contain a more thorough description of apparatus and test procedure than this report.

The experimental program consisted essentially of determining the velocity and pressure distribution in the tunnel at different velocities of flow and with different test section boundary forms. The analysis of the experimental data permitted prediction of the operation of the prototype tunnel and served to indicate where the original design could be improved.

The model of the 24-in. tunnel was tested in the forms listed in Table I+. Throughout the report, these various tunnel forms will be indicated by the letter designation given in Table I in order to eliminate repeating the description of different test conditions.

---

*Numbers in brackets refer to corresponding numbers in the References, pp. 155 and 156.

+All tables are included at the end of the report, pp. 144 to 154.

Page

PART VII. PUMP STUDIES 123
A. Introduction 123
B. Head, Discharge, and Power Requirements 123
C. Velocity Distribution 125
D. Cavitation and Static Pressure 126
E. Temperature of the Tunnel 128
F. Conclusions 131

Appendix 137
Tables 144
References 155

LIST OF FIGURES

Figure		Page
1	Sketch of Original Design of Proposed Prototype Water Tunnel	10
2	Sketch of Revised Design of Proposed Prototype Water Tunnel	10
3	View of Model Water Tunnel	11
4	Model Water Tunnel and Control Tower	12
5	Schematic Drawing of Water Tunnel Model (Tunnel Forms A and C)	13
6	Model Contraction Dynamometer Shaft Installation (Tunnel Form B)	14
7	Intersection of Contraction Dynamometer Shaft with Vaned Elbow IV (Tunnel Form B)	15
8	Intersection of Contraction Dynamometer Shaft with Vaned Elbow IV (Tunnel Form H)	16
9	Struts Used to Support Dynamometer Shaft	17
10	Detail of Open-Jet Test Section Showing Pick-Up Cone (Tunnel Form A)	18
11	Detail of Open-Jet Test Section Showing Adjusting Ring and Contraction Exit (Tunnel Form A)	19
12	Dimensions of Lucite Closed-Jet Test Section (Tunnel Form C)	20
13	Pitot Cylinder in Lucite Closed-Jet Test Section (Tunnel Form C)	21
14	Aluminum Closed-Jet Test Section (Tunnel Form C)	22
15	Diffuser Transition Boundary in Model and Revised Prototype Tunnel	23
16	Model Tunnel with 9° Main Diffuser (Tunnel Form D)	24
17	Model Diffuser Dynamometer Shaft Installation (Tunnel Form F)	25
18	Nose and Supporting Struts of Diffuser Dynamometer Shaft (Tunnel Form F)	26
19	Detail of Supports for Diffuser Dynamometer Shaft	27
20	Faired Splitter in Vaned Elbow I	28
21	Designation of Traverse Stations and Components of Model Tunnel	29
22	Velocity and Pressure Measuring Instruments	30
23	Turbulence Sphere Test Section Mounting	31
24	Pressure Distribution along Contraction Boundary	40
25	Contraction Head Loss Coefficient (Computed from Calibration Data)	40
26	Suggested Design of Open-Jet Test Section to Provide Uniform Velocity and Pressure in Jet Core	65

Figure | Page

27 Model Open-Jet Test Section with 6 5/8-in. Pick-Up Cone and the Contraction Dynamometer Shaft Extension Used for Measuring Axial Pressure Variation 66

28 Model Open-Jet Test Section with 6 3/8-in. Pick-Up Cone 67

29 Axial Pressure Variation in Open-Jet Test Section with 6 5/8-in. Pick-Up Cone 68

30 Axial Pressure Variation in Open-Jet Test Section with 6 3/8-in. Pick-Up Cone 69

31 Velocity Distribution at Station 1 with and without the Contraction Dynamometer Shaft 70

32 Velocity Distribution at Station 2 with and without the Contraction Dynamometer Shaft 70

33 Velocity Distribution at Station 3 with and without the Contraction Dynamometer Shaft 71

34 Velocity Distribution in Test Section in the Wake of Contraction Dynamometer Shaft Support Struts 72

35 Theoretical Distribution of Longitudinal Velocities in Diffusion Region of Open-Jet Test Section 73

36 Theoretical Velocity Distributions at Traverse Stations in Model Open-Jet Test Section 74

37 Measured Velocity Distribution in Diffusion Region of Model Open-Jet Test Section 74

38 Critical Reynolds Number in Model Open-Jet Test Section as Determined by Turbulence Sphere 75

39 Severe Cavitation in the Diffusion Layer of the Model Open-Jet Test Section 76

40 High-Speed Photographs of Cavitation in the Diffusion Layer of the Open-Jet Test Section at Different Cavitation Indices (σ) 77

41 Theoretical Longitudinal Velocity Distribution in Closed-Jet Test Section and Diffuser Transition 94

42 Theoretical Radial Velocity Distribution in Diffuser Transition 94

43 Boundary Pressure Distribution in Closed-Jet Test Section and Diffuser Transition 94

44 Measured Velocity Distribution at Downstream End of Closed-Jet Test Section 95

45 Critical Cavitation Indices in Prototype Closed-Jet Test Section 96

46 Velocity Distribution at Station 4 with 6 5/8-in. Pick-Up Cone (Tunnel Form A) 109

47 Velocity Distribution at Station 4 with 6 5/8-in. Pick-Up Cone and Contraction Dynamometer Shaft (Tunnel Form B) 109

Figure		Page
48	Velocity Distribution at Station 4 with 6 3/8-in. Pick-Up Cone (Tunnel Form E)	109
49	Velocity Distribution at Station 5 (Tunnel Forms A and E) . . .	110
50	Velocity Distribution at Station 5 (Tunnel Forms B, F, and G) .	110
51	Velocity Distribution at Station 5 (Tunnel Forms C and D) . . .	110
52	Velocity Distribution at Station 6 (Tunnel Forms A and E) . . .	110
53	Velocity Distribution at Station 6 (Tunnel Forms B, F, and G) .	111
54	Velocity Distribution at Station 6 (Tunnel Forms C and D) . . .	111
55	Velocity Distribution at Station 7 (Tunnel Forms A, D, and C) .	111
56	Velocity Distribution at Station 8 (Tunnel Form A)	111
57	Velocity Distribution at Station 11 (Tunnel Forms A, B, and H).	122
58	Velocity Distribution at Station 12 (Tunnel Forms A, J, and I).	122
59	Velocity Distribution at Station 12 (Tunnel Forms B and H) . .	122
60	Head-Discharge Curves for Prototype Water Tunnel	132
61	Pump Rating Curves and Head-Discharge Curves of Prototype Tunnel	133
62	Maximum Allowable Pressure in Prototype Test Section	134
63	Temperature Rise of Prototype Tunnel during Operation	135
64	Decrease in Temperature during Cooling of Prototype Tunnel . .	136
65	Values of ψ in the Region of the Diffuser Transition as Determined by the Relaxation Method	143

PART I. DESCRIPTION OF APPARATUS AND TEST PROCEDURES

A. Model Water Tunnel Components

The prototype water tunnel as originally designed is shown in Fig. 1; the first forms of the model tested corresponded to this design except for some discrepancies in the vicinity of the pump. Figure 2 is a drawing of the final revised design of the prototype tunnel. Figures 3 and 4 are photographs and Fig. 5 is a drawing of the 1:4-scale model of the proposed 24-in. water tunnel in its original test form. This model was constructed mainly from components of a 1:10-scale model of a 60-in. water tunnel [2]*. Referring to Fig. 5, the following parts of the present model were taken from the 60-in. tunnel model: the pump drive, the pump assembly, the pump diffuser, all of the vaned elbows except the one following the main diffuser, the contraction, the two sections of 18-in. diameter conduit with air traps, and the base frame (not shown in Fig. 5). All other components of the present model, including the test sections and main diffusers, were specially constructed for these experiments. The contraction and the metal parts of the test section are of aluminum, and the bulk of the remaining tunnel conduits are of steel.

The pressure measurement and control mechanism for the model of the 24-in. tunnel were the same as were used in the model of the 60-in. water tunnel, except for the addition of Lucite cylinders above each of the three manifold rings at the contraction to facilitate air drainage in the lines. The two systems are fully described in reference [2].

1. Contraction

The contraction as used in the previous model studies for the 60-in. closed-jet tunnel had to be slightly modified in order to install the open-jet test section. The modification consisted of machining off the downstream flange, shaping the exterior of the downstream end of the casting to the required boundary shape of the open-jet chamber (Fig. 5), and providing exterior threads for attachment to the test section. Two aluminum end plates for the open-jet test section were machined to the contours designated by the design, and one of these was threaded to screw onto the end of the contraction. After preliminary assembly, the aluminum-to-aluminum threads were found to have

---

*Numbers in brackets refer to the corresponding numbers in the Bibliography, pp. 156 and 157.

seized, and the plate had to be forced off. This in turn warped the downstream end of the contraction slightly so that this portion of the contraction had to be remachined. A steel spacer ring was then constructed to fit between the aluminum plate and the contraction so that there were no aluminum-to-aluminum threads. The change in shape resulting from the remachining was very small, as can be seen by comparing the boundary coordinates in column three, Table IV of this report, with the coordinates in Table III of reference [3]. In the tables, $\underline{x}$ represents the distance in inches in the model from the upstream end of the contraction and is measured positive in the downstream direction. Table IV of this report gives coordinates to one more significant figure than Table III of reference [3] because a specially built caliper was used in measuring the inside diameter.

Some of the tunnel tests were made with a mock-up of a dynamometer shaft housing passing through the contraction to the test section. The model shaft housing, called the contraction dynamometer shaft in this report, was constructed in accord with a Taylor Model Basin design so that its contour followed the theoretical stream surface of the contraction flow system whose diameter was equal to the shaft diameter at the downstream end of the contraction [1]. The dimensions of the shaft are given in Table II and Fig. 6. The shaft was turned from four lengths of steel rod plated with cadmium and screwed together. This installation was tested with two forms for the intersection of the shaft and the vaned elbow upstream of the contraction, as shown in Figs. 7 and 8. In the first form, the upstream portion of the shaft was 1.125 inches in diameter and passed through an aluminum sleeve 1 1/2 inches in diameter and 6 in. long, which was threaded through the guide vanes of the vaned elbow. In the second form of the installation, shellacked wooden forms were placed over the 1.125-in. portion of the shaft and over the aluminum sleeve so that the shaft was effectively of constant diameter from the point where it pierced the tunnel to the point where it is of 2.437-in. diameter, as shown in Fig. 6.

The shaft was supported in the model by two sets of struts, each set consisting of three struts spaced 120° apart. One set of struts was located in the stilling length upstream of the contraction at $x = -2.0$ (Fig. 6). The dimensions of these struts, designated type I, are given in Fig. 9. The second set of struts, designated type II, were located at $x = +15.0$ and were slightly smaller than the type I struts (Fig. 9). All of the struts were installed so

that there was a clean intersection between the tunnel wall and struts and between the shaft housing and the struts.

2. Open-Jet Test Section

The open-jet test section (Figs. 10, 11, 27, and 28) consisted of a Lucite cylinder 15 inches in inside diameter and 9 5/16 in. long, which was held between two circular aluminum end plates. The cylinder was originally formed from 1/2-in. Lucite sheet and machined and polished to 3/8-in. thickness, but this shell did not withstand the combinations of stresses due to pressure, vibration, and thermal straining of the tunnel and was cracked and patched in several places after about eight months' use. A replacement cylinder was made from 3/4-in. Lucite sheet and machined and polished to 5/8-in. thickness; this test section cylinder remained undamaged during the remainder of the test program.

A Lucite hatch 6 inches in diameter (Fig. 5) was provided in the test section cylinder to permit access to the test section, and the hatch cover was clamped to a coaming by a brass clamp ring. The interior of the hatch cover was smoothly machined to the same 15-in. diameter as the main cylinder. The hatch cover and the test section cylinder were machined to permit insertion of a Pitot cylinder at three different axial distances from the contraction. Pitot cylinder traverses could be made along any desired diameter by rotating the test section cylinder within the end plates.

Two sizes of pick-up cones were used at the downstream end of the open-jet test section (Figs. 5, 10, and 27), one of 6 5/8-in. and the other of 6 3/8-in. throat diameter (Table I). Both cones were machined from aluminum castings and mounted on four aluminum adjusting posts which passed through the downstream end plate of the test section and engaged an external adjusting ring. The gap between the pick-up cones and the downstream end plate could be adjusted from 0 to 5/8 in. by turning the adjusting ring. The smaller cone was provided with an aluminum adapter to the diffuser which was designed to fit the larger cone. The larger cone, as well as the downstream end plate, was coated with a black oxide of aluminum to facilitate visual observation of cavitation.

3. Closed-Jet Test Section

The closed-jet test section and diffuser transition of the model water tunnel were originally machined of Lucite to the dimensions shown in

Fig. 12. The test section, which was cylindrical and 6 inches in diameter, was 2.76 in. long and corresponded to the original design of the prototype. Final adoption of a smaller pick-up cone in the open-jet prototype will permit the use of a longer closed-jet test section in the prototype. This longer closed-jet test section was not tested in the model because a reasonably accurate estimate of the change in performance could be made on an analytical basis.

Velocity traverses could be made at the downstream end of the Lucite test section using a 1/4-in. Pitot cylinder in ports provided in the walls (Fig. 13). The transition curve downstream of the test section (Fig. 12) could not be machined accurately enough in Lucite so that it was necessary to construct a new test section of aluminum (Fig. 14) in order to investigate the pressure distribution and cavitation characteristics. The surface of the aluminum test section was very smooth and the final machined radius of the transition was very close to the design radius at every point, the average measured error being less than 0.001 inch. Two diametrically opposed taps 1/32 inch in diameter drilled normal to the inner wall were located every 1/2 in. along the transition in order to measure the pressure distribution.

4. Diffusers

The diffuser following the test section, called the main diffuser in this report, was originally designed to have a total angle of divergence of 6° 40' and to be made up of three parts in the model. When the open-jet test section with the larger pick-up cone was installed in the tunnel, the first section of the diffuser was a part of the downstream end plate, directly downstream of the pick-up cone. This section of the diffuser was 15/16 in. long and was designed with ports so that traverses could be made using a 1/4-in. Pitot cylinder. The next section of the diffuser consisted of a Lucite cone 11 1/16 in. long, its largest diameter being 8 3/32 inches. This section was made of Lucite in order to facilitate observation of possible cavitation on the pick-up cone and diffuser throat. The main or downstream portion of the diffuser was rolled from 3/16-in. steel, welded, and galvanized without machining the inside boundary. Testing of the smaller pick-up cone necessitated lengthening the diffuser to make its throat diameter smaller. This was accomplished by installing an aluminum adapter between the Lucite section of the diffuser and the downstream end plate of the test section. Lengthening the diffuser made it necessary to insert a spacing ring in the lower leg of

the tunnel directly following the pump diffuser. Figure 4 shows the model tunnel with the 6° 40' diffuser and open-jet test section.

When the closed-jet test section was installed in the tunnel, the transition from test section to diffuser and the first section of the diffuser were contained in this component. The remaining two sections were the same as for the open-jet test sections.

The tunnel was also tested with a 9° total angle diffuser following the open-jet test section. This diffuser was constructed in one piece and was machined and cadmium plated internally along its entire length. The 9° diffuser was tested to determine whether separation in the diffuser of the then-existing 24-in. water tunnel at Taylor Model Basin was causing vibration of the tunnel. The model tests did not indicate any intermittent separation, nor was there any noticeable tendency toward vibration. The data on velocity distribution and energy loss for this diffuser are included in this report for comparative purposes. A section of cylindrical conduit 12 inches in diameter was placed between the 9° diffuser and the following vaned elbow to close the flow circuit. Figure 16 shows the model tunnel with the 9° diffuser.

A comparison of Figs. 1 and 5 shows that there is a diffuser in the vertical leg above the pump in the model water tunnel which will not appear in the prototype. It was necessary to install this diffuser in order that the approach conduit and pump assembly used in the model of the 60-in. water tunnel could be used for the present study. Also, the diffuser downstream of the pump is not a model of the prototype design. These discrepancies in the construction of the model were considered no less allowable than the discrepancy which exists between the model and prototype pumps; it is not believed that the discrepancies in the design of the connecting conduits or the pumps will noticeably affect the other tunnel components. The model diffusers upstream and downstream of the pump will be treated in this report, however, in order to give a complete description of the flow in the model. Both of these diffusers were rolled of 3/16-in. steel, welded, and galvanized without further machining except for removal of the weld bead.

In some tests, the 6° 40' diffuser following the test section was tested with a model dynamometer shaft and support system installed. Figure 17 shows the installation. This dynamometer shaft, called the diffuser dynamometer shaft, consisted of a stainless steel rod 13/16 inch in diameter and

was supported at its downstream end by an aluminum splitter in a vaned elbow. The upstream end of the shaft had a nosepiece 1 1/2 in. long whose tip was 3 1/2 in. from the end of the contraction (Fig. 18). The shaft was supported at two points inside the diffuser by sets of struts designated as type I in this report (Fig. 9), which were swept back 45° in the direction of flow to lessen their cavitation susceptibility. The installation was first tested with two struts in the lower half of the diffuser at each point of the support. The struts were spaced 45° on either side of the plane of symmetry of the tunnel. Later, tests were made with three struts at each point of support; these struts were spaced 120° apart, the vertical one being in the upper half of the diffuser. The supporting struts were fastened to an enlarged portion of the shaft which simulated the shape of the bearings for the dynamometer shaft (Fig. 19).

5. Vaned Elbows

The vaned elbows used in the model tunnel consisted of extruded aluminum vanes attached to cast-aluminum frames. The shape of the individual vanes and their orientation in the cascade are fully described in reference [6]. In all of the tests made in the present study, the stagger angle of the vanes was 100°, since it had been determined that this angle gave optimum flow conditions. Vaned elbows II, III, and IV (Fig. 21) are the same elbows that were used in the previous model study. A new vaned elbow to be used downstream of the main diffuser (vaned elbow I) was constructed for this study since the diameter of the approach conduit was 12 in., instead of 13.2 in. as in the previous model. This elbow contained 11 vanes and was bisected by a faired splitter of 1-in. nominal thickness, which was constructed to provide a fairing for the diffuser dynamometer shaft (Fig. 20). The splitter was formed from aluminum sheet and had its leading edge normal to the incoming flow and its trailing edge parallel to the vane cascade axis. The splitter in vaned elbow II had a thickness of 3 in. and served as a fairing for the pump drive shaft housing. Both the leading and trailing edges of this splitter were parallel to the vane cascade axis.

The contraction dynamometer shaft passed through vaned elbow IV with no fairing. Vaned elbow IV was tested with two forms of intersection of the contraction dynamometer shaft and the vane cascade, as noted previously. This elbow was also tested without the contraction dynamometer shaft, but with the aluminum sleeve remaining in the cascade in order to determine whether or not

the sleeve alone would seriously affect the flow when the shaft was removed. The elbow was also tested with a hemispherical nosepiece and conical tailpiece 3 1/2 in. long attached to the aluminum sleeve.

B. Test Apparatus and Procedures

The main portion of the experimental program involved determining the velocity distribution at different cross sections of the tunnel circuit and determining the tunnel axial pressure gradient at different rates of flow. For these purposes, 12 traverse stations (Fig. 21) were established in the flow circuit. The traverse stations in the open-jet and closed-jet test sections and at the entrance to the diffuser in the open-jet test section consisted of two diametrically opposed packing glands through which the 1/4-in. Pitot cylinder and Pitot tube could be inserted. The traverse stations in the remainder of the tunnel are described in reference [2].

Four instruments were used in making velocity traverses: 1/4-in. (Fig. 22d) and 3/8-in. (Fig. 22e) diameter "long" Pitot cylinders, 2 3/8 in. diameter "cantilevered" Pitot cylinder (Fig. 15, Ref. [2]) and a 1/4-in. diameter Pitot tube (Fig. 22a). The procedure in using the Pitot cylinders is described in reference [2]. In the present tests, the angular orientation of the Pitot cylinder with respect to the mean flow direction was determined by applying a small bubble level to the radial index arm (Fig. 22) when the Pitot cylinder axis was horizontal. When the Pitot cylinder axis was vertical, the Pitot cylinder was oriented by aligning the index arm by eye with a scribed line parallel to the mean flow direction. Since all of the Pitot instruments measured only the total head at a specific point in a cross section, the average static pressure at the station being traversed was subtracted from the measured total head to give the velocity head.

The 1/4-in. Pitot cylinder was used for making traverses at three stations in the open-jet test section, at the entrance to the diffuser downstream of the open-jet test section, and at one station in the closed-jet test section. Traverses at stations not in the test section were made with the 3/8-in. Pitot cylinders. The 1/4-in. Pitot tube was constructed especially for exploring the wakes, in the test section, of the struts which supported the contraction dynamometer shaft. Since traverses could only be made on a diameter in the test section, no information concerning the lateral extent of the wakes was obtainable from a traverse using a Pitot cylinder. The Pitot

tube, however, could be rotated about the axis of support up to 15° on either side of the position where the nose was pointed directly upstream and still could give reliable values of the velocity distribution. The end of the nose of the Pitot cylinder was 2 1/8 in. from the axis of rotation; a traverse could thus cover a width of 1.1 in., which included the entire width of a wake in the test section. The error incurred in having the Pitot head at an angle to the approach flow was corrected by calibrating the Pitot tube in a region of the jet where uniform flow existed.

The pressure difference between traverse stations was measured using a 50-in. U-tube manometer with four gage fluids: carbon tetrachloride, ethylene bromide, Merriam No. 3 gage fluid, and mercury. The pressure differences were used in computing head loss coefficients for the components of the tunnel. The diameter of the conduit at each station and the square of the ratio of the cross-sectional area of each station to the area of a section 6 inches in diameter are given in Table III. In all cases where necessary, the cross-sectional area ratio has been corrected to take into account the presence of shafts on the axis of the conduit.

A special extension to the contraction dynamometer shaft was made in order to measure the axial pressure gradient in the open-jet test section. This extension was a cadmium-plated steel cylinder 0.812 inches in outside diameter and having a 0.153-in. wall which was pierced by 29 holes 1/32 inch in diameter spaced every 3/8 in. along the extension (Figs. 22b and 27). A plunger with two O-rings (Fig. 22c) was constructed so that by moving the plunger in 3/8-in. increments, only one of the holes in the dynamometer shaft extension was between the two O-ring seals. The pressure at the tap opposite the plunger was conducted to an external manometer by a 3/8-in. metal tube extending through the center of the hollow dynamometer shaft.

A turbulence sphere was used to determine the critical Reynolds number, and thus to define the amount of turbulence, of the open-jet test stream. The installation (Fig. 23) consisted of a 1-in. diameter Monel ball bearing which was supported by a 1/4-in. diameter stainless steel sting 2 in. long. This 1/4-in. tubing was pierced by two 1/32-in. diameter holes at its juncture with the sphere so that the static pressure in the wake could be measured. Inside the 1/4-in. tubing was a length of 1/8-in. tubing which was connected to a 1/32-in. hole at the stagnation point of the sphere. The pressure in

these two tubes was led through a 3/4-in. diameter brass sting support and out through the two packing glands in the downstream end plate of the open-jet test section which were also used for making velocity traverses at the entrance to the diffuser. The drag of the installation was transmitted to a 1/8- by 1-in. streamlined strut at the entrance to the diffuser. Vibration of the system was originally restricted by two lengths of piano wire which were fastened to the sting support and to the downstream end plate. These wires proved to be too weak, however, and were replaced by two 1/4-in. rods normal to the flow which were fastened to the test section cylinder and the nose of the sting support.

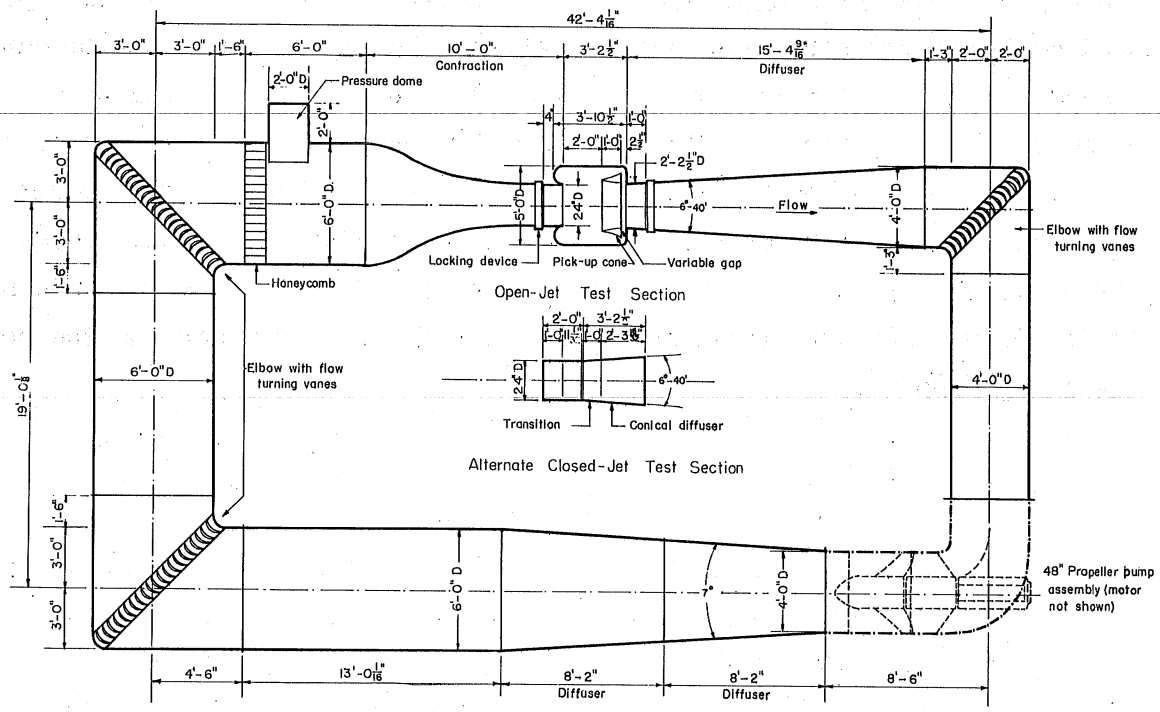

Fig. 1 - Sketch of Original Design of Proposed Prototype Water Tunnel

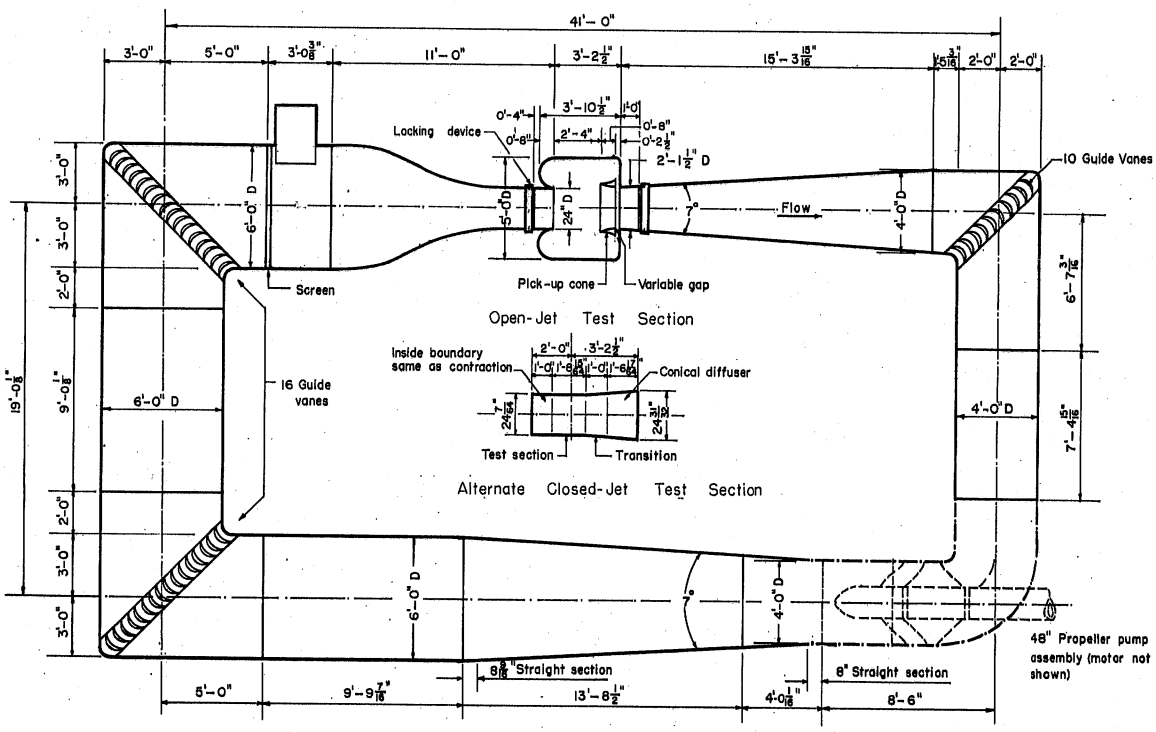

Fig. 2 - Sketch of Revised Design of Proposed Prototype Water Tunnel

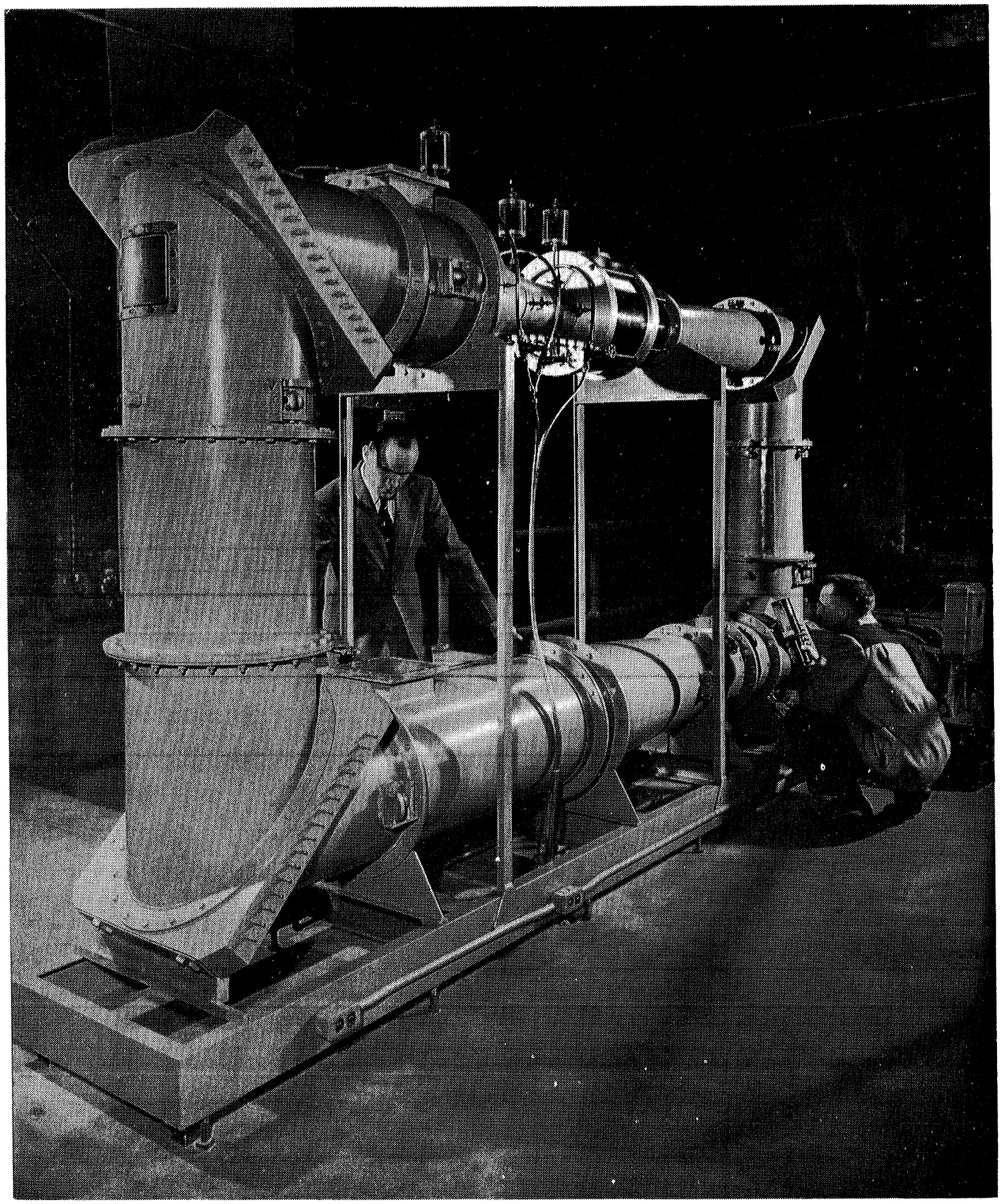

Fig. 3 - View of Model Water Tunnel

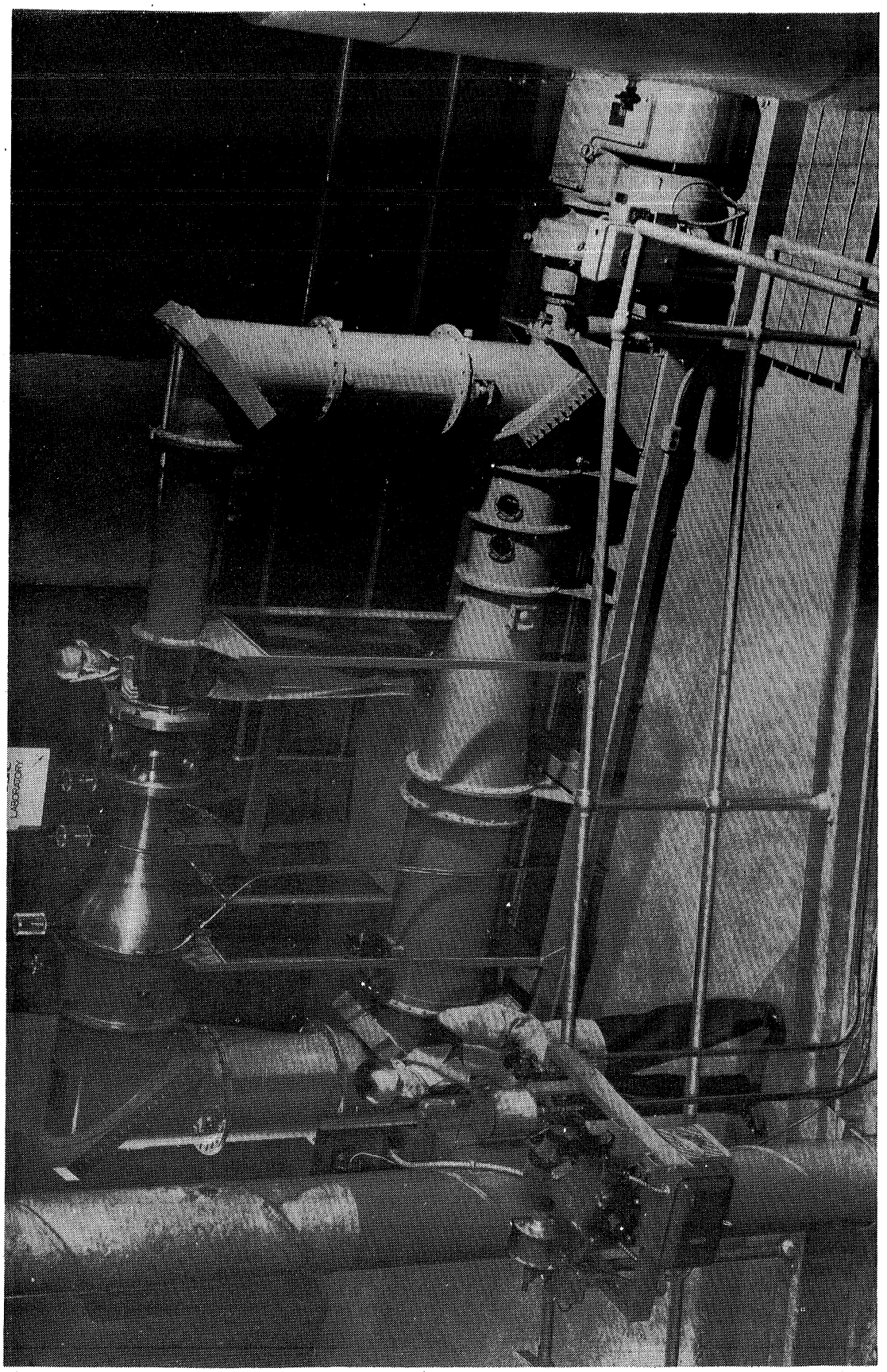

Fig. 4 - Model Water Tunnel and Control Tower

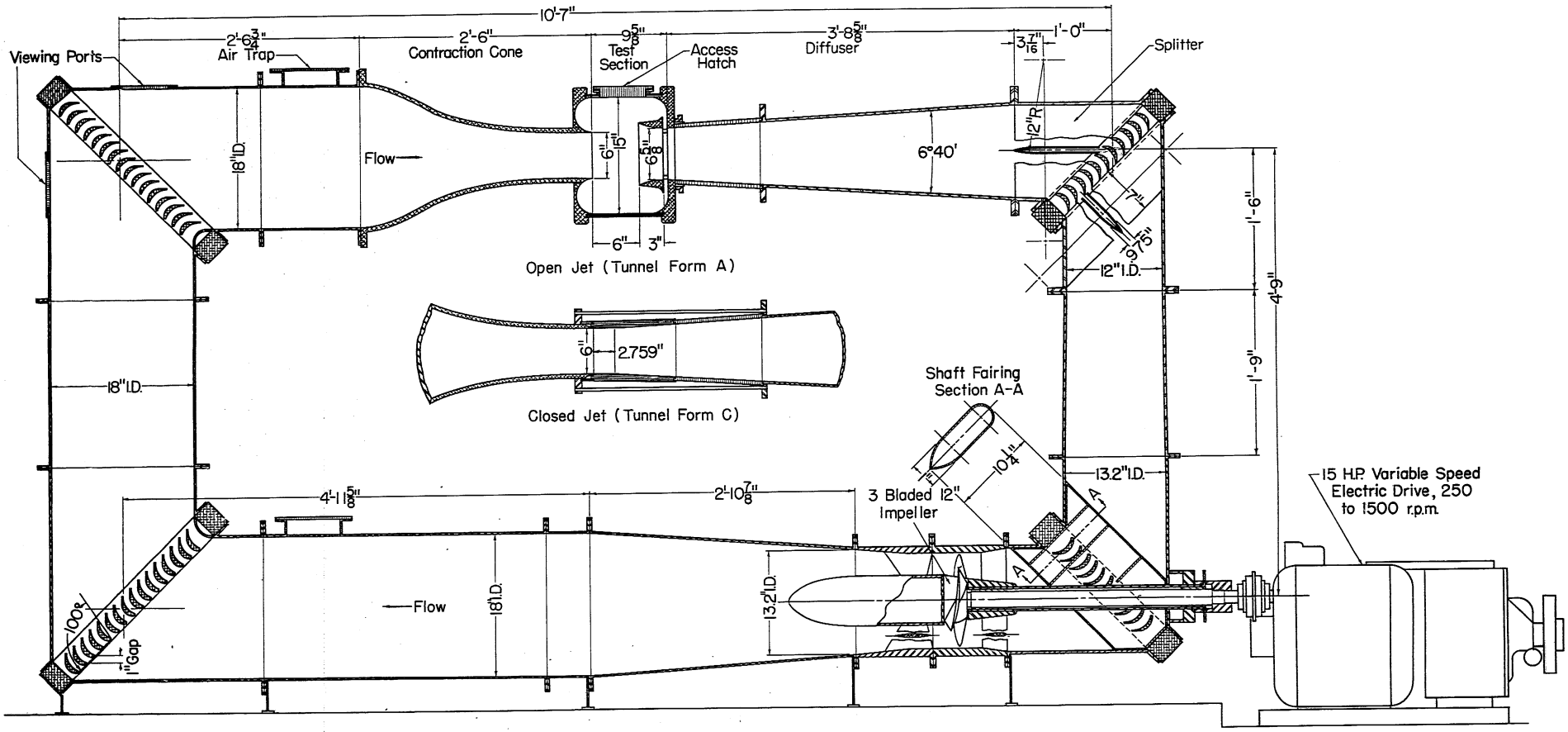

Fig. 5 - Schematic Drawing of Water Tunnel Model (Tunnel Forms A and C)

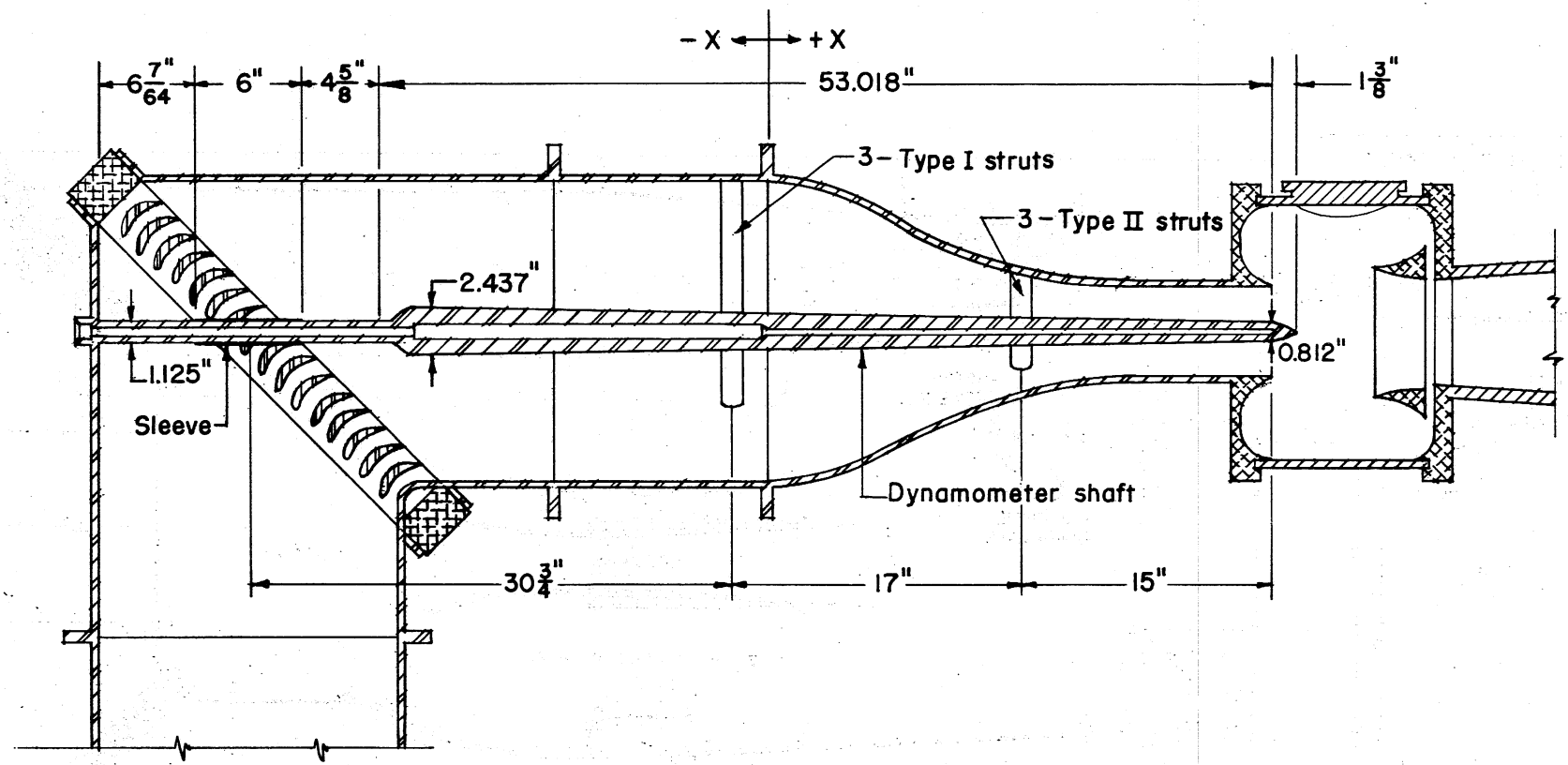

Fig. 6 - Model Contraction Dynamometer Shaft Installation (Tunnel Form B)

Fig. 7 - Intersection of Contraction Dynamometer Shaft with Vaned Elbow IV (Tunnel Form B)

Fig. 8 - Intersection of Contraction Dynamometer Shaft with Vaned Elbow IV (Tunnel Form H)

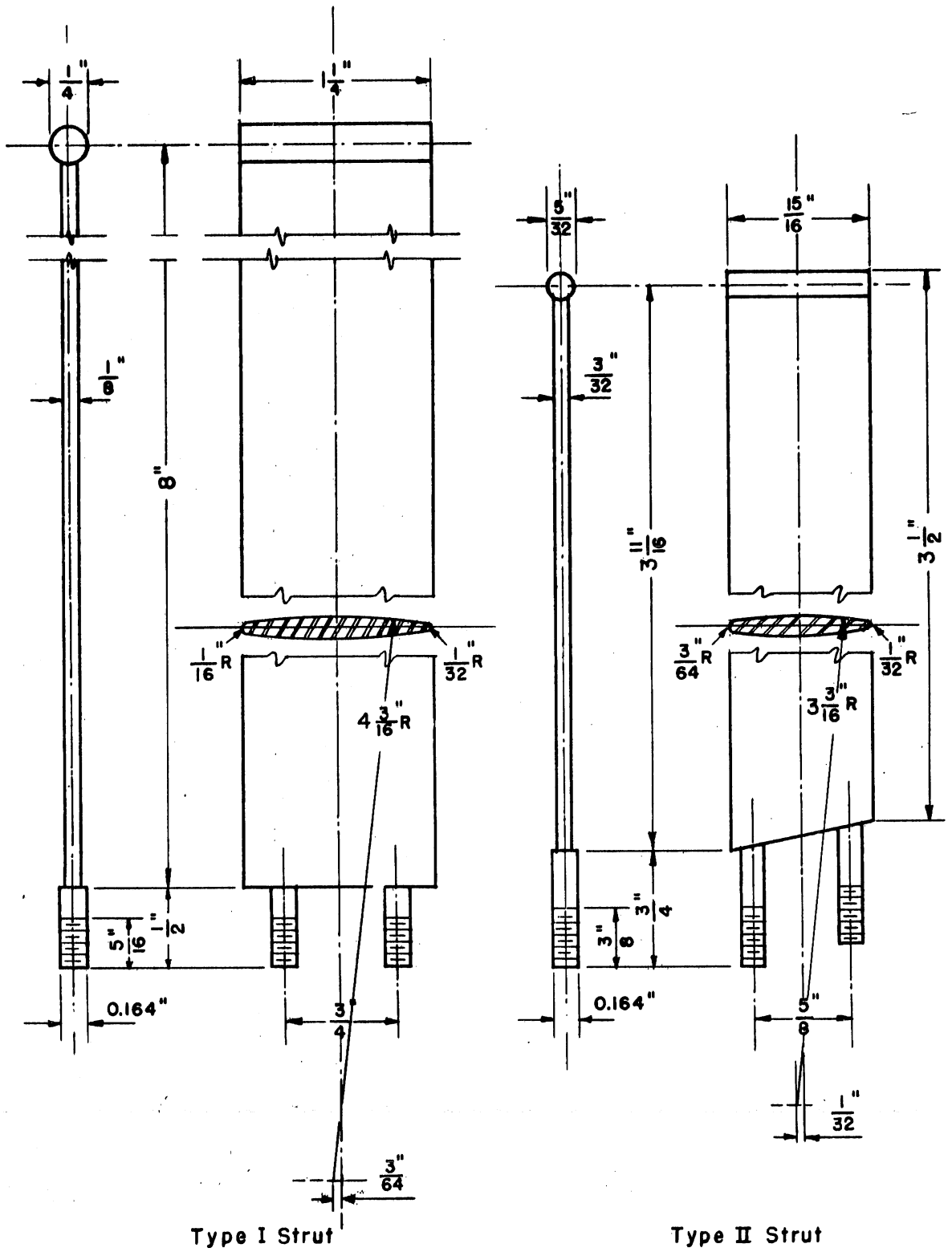

Fig. 9 - Struts Used to Support Dynamometer Shaft

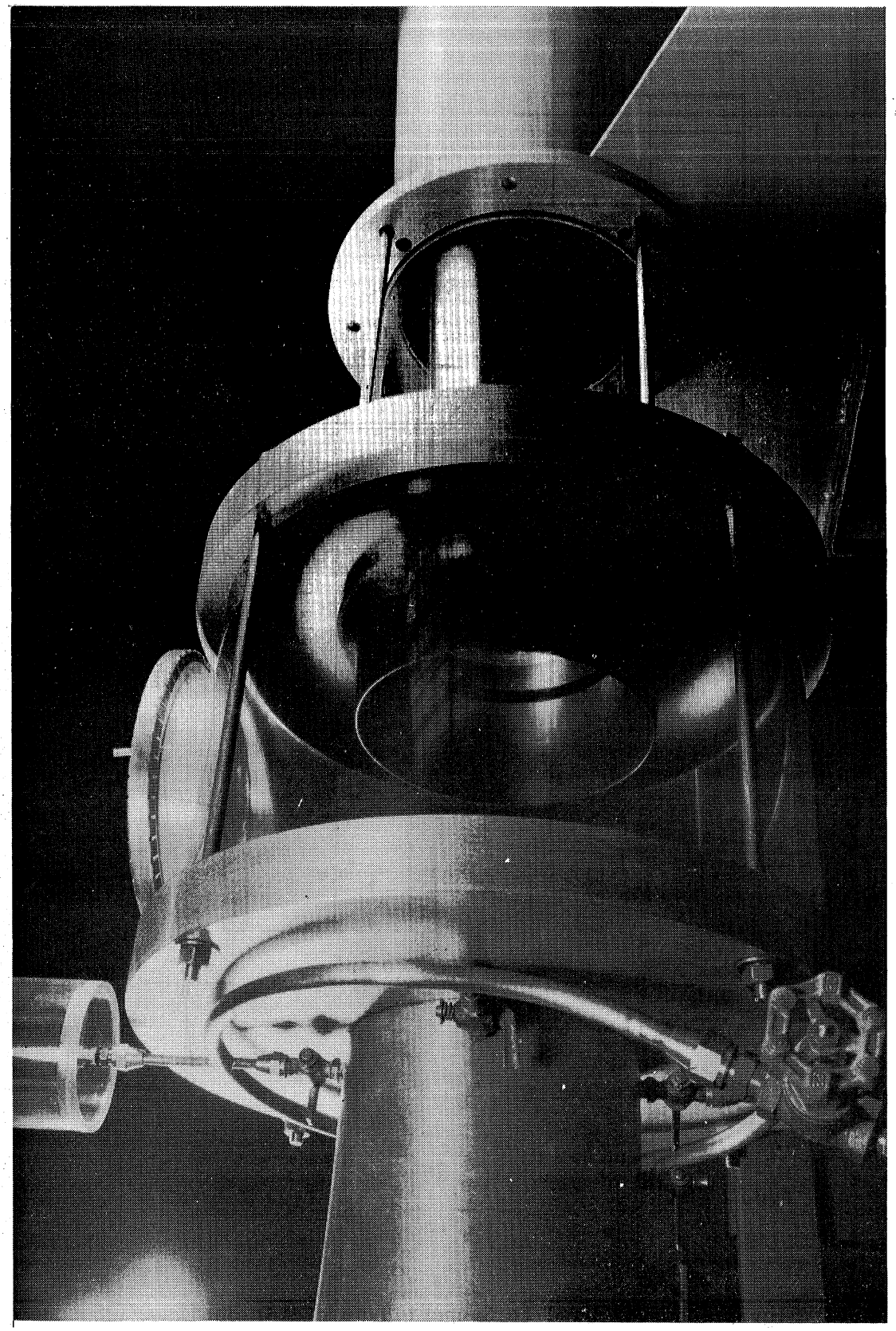

Fig. 10 - Detail of Open-Jet Test Section Showing Pick-Up Cone (Tunnel Form A)

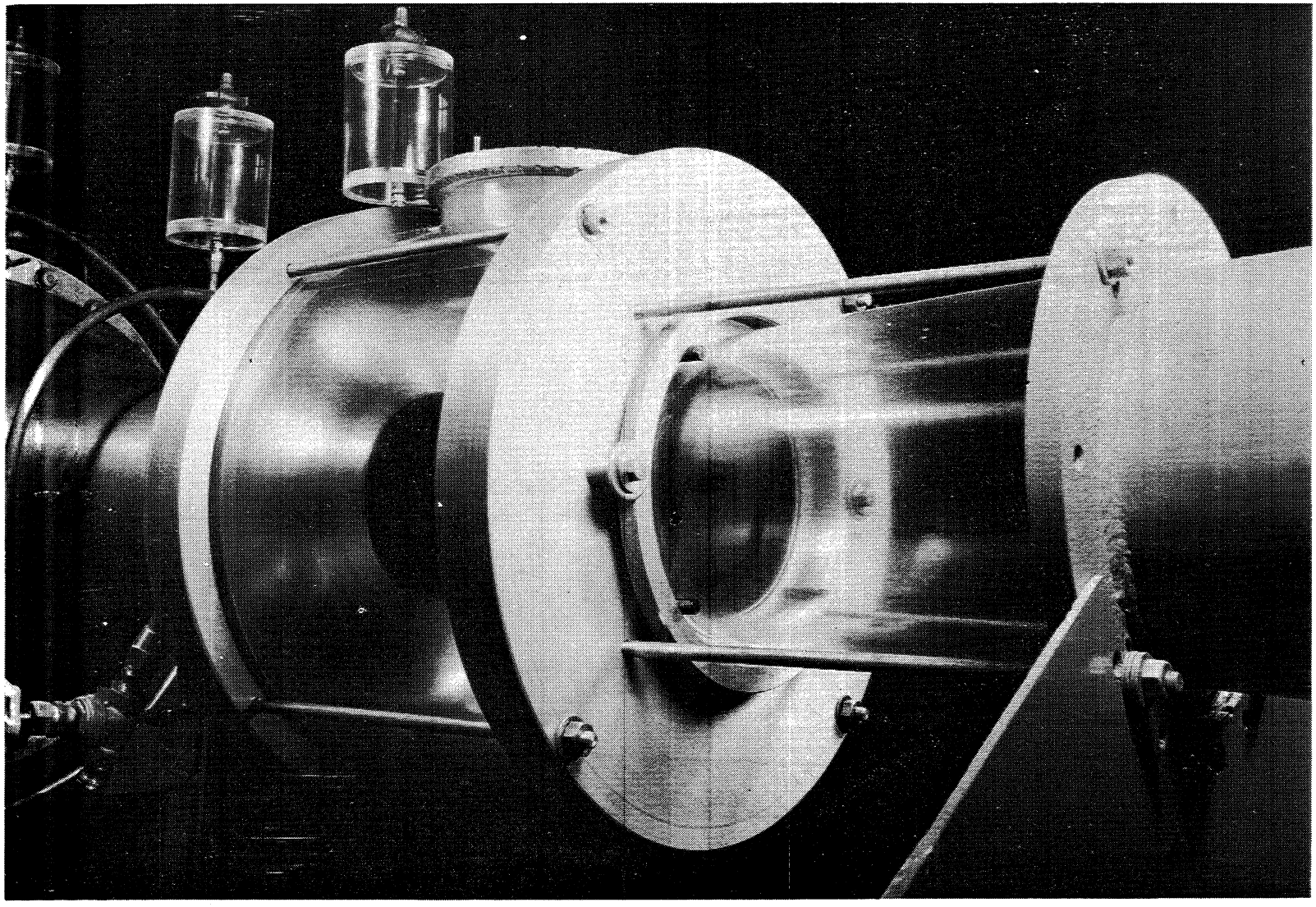

Fig. 11 - Detail of Open-Jet Test Section Showing Adjusting Ring and Contraction Exit (Tunnel Form A)

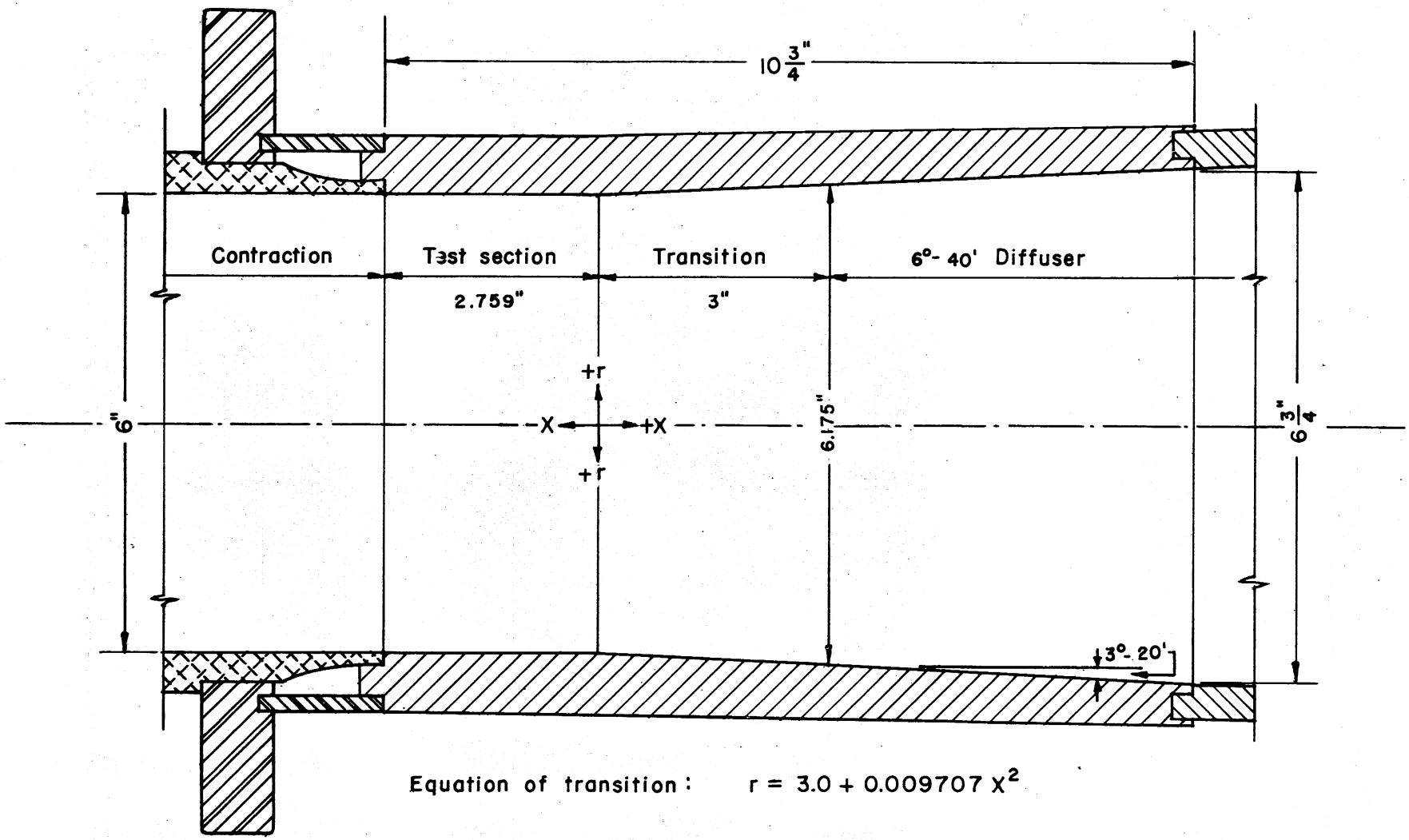

Fig. 12 - Dimensions of Lucite Closed-Jet Test Section (Tunnel Form C)

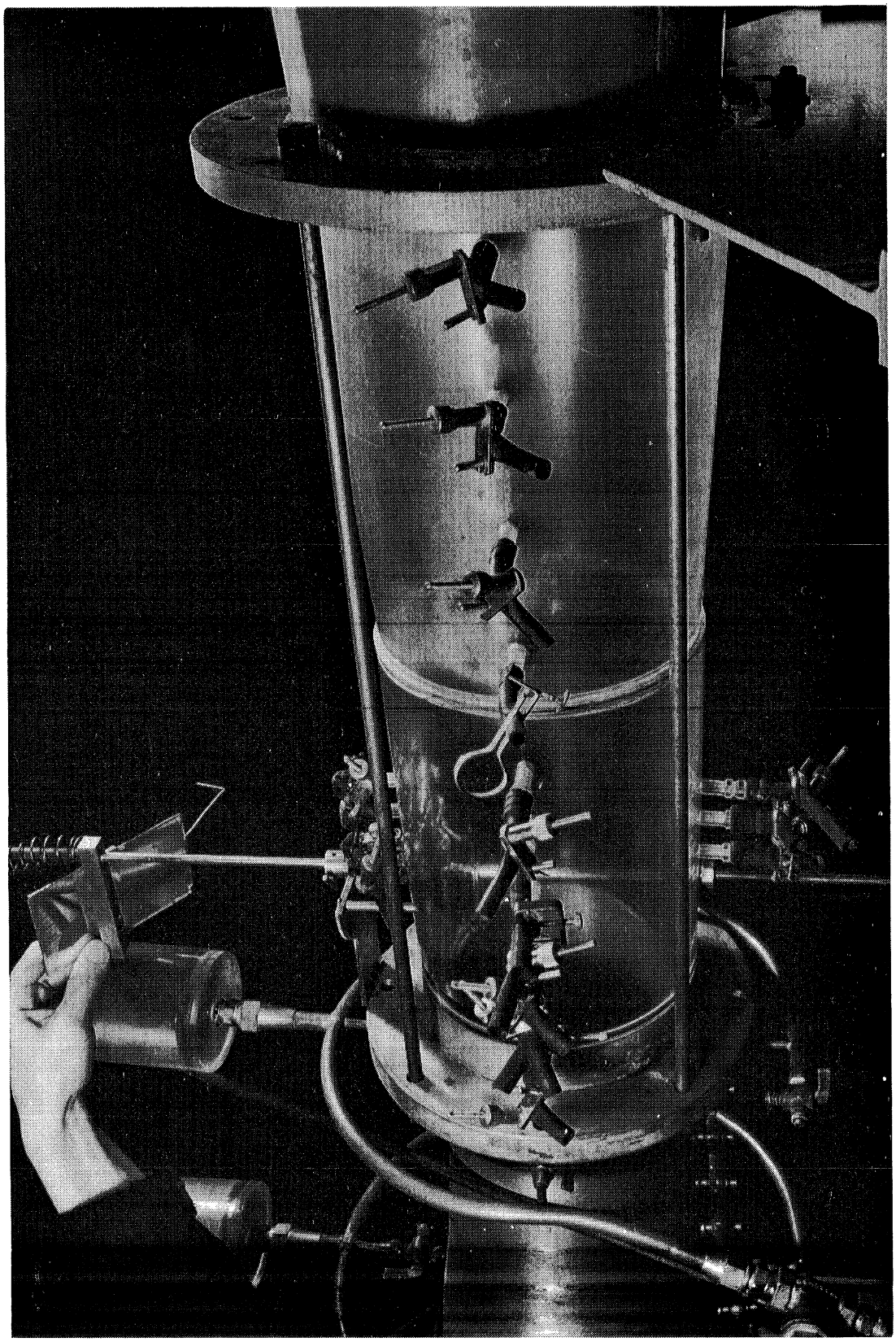

Fig. 13 - Pitot Cylinder in Lucite Closed-Jet Test Section (Tunnel Form C)

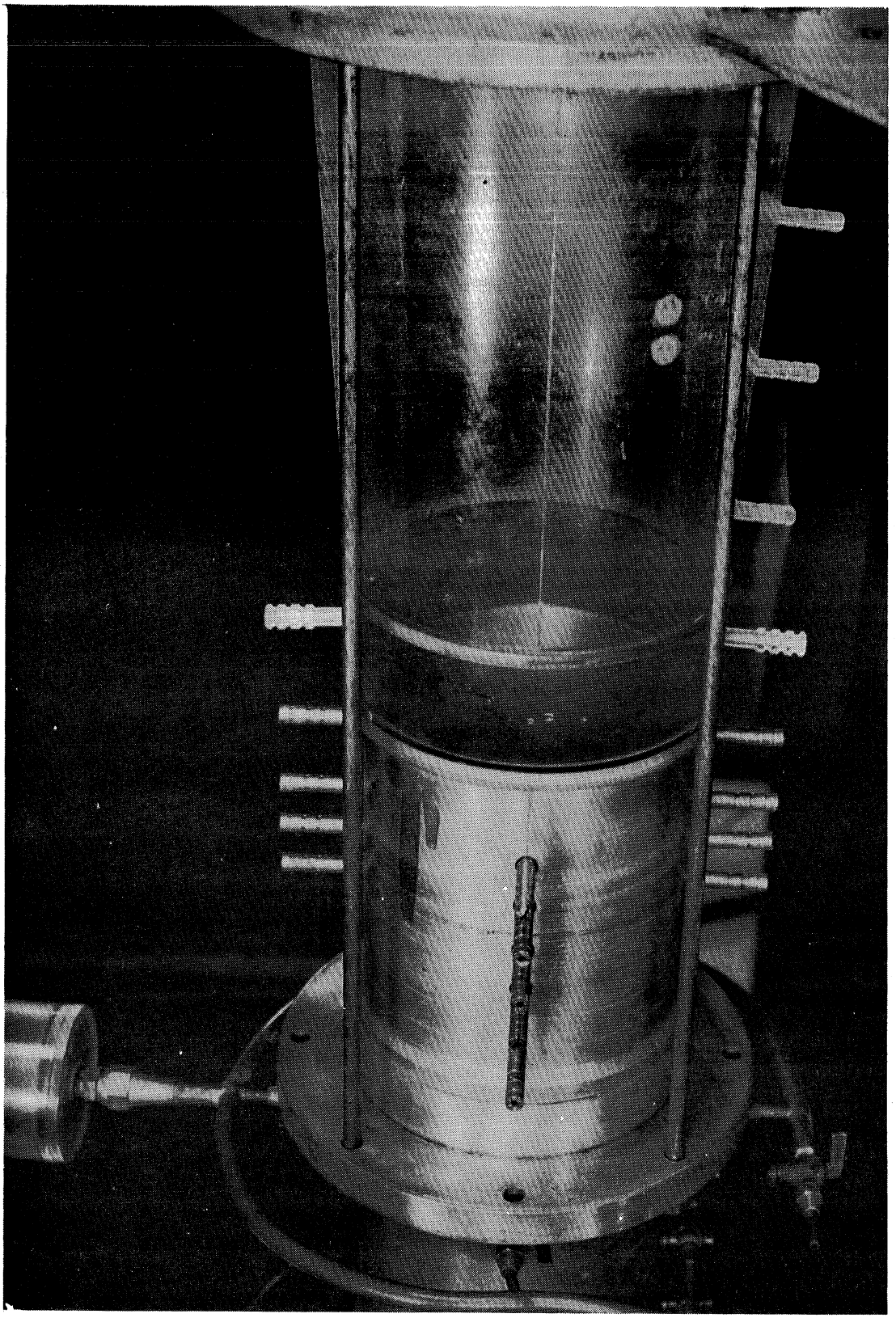

Fig. 14 - Aluminum Closed-Jet Test Section (Tunnel Form C)

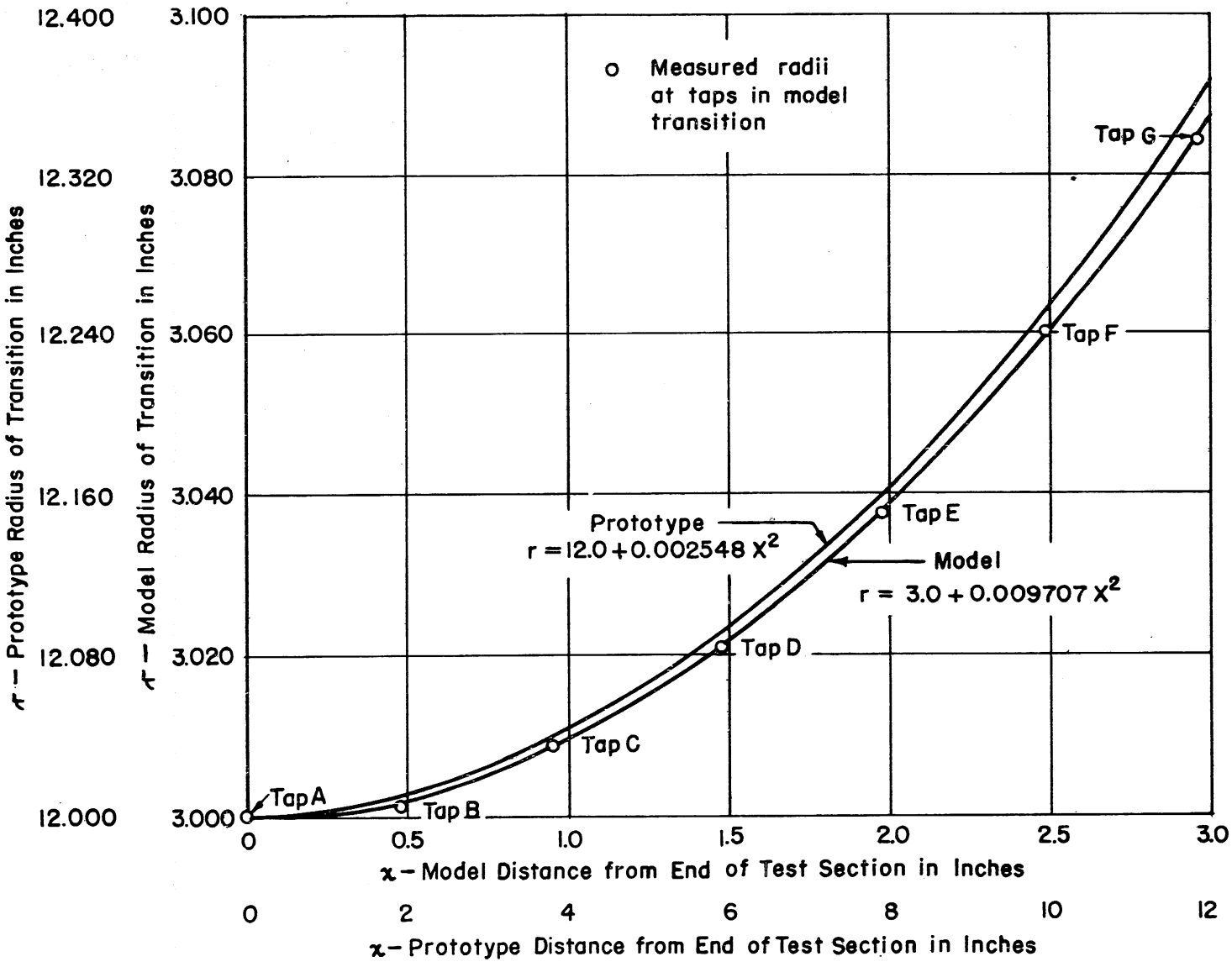

Fig. 15 - Diffuser Transition Boundary in Model and Revised Prototype Tunnel

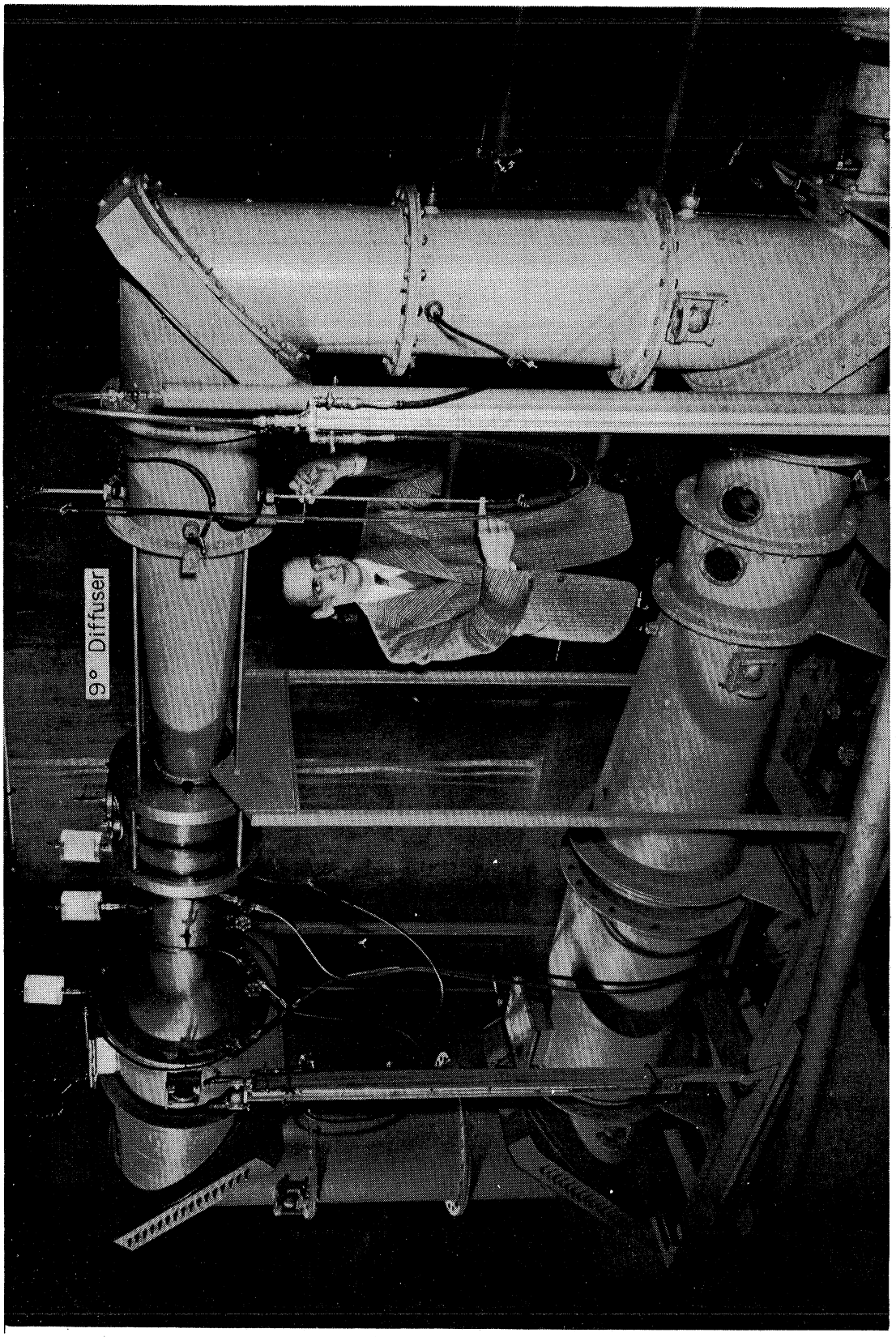

Fig. 16 - Model Tunnel with 9° Main Diffuser (Tunnel Form D)

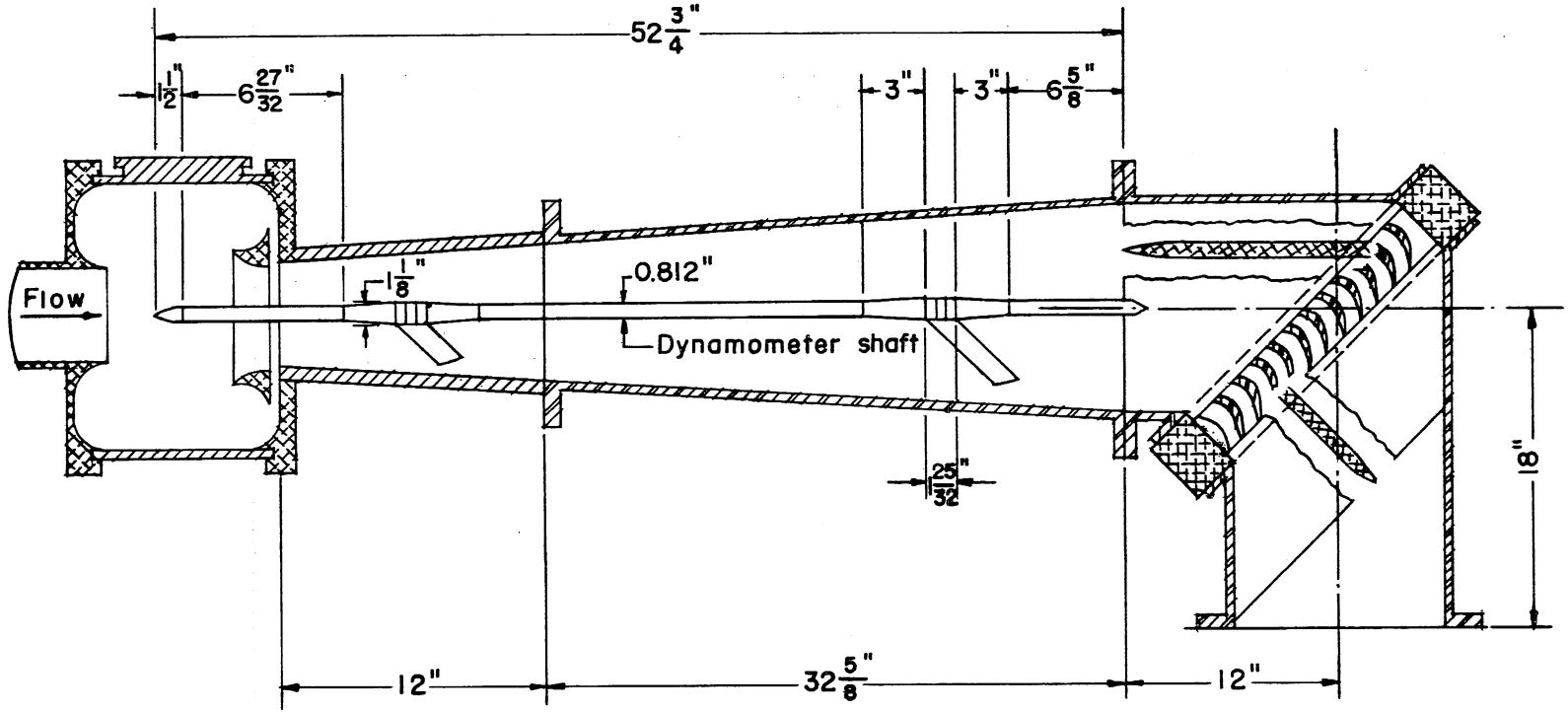

Fig. 17 - Model Diffuser Dynamometer Shaft Installation (Tunnel Form F)

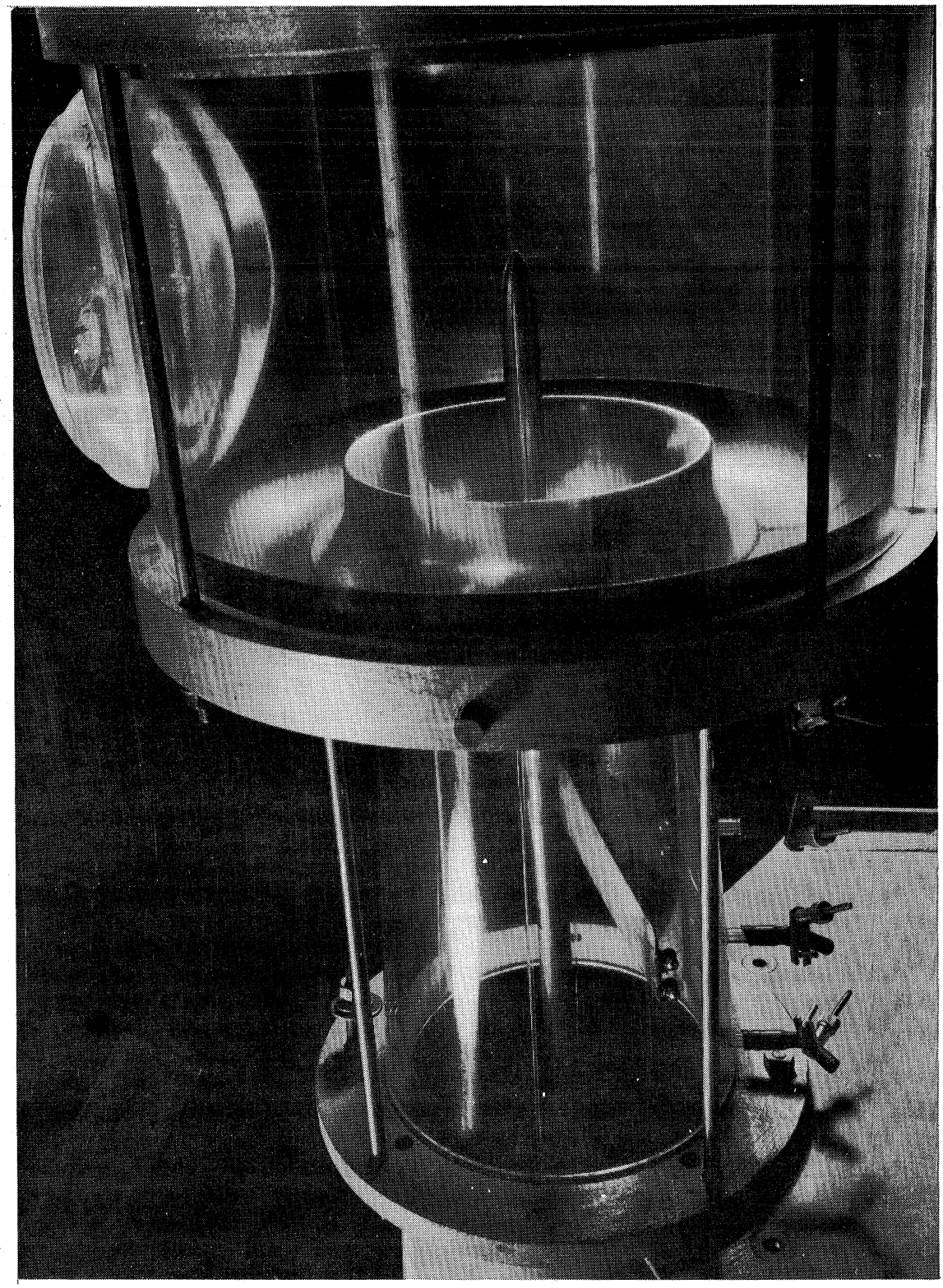

Fig. 18 - Nose and Supporting Struts of Diffuser Dynamometer Shaft (Tunnel Form F)

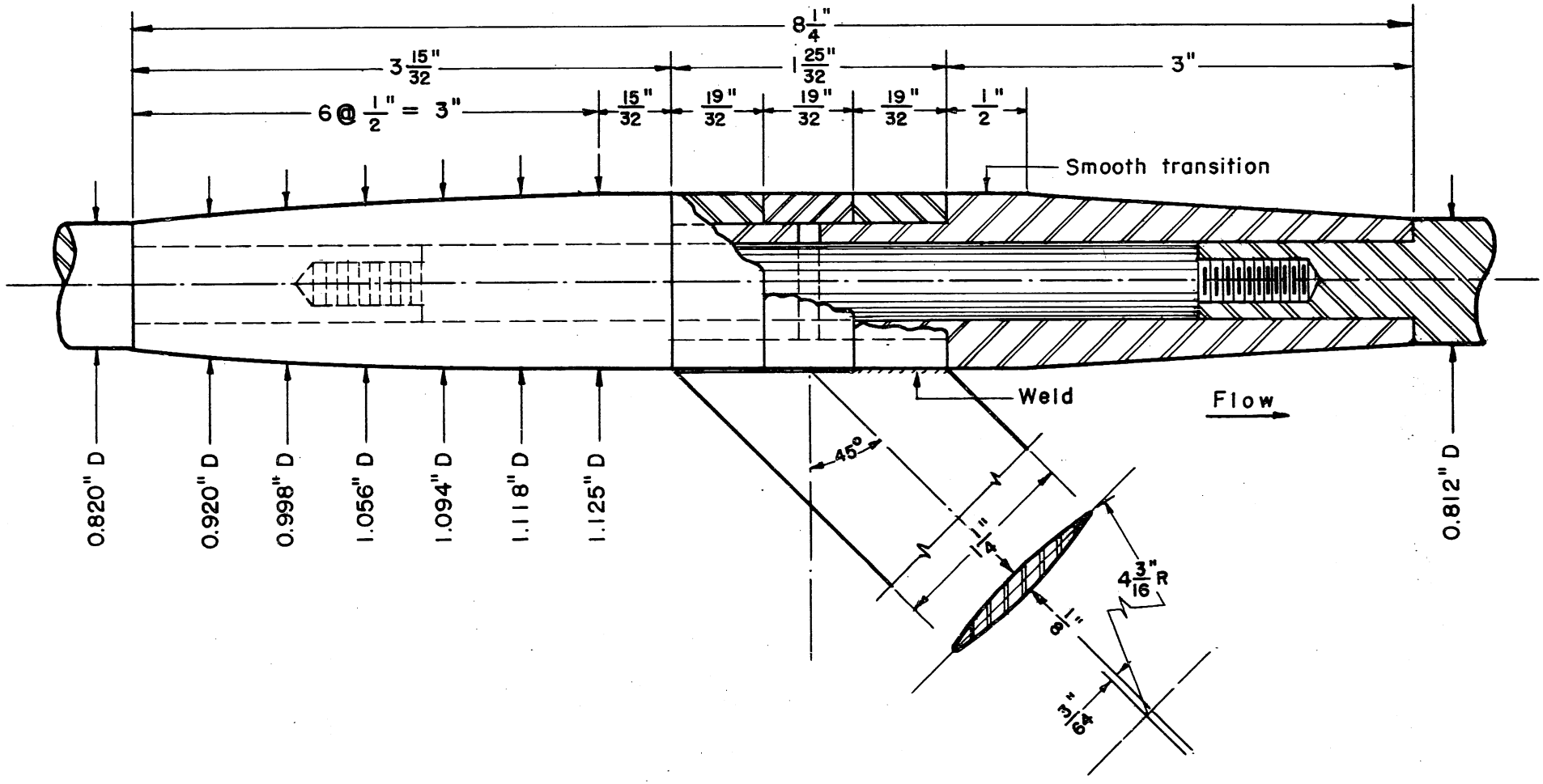

Fig. 19 - Detail of Supports for Diffuser Dynamometer Shaft

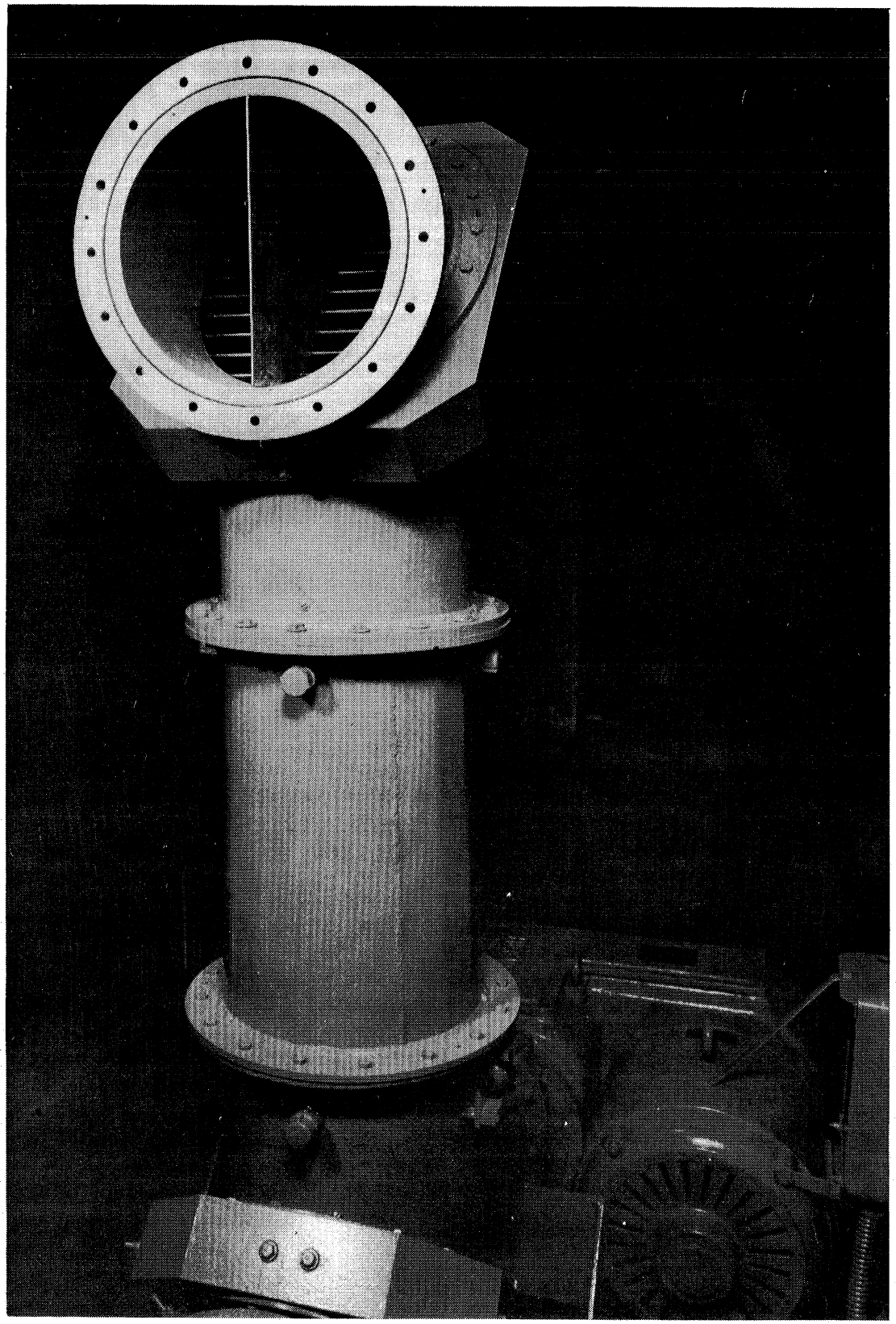

Fig. 20 - Faired Splitter in Vaned Elbow I

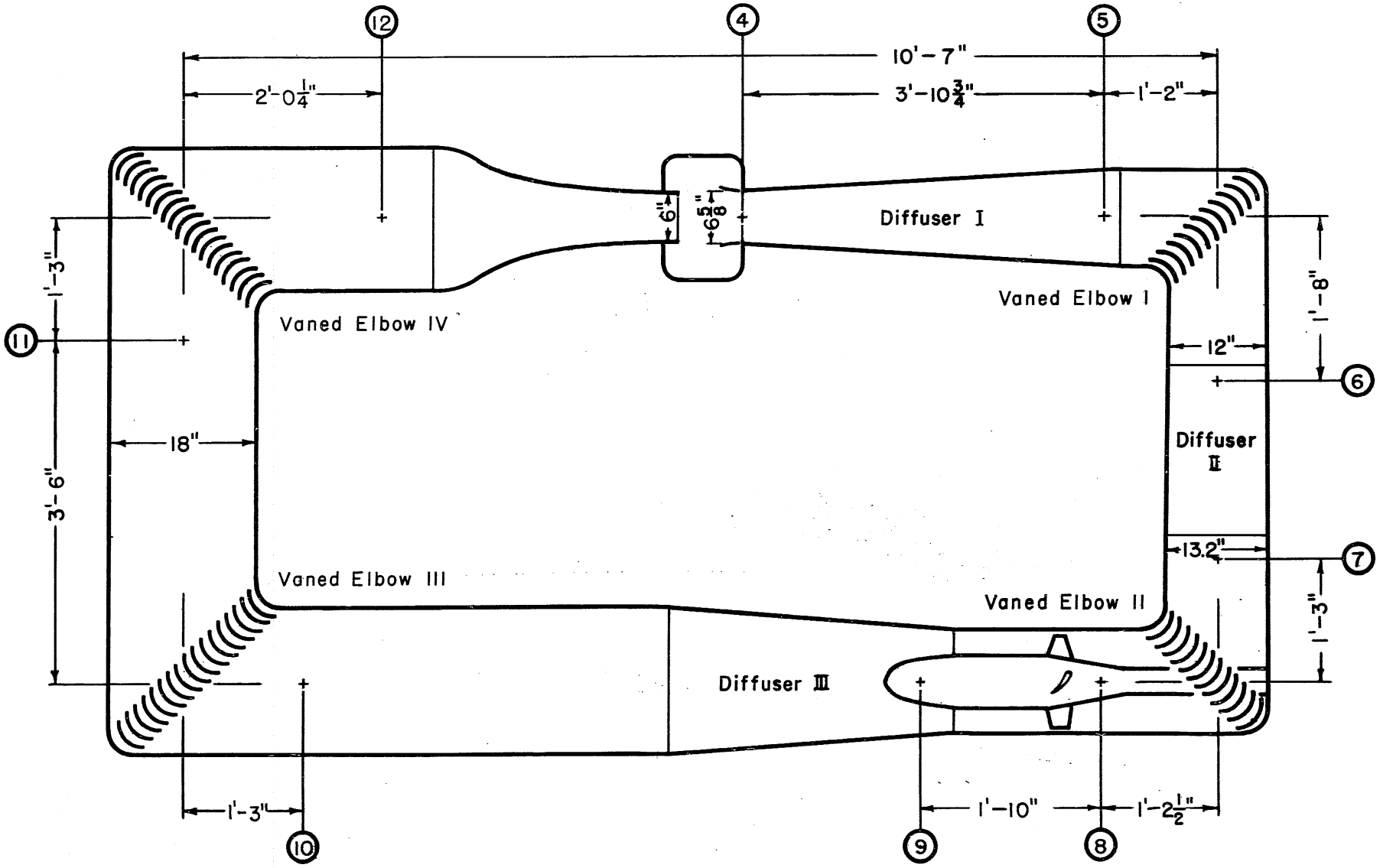

Fig. 21 - Designation of Traverse Stations and Components of Model Tunnel

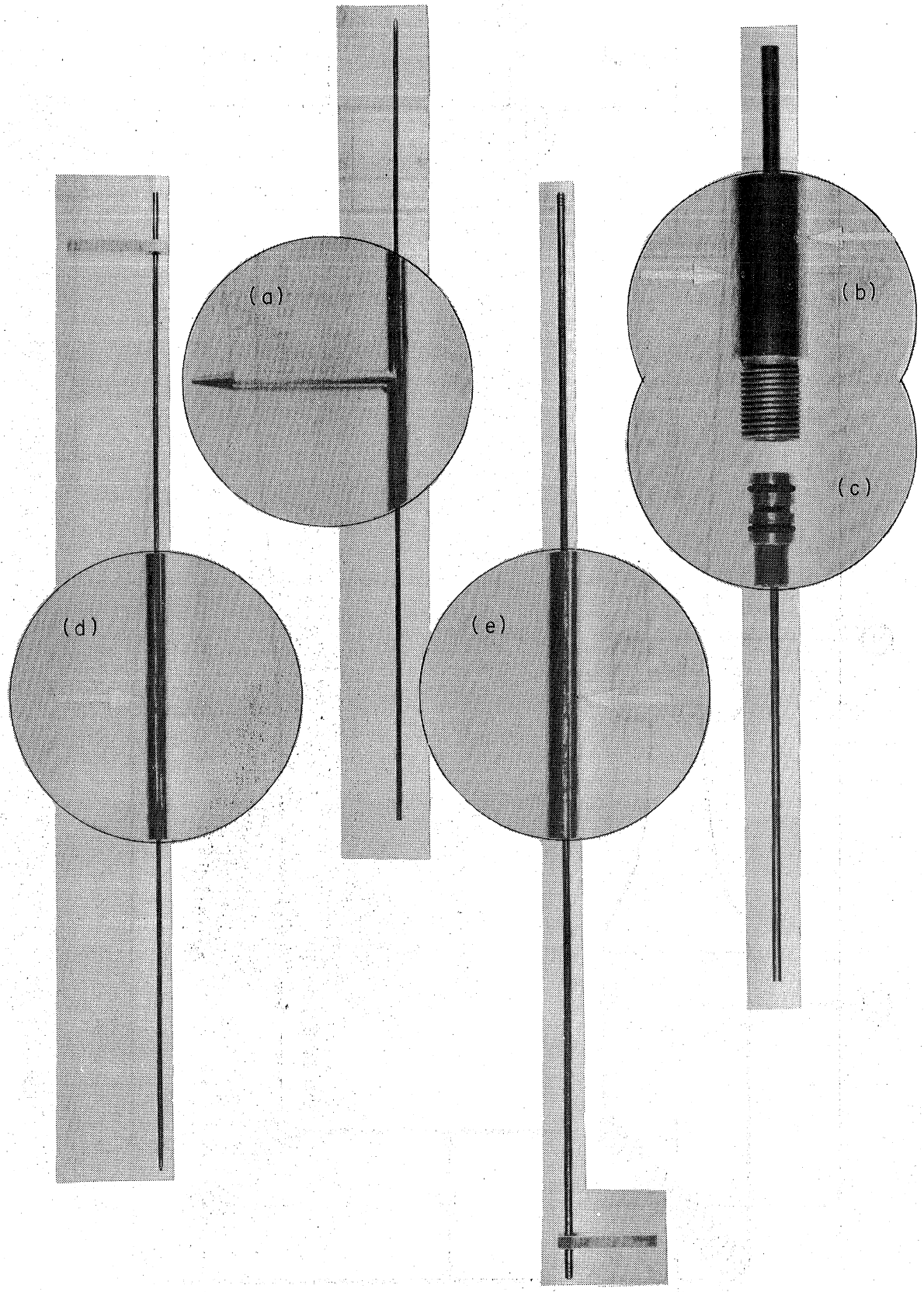

Fig. 22 - Velocity and Pressure Measuring Instruments
Pressure Taps are Indicated by Arrows

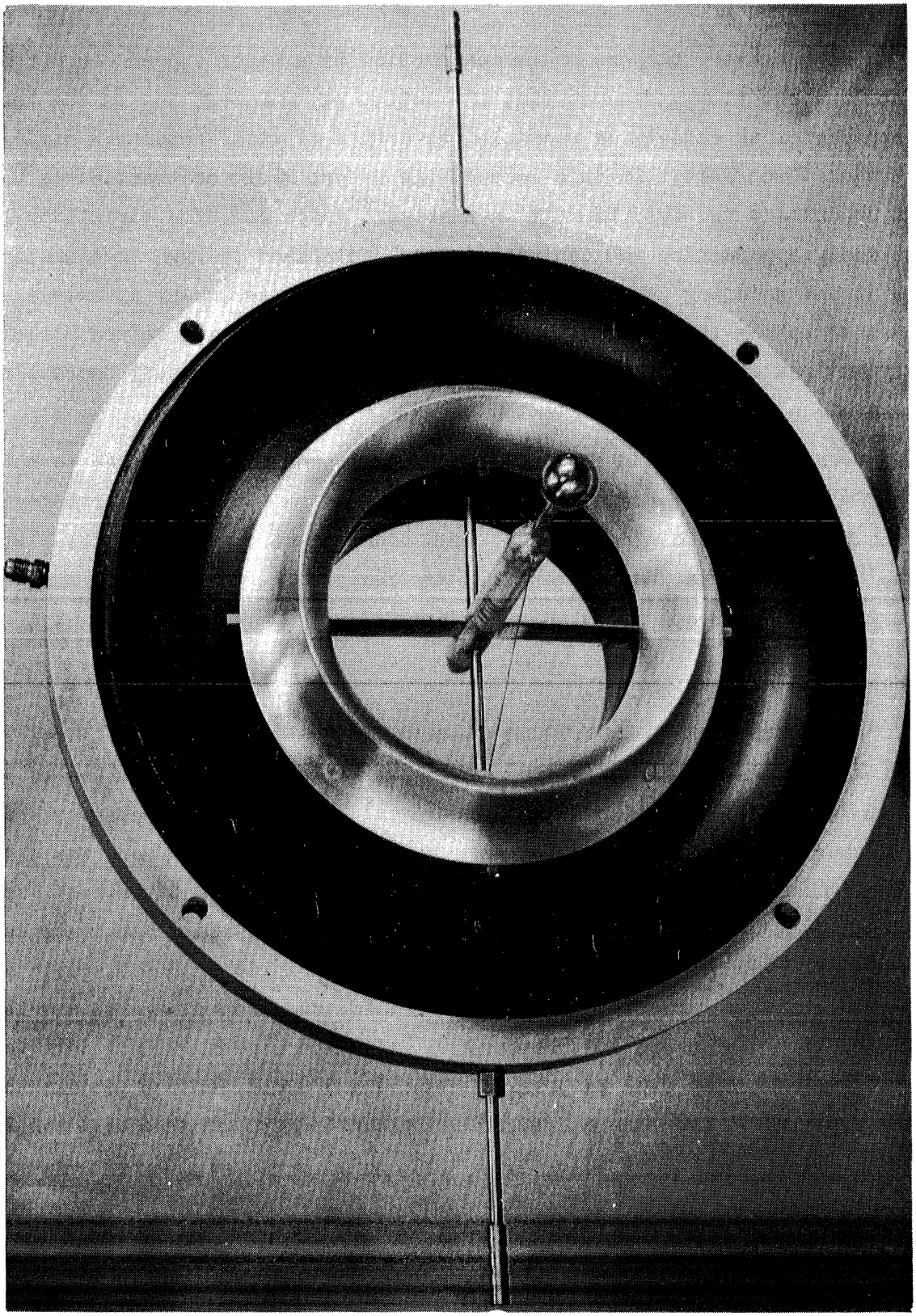

Fig. 23 - Turbulence Sphere Test Section Mounting

PART II. CONTRACTION STUDIES

A. Introduction

The primary purpose of the contraction in a water tunnel circuit is to stabilize the flow stream so that the action of the test jet on the test body approaches as closely as possible the action of still water on a similar body moving through it. In this respect the effect of the contraction on the stream produces a two-fold benefit in that both space and time variations in the velocity approaching the contraction are diminished by the acceleration of the stream entering the contraction. An important secondary advantage of the contraction is that it allows the velocity of flow in the return circuit to be much less than the velocity of the test jet, thereby greatly decreasing the power required to recirculate the stream.

The contraction of the new 24-in. water tunnel was designed to have the same shape as the contraction in the model of the 60-in. water tunnel, since in general this contraction had been found to be a highly satisfactory design. The considerations underlying the choice of contraction ratio and boundary contour are set forth in reference [3].

B. Pressure Distribution

Pressure distribution along the contraction was measured at 19 points located at distances from the upstream flange of the contraction (values of $\underline{x}$) listed in Table IV. The piezometer taps were all 1/32 inch in diameter. Manifolds of four taps each were located at x = 1.5, 17, and 28.5. There was only one tap at the other measuring points. The pressure difference between taps was measured with a 50-in. U-tube using three gage fluids: carbon tetrachloride, ethylene bromide, and Merriam No. 3 gage fluid. The difference in pressure between two adjacent taps was not usually measured directly; one tap was chosen as a reference and pressure measurements were made from this tap to as many neighboring taps as possible. The pressure difference between the measuring points fitted with manifolds was calibrated against discharge before the tunnel was assembled. After assembly, these pressure differences were read with a special manometer called a velometer and served to determine the rate of flow in the model tunnel.

Experimental studies on the contraction consisted of determining the longitudinal pressure distribution at three different rates of flow for the

tunnel operating as an open-jet tunnel with and without the upstream dynamometer shaft and for the tunnel operating as a closed-jet tunnel. The data for all six runs without the shaft are tabulated in Table IV, and the six readings at each piezometer tap are averaged to give a single point which is plotted in Fig. 24 along with the theoretical curve which is obtained by assuming that the flow at any section is purely axial. Making this assumption, application of Bernoulli's equation will show that

$$\frac{\frac{p_a - p_x}{w}}{\frac{\bar{V}_a^2}{2g}} = K - 1$$

where K is equal to $\frac{A_a^2}{A_x^2}$,

A is the cross-sectional area of flow,

p is the pressure (psf),

w is the weight of water (lb per cu ft),

$\bar{V}$ is the mean velocity of flow, and

subscript a indicates the reference station from which all pressures were computed, which in these experiments was at $x = 1.5$. The pressure distributions measured at three different velocities with the shaft in the contraction were also computed and plotted in the same manner in Fig. 24.

Theoretically, there should be no difference in the pressure distribution along the contraction when operating with either a closed- or open-jet test section, unless there is a radial variation in pressure in the jet at the end of the contraction caused by the pick-up cone of the free jet. The theory appears to be confirmed in Table IV and by later experimental work which indicated that the pressure influence of the pick-up cone did not extend upstream as far as the end of the contraction.

Since the pressure distribution data in Table IV were not measured with the velometer, but with a standard 50-in. U-tube manometer in several successive increments, the total pressure difference across the contraction computed from these runs was not, in general, equal to the velometer reading. This caused some scatter in the end points of the dimensionless pressure data which could have been partially eliminated by adjusting all of the pressure

measurements. The data have been presented, however, without adjustment since it was thought that knowledge of the experimental error would be of value in interpreting the results.

The most significant fact that can be deduced from the experimental work on the contraction is that the boundary pressure decreases steadily in the direction of flow both with and without the dynamometer shaft in the contraction. This will insure that there will be no cavitation on the walls of the contraction unless there is cavitation at some point in the test section. The monotonically decreasing pressure also assures that there will be no major separation of the flow from the walls, as had been already experimentally confirmed [3]. The pressure drop in the upstream portion of the contraction is less than the theoretical pressure drop, assuming uniform axial flow. This is due to the fact that the pressure increases towards the wall when fluid flows along a concave wall. It can also be inferred that the pressure along this part of the boundary is higher than the pressure at the interior of the fluid, since the wall pressure at x = 1.5 was about 10 per cent of the local velocity head higher than the pressure at x = -6.0, the next tap upstream from the contraction. Since there was no increase in cross-sectional area between the two points, the average pressure must have dropped in the direction of flow, so that the boundary pressure must be higher than the average pressure. The effect of streamline curvature also explains why the pressure drop downstream of x = 15, where the wall is convex, is greater than the theoretical value, although part of the pressure difference must be ascribed to energy loss caused by wall friction.

C. Head Loss

The total loss in energy between x = 1.5 and x = 28.5 is probably closely represented by the difference between the theoretical and actual pressures at x = 28.5. Since the walls of the contraction were parallel at the beginning and end of the contraction, very little, if any, of this pressure difference can be ascribed to the effects of wall curvature. The experimental determination of the difference between theoretical and actual pressure is hampered by the fact that the experimental pressure difference between x = 1.5 and x = 28.5 is used to compute the discharge and, therefore, is used to compute the theoretical pressure difference. In order to accurately measure the head loss in the contraction both with and without the dynamometer shaft, it

is necessary to find a way of measuring the discharge independent of the pressure difference across the contraction. Such a basis for measuring discharge was not available in the flow circuit, since no other pressure difference was both large enough and stable enough, and an integrated Pitot traverse would not be expected to give an accuracy of discharge better than 1 per cent, which would be an error of 2 per cent in the velocity head. The relationship between the discharge and the pressure drop across the contraction had been determined experimentally [2] by weighing the discharge, but this was done before the contraction was remachined. However, it was assumed that the remachining did not change the head loss in the contraction, and a new calibration curve was computed for the rebored contraction taking into account the small change in contraction ratio which resulted from remachining the contraction. Thus, in order to measure the actual velocity of flow during a test, the total pressure drop across the manifold was measured with the velometer, and the velocity of flow was determined from the recomputed calibration curve.

There was no possibility of determining experimentally the head loss of the rebored contraction with or without the dynamometer shaft installed unless the calibration was rerun. If, for instance, it is assumed that the dynamometer shaft assembly causes an additional head loss of 0.5 per cent $V_o^2/2g$ and a new calibration curve is computed on this basis, it can be shown that the experimental increase in head loss computed on the basis of the revised calibration must exactly equal the assumed head loss.* The best estimate of the head loss in the contraction without the dynamometer shaft can be obtained by examining the original calibration data which are shown in Table V. The coefficient of head loss (K_o) was computed from the following arrangement of the Bernoulli equation:

$$K_o = \frac{h_l}{\frac{V_o^2}{2g}} = \frac{\frac{(p_{1.5} - p_{28.5})}{w}}{\frac{V_o^2}{2g}} - a_{28.5}\left(\frac{6}{d_{28.5}}\right)^4 + a_{1.5}\left(\frac{6}{d_{1.5}}\right)^4$$

*In this report V_o refers to the average velocity of flow in a section 6 inches in diameter in the model or 24 inches in diameter in the prototype.

Substituting the values applicable to the calibration data,

$$\alpha_{28.5} = 1.000$$

$$d_{28.5} = 6.004 \text{ in.}$$

$$\alpha_{1.5} = 1.071$$

$$d_{1.5} = 17.908 \text{ in.}$$

gives the head loss coefficients which are tabulated in Table V and plotted in Fig. 25. The average value of the coefficient for 15 runs was 0.0315 and it is estimated that the prototype coefficient of loss for the contraction operating without the dynamometer shaft installed will be 0.0290, since the tests indicated that there is some decrease in the head loss coefficients with increasing Reynolds number.

When the dynamometer shaft is installed, the head loss in the contraction will be increased by the drag on the supporting struts and by the skin drag on the shaft itself. The head loss due to skin friction on the shaft was estimated by dividing the contraction and shaft into seven longitudinal segments and computing the drag on the shaft, assuming an average coefficient of drag of 0.004. Each skin drag increment must result in a pressure difference between the end planes of the corresponding segment in excess of that which would exist if there were no drag on the shaft. The pressure increment times the local area of flow must equal the drag on the increment of shaft skin area,

$$\Delta p \cdot A_l = A_s C_D w \frac{V_l^2}{2g}$$

so that

$$\frac{\Delta p}{w} = \frac{A_s}{A_l} C_D \left(\frac{V_l}{V_o}\right)^2 \frac{V_o^2}{2g}$$

where V_l is the average local velocity,
V_o is the test section velocity,
C_D is the coefficient of skin drag,
A_s is the increment of shaft skin area,
A_l is the average local area of flow, and
Δp is the pressure increment.

Adding the pressure increments for each segment showed that the increased pressure drop across the contraction was $0.0035\ wV_o^2/2g$; the coefficient 0.0035 is also the head loss coefficient of the shaft in terms of the test section velocity head. The struts in the contraction had a thickness-chord ratio of 0.10 and, on the basis of aeronautical research, their coefficient of drag was assumed to be 0.008. The pressure increment due to the presence of the struts was computed from

$$\frac{\Delta p}{w} = \left(\frac{CL}{A_l}\right) C_D \left(\frac{V_l}{V_o}\right)^2 \frac{V_o^2}{2g}$$

where C is the chord length of the struts and L is the sum of the lengths of the three struts. This computation showed that the struts caused an additional pressure drop across the contraction of $0.0005\ wV_o^2/2g$ so that the total increase in pressure drop across the contraction due to the shaft installation was $0.0040\ wV_o^2/2g$. A new calibration curve was computed for the contraction on the basis of this value, taking into account the change in area due to the presence of the shaft. This calibration was used for the analysis of tests involving the presence of the shaft in the contraction.

After this shaft installation had been tested in the model tunnel, it was decided at Taylor Model Basin that the shaft was not adequately supported in the contraction and the design of the prototype was changed so that three additional struts having their leading edges 27.3 in. upstream of the end of the contraction in the prototype and having dimensions of 0.22 in. by 6.6 in. would support the shaft at its downstream end. These struts were not tested in the model tunnel because of the impracticability of constructing them accurately to the model scale. However, head loss in the prototype installation due to these additional struts can be quite accurately estimated on the basis of boundary-layer theory, since their relative thickness is so small that the form drag can be neglected. The Reynolds number, using the chord of the struts as a length parameter, will be

$$Re = \frac{V l}{\nu} = 5.29 \cdot 10^4\ V_o$$

For this Reynolds number, the average drag coefficient for one side of the strut will be

$$C_D = 0.0032$$

and the increase in pressure drop across the contraction due to the presence of these struts will be

$$\frac{\Delta p}{w} = \left(\frac{CL}{A_\ell}\right) 2C_D \left(\frac{V_\ell^2}{V_o^2}\right) \frac{V_o^2}{2g} = 0.0020 \frac{V_o^2}{2g}$$

It is not expected that the presence of these three struts will have any adverse effects on the contraction performance other than causing a slight nonuniformity of the velocity in the test section. The lateral extent of the wakes of the struts and probable maximum velocity deficiency is analyzed in Part III of this report. The centerline of the struts will be in a region of flow where the pressure is approximately $0.13\ V_o^2/2g$ ft higher than the pressure in the test section. If it is assumed that the pressure in the test section is vapor pressure, the cavitation index at the struts will be

$$\sigma = \frac{\dfrac{(p - p_{vp})}{w}}{\dfrac{V^2}{2g}} = \frac{\dfrac{\left(0.13 \dfrac{V_o^2}{2g} + p_{vp} - p_{vp}\right)}{w}}{\dfrac{V_o^2}{2g}\left(\dfrac{A_o}{A_\ell}\right)^4} = 0.15$$

Applying Eq. (1) of reference [1] (page 26) the critical cavitation index of the struts will be 0.114, so that the struts will not cavitate even under the impossibly severe condition of vapor pressure in the test section.

D. Velocity Distribution

As stated previously, the primary purpose of the contraction is to accelerate the flow in such a manner that both time and space variations in velocity are made as small as possible. The adequacy of the contraction in this respect is illustrated in Parts III and IV, in which are presented velocity traverses made in both open- and closed-jet test sections. In general,

it may be stated that space variations in velocity in the core of the jet are of such small magnitude (approximately 1/2 of 1 per cent) that the test stream will adequately approximate the absolutely uniform velocity which, theoretically, will act on a prototype test body. Tests with a turbulence sphere installation indicate that the root mean square time variations in velocity in the test stream are of the order of 0.008 V_o.

E. Conclusions

On the basis of these experimental and analytical investigations of the contraction and the following studies of the test sections, it is concluded that:

1. The space variations in mean velocity of the stream leaving the contraction will be small enough (of the order of 1/2 of 1 per cent) so that they will not be detrimental to testing procedures.

2. The head loss in the prototype contraction may be predicted as 0.0290 $V_o^2/2g$ without the dynamometer shaft housing and 0.0358 with the dynamometer shaft housing installed.

3. There will be no detrimental adverse pressure gradient in the contraction with or without the dynamometer shaft housing installed.

4. Such cavitation as may occur on the struts supporting the dynamometer shaft housing must be preceded by very severe cavitation in the test section.

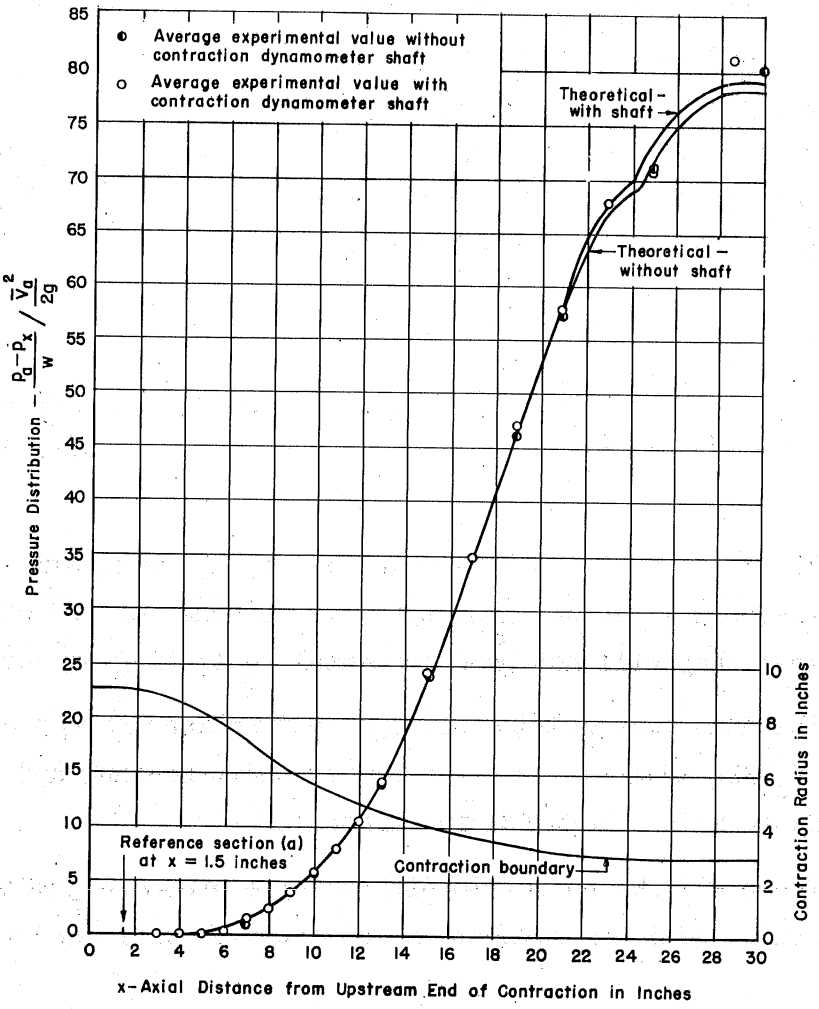

Fig. 24 - Pressure Distribution along Contraction Boundary

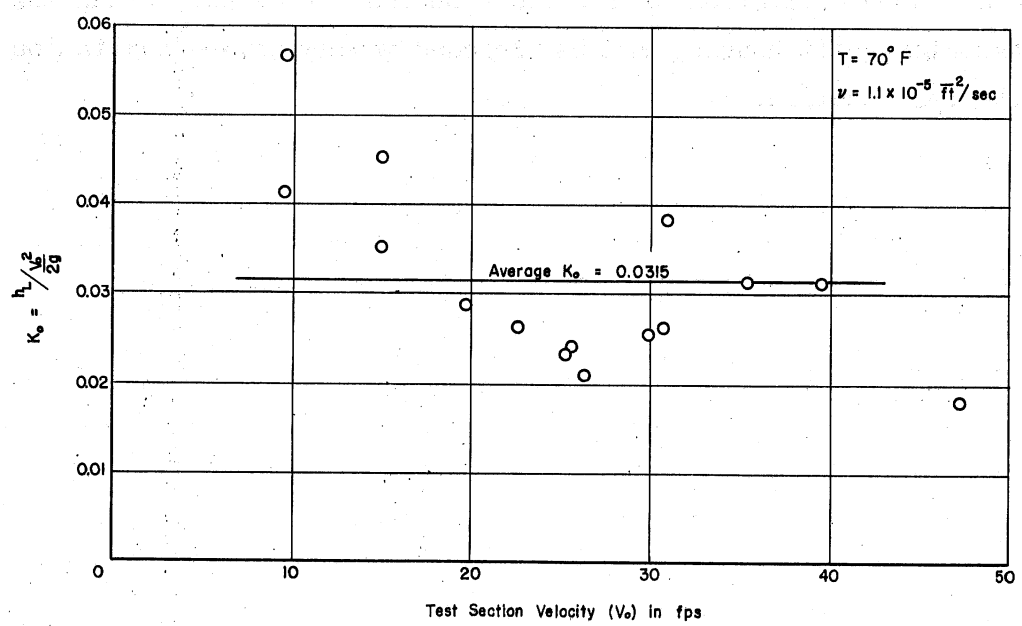

Fig. 25 - Contraction Head Loss Coefficient (Computed from Calibration Data)

PART III. OPEN-JET TEST SECTION AND CAVITATION INDEX

A. Introduction

The prototype water tunnel was designed primarily as a facility for testing model propellers. Since the accuracy with which propellers can be machined increases with the size of the propeller, it is naturally desirable to test propellers that are as large as possible. The tunnel was therefore designed with an open-jet test section because larger propellers can be tested in an open jet than in a closed jet.

In the open-jet test section shown in Figs. 5 and 27, the test stream is discharged from the contraction into a cylindrical chamber somewhat larger in cross section than the test stream. This chamber is filled with water at rest and as the jet enters the chamber, large tangential shearing stresses are set up by the high velocity gradient at the edge of the jet. This shearing action in turn results in the formation of eddies, and it is manifested as a zone of free turbulence which broadens as the flow proceeds downstream. Diffusion in the turbulent layer causes some of the water initially at rest to be accelerated and entrained by the jet. Also, the zone of diffusion extends into the test stream and decreases the diameter of the core of uniform velocity. The overall effect of this mixing is to increase the discharge of the jet as it passes through the test section. Water being relatively incompressible, it is necessary that this increase in discharge be spilled from the jet before it enters the diffuser. This is accomplished by having a gap between the pick-up cone (exit nozzle) which receives the jet at the downstream end of the test section and the throat of the diffuser. The upstream portion of the pick-up cone must be somewhat larger than the initial diameter of the jet in order to enclose most of the zone of diffusion.

The extent of the zone of diffusion is determined by the distance the jet travels between the contraction and the pick-up cone. The prototype tunnel was originally designed so that the jet would be 1 diam long when the pick-up cone gap was 2 1/2 in. (5/8 inch in the model); the chamber surrounding the jet was designed to be 2 1/2 times the diameter of the jet. The rounded corners in the test section chamber are intended to guide the steady circulation pattern which develops as a result of the entrainment and spilling.

Ideally, the core flow in the test jet should be free from both space and time variations in pressure and velocity. In designing propellers, it is

assumed that they are moving through a fluid at rest and thus that the relative motion between the hub axis and the fluid is the same as if the propeller were stationary in a stream of uniform velocity and pressure. Any steady variations in the flow field around the propeller, such as might be caused by the ship's hull or appendages, can most easily be simulated in a water tunnel if the jet is initially uniform. The prototype propeller will also be in motion in water which has very little or no turbulence, indicating that random unsteady variations in velocity should be restricted to a practical minimum. Unsteady variations in pressure will likewise be detrimental to test results and, if they are of a regular cyclic nature, they could excite the tunnel structure to resonant vibration. The tunnel will also be used for testing model propellers under cavitating conditions. For this purpose, it is desirable that the critical cavitation index of the open jet be as small as possible in order to increase the severity of cavitation that can be imposed on the model.

A great deal of the analytical and experimental work on the water tunnel was concentrated on an investigation of the flow in the open-jet test section. This was necessary because of the complex nature of the flow in this component and because reports of previous investigations of confined jets were not available.

B. Pressure Distribution

As stated previously, it is desirable that the test body or model propeller be tested in a flow field which initially has uniform velocity and pressure in order to simulate prototype operation. It is possible to design the open-jet test section so that this condition will be obtained. However, as will be shown, such design probably would not be feasible because it would limit the scope of tests that could be made in the open-jet test section.

The flow process in the open jet is exceedingly complex because of the absence of solid boundaries which confine the stream. The jet is allowed to establish its own flow pattern in response to the varying forces imposed upon it by the test bodies or propellers. For example, in testing propellers under normal driving conditions, momentum is added to the stream so that the jet contracts behind the propeller. The thrust which is exerted on the jet acts in the downstream direction and energy is added to the flow. If the test simulates conditions where the propeller is used as a brake in decelerating a ship, the resultant thrust on the jet is in the upstream direction, and the

jet is decelerated and expands in passing through the test chamber. It is this adaptability of the open jet which makes it superior to a closed jet in testing large models. A relatively small blockage of a closed jet can set up large variations in pressure because the flow path is restricted by solid boundaries. These pressure differences are not nearly so large in an open jet, but the design of a satisfactory pick-up cone is made difficult because the cross-sectional dimensions of the open jet change with different test conditions. However, the same pick-up cone must serve to conduct enough flow into the diffuser throat to maintain continuity of discharge with minimum disturbance for all operating conditions. At the same time, the open-jet test section should have a pressure distribution as uniform as possible both axially and laterally before the propeller is put in the flow.

If the water tunnel contraction is properly designed, the nonuniformity of pressure in the core of the jet determines quantitatively the amount of nonuniformity of velocity. This convenient relation is a result of the core flow having uniform velocity when it is discharged from the contraction. Since no shear forces can be established unless a velocity gradient exists, there is no dissipation of energy in the core flow and the total head of each stream tube is constant. Thus, if the core pressure rises, the velocity in the core must decrease and the stream tubes will increase in area and vice versa.

Considering the entire flow process in an unconfined submerged jet, it is clear that no large pressure differences can develop. Since there are no solid boundaries for the jet to react against, pressure differences can exist only if there is a change in direction along some stream line. Defining any flow not in the original direction of the jet as a secondary flow, the magnitude of the pressure differences is directly dependent upon the secondary flows set up in the diffusion of the unconfined jet. Theoretical considerations indicate that such pressure variations amount to a fraction of 1 per cent of the velocity head [9]. Thus, if the chamber surrounding the jet were large enough and if the passages leading into the throat of the diffuser were designed to follow closely the stream surface of the unconfined jet, it is probable that no large pressure differences would exist in the core of the open-jet test stream.

The condition of uniform total head in the core flow dictates that the pressure must rise if the stream is directed into a pick-up cone whose

diameter is too large. The core stream tends to accelerate all of the fluid in a conduit into motion; if part of the fluid is at rest, the velocity gradient between this fluid and the fluid in motion tends to accelerate the stationary fluid and decelerate the moving fluid. Since continuity of flow is maintained in the passages leading to the diffuser, the core flow must decelerate, which in turn causes the pressure to rise. Likewise, if the stream is directed into a pick-up cone whose diameter is too small, the pressure in the core must drop. For this condition, the core flow must accelerate to maintain continuity of discharge, the stream tubes will contract, and the pressure is thereby decreased.

If solid boundaries force an incompressible fluid stream to undergo a change in velocity, the deceleration or acceleration occurs gradually. Hence, the changes in velocity and pressure brought about by the two conditions explained above cannot be expected to occur without influencing the flow upstream of the pick-up cone, even though this region is not directly in contact with solid boundaries. If the pick-up cone is designed so that a pressure rise occurs, a gradual increase in pressure in the open-jet test section preceding the cone must be expected.

It would appear superficially that the best pick-up cone is one which will cause no change in the core velocity. A possible design for such a pick-up cone is shown in Fig. 26. The sharp leading edge of the cone is designed to intercept the stream surface which is an extension of the boundary of the contraction. The inside boundary of the pick-up cone is drawn to have the shape of a parabolic transition 3 in. long, like the one used in the closed-jet test section (Part IV). If there were no gap behind the pick-up cone, the pressure changes brought about by the changing internal area of the pick-up cone could be exerted against the boundaries of the pick-up cone and would not be expected to influence the pressure in the open-jet test section. The core flow in the open jet would not be required to change in speed because the stream tubes would not have to contract or expand as they entered the pick-up cone. The extra fluid which would be entrained by the diffusion process would be peeled off by the leading edge and recirculated in the test chamber. The design of this cone is based upon reasoning that the chamber around the jet is large enough so that the diffusion at the edge of the jet takes place in the same manner as in an unconfined jet. (The mechanics of the diffusion process will be set forth below in the discussion of velocity distribution.)

Although this pick-up cone would probably give good results in an undisturbed jet, it was not tested in the model tunnel because it is apparent that deviations from ideal conditions would occur in the prototype tunnel under actual conditions of testing model propellers. As already noted, if the thrust exerted by a test propeller on the jet acts in an upstream direction, the jet expands and would have to contract sharply and accelerate in entering the pick-up cone in order to maintain continuity of discharge. The stream entering the pick-up cone would then tend to strike the lip of the cone at an angle, and separation would occur inside the cone. Separation at the entrance would result in a very poor velocity distribution in the throat of the diffuser where it is essential to have the velocity distribution as uniform as possible in order to attain high efficiency. These undesirable consequences could be alleviated somewhat, but not eliminated, by moving the pick-up cone upstream so that there is a gap between the downstream end plate of the test section and the pick-up cone. Some fluid from the test section chamber could then flow into the diffuser through this annular opening, thus decreasing the amount of flow that would have to enter through the pick-up cone to maintain continuity of discharge.

If a propeller exerts a thrust in the downstream direction, the jet contracts and the pick-up cone would tend to conduct too much discharge into the diffuser. The surplus discharge would have to be spilled by reversal of flow in the pick-up cone if there is no gap between the cone and the downstream end plate. If a gap is provided, some of the excess discharge could be spilled downstream of the pick-up cone. For either direction of thrust, conditions would be somewhat alleviated by the pressure differences necessary to cause spilling or filling of the pick-up cone. If the thrust is in the upstream direction, the pressure in the pick-up cone would have to be less than the pressure in the test section chamber to cause a flow into the gap. This, in turn, would tend to accelerate the flow into the cone, recontracting the stream and making less filling necessary. Similar reasoning applied when the thrust acts downstream shows that less spilling results. The increase or decrease in pressure is dependent upon the amount of spilling or filling required and upon the width of the gap behind the pick-up cone.

In summary, it appears that flow into the pick-up cone of Fig. 26 might be quite satisfactory when the model propeller is accelerating the jet and adding energy to the flow. The spilling action would tend to improve the

distribution of velocity in the diffuser throat and the flow would not tend to separate at the upstream lip of the pick-up cone. However, if the model propeller were backing into the flow, or if a stationary test body were mounted in the jet, the stream would impinge at an angle on the upstream lip causing separation on the inside of the cone. Of more importance, this condition might also cause the pick-up cone to be the initial source of cavitation in the tunnel, depending upon the pressure distribution caused by the entry misalignment. For these reasons, this design is not considered satisfactory for the intended application.

The two pick-up cones actually tested are shown in Figs. 27 and 28. These cones were mounted in the tunnel so that the gap between the downstream surface of the pick-up cone and the downstream end plate could be varied from 0 to 5/8 inch.

The larger pick-up cone, which had a length of 3 in. and throat diameter of 6 5/8 inches in the model, was the original design for the prototype water tunnel. The diameter of the leading edge of this cone was designed to be large enough to enclose all of the zone of diffusion when no test body is in the jet [1]. The primary advantage of this design is that it does not force the high-velocity regions of the jet to impinge at an angle on the leading edge of the cone. Its main disadvantage is that it conducts too much flow into the diffuser throat, causing a rather severe retardation of and pressure rise in the jet core. The magnitude of the pressure rise is shown in the test data of Fig. 29. Test data were obtained by using the dynamometer shaft extension and plunger described in Part I. The pressure at each of 29 taps spaced 3/8 in. apart was determined at test section velocities of 18, 30, and 48 fps for a given pick-up cone gap. The pressure difference between the tap farthest upstream and any other tap was then computed, and the three dimensionless pressure coefficients for each tap, based on test section velocity head, were averaged. The curves in Fig. 29 were computed by averaging the pressure coefficients at every possible group of four adjacent taps. It is believed that the pressure distribution with the shaft extension in the flow is not appreciably different from the unoccupied tunnel pressure distribution, since the shaft extension had relatively little area blockage.

The effect of the pick-up cone gap on the pressure distribution is apparent in Fig. 29. With zero gap, it is necessary that spilling occur by reversal of flow at the outside edge of the jet. This requires a higher

pressure inside the pick-up cone than if the gap is open and the excess flow spills through the gap. The pressure increase required to cause spilling is slightly less with a 5/8-in. gap than with a 5/16-in. gap.

The rate of retardation of the core flow in the open jet can be computed from Fig. 29. Since the sum of pressure head and velocity head is constant in the core, for each increase of 0.01 in the pressure coefficient there is an accompanying decrease in velocity of 1/2 of 1 per cent. For purposes of comparing the larger and smaller pick-up cones tested, it may be noted that the distance along the open jet measured from the end of the contraction in which a pressure increase of 0.01 $V_o^2/2g$ and a velocity decrease of 1/2 of 1 per cent occurs is 3.1, 2.8, and 3.5 in. for pick-up cone gaps of 0, 5/16, and 5/8 in., respectively.

The dashed-line curve in Fig. 29 represents, to a suitably reduced linear scale, the pressure distribution in the existing 24-in. open-jet water tunnel at Taylor Model Basin [1]. This curve has been computed using the pressure at the upper boundary of the test section chamber as a reference, while the pressure distribution for the model was computed using the core pressure at the end of the contraction as reference*. The pressure curve for the jet of the 24-in. tunnel indicates that the jet is still converging after it leaves the contraction. It is noteworthy that the pressure at the three traverse stations in the boundary of the test section chamber of the model was 0.01 $V_o^2/2g$ less than the core pressure at the end of the contraction. It appears from Fig. 29 that the model design offers substantial improvement in test section pressure conditions, although much of the improvement may be attributed to the superior contraction design.

The second pick-up cone tested was designed in an attempt to reduce the velocity retardation in the test section. This cone is shown in Fig. 28 and was designed to have a length of 2 in. and throat diameter of 6 3/8 inches in the model. It was reasoned that the smaller throat diameter would lessen the amount of retardation in the core and that shortening the cone would delay somewhat the pressure rise in the core, since the stream retardation is primarily caused by pressures built up against solid boundaries. The throat diameter was purposely made large enough so that some retardation would take

---

*Throughout this report, "pressure" actually means the sum of the static pressure and elevation head, or the so-called piezometer pressure.

place. This was necessary because the pressure has to be greater in the pick-up cone than in the chamber surrounding the jet in order for spilling to take place. If the throat diameter were too small, the pressure would have to be higher in localized peripheral areas than at the center of the core. This would necessarily result in distortions of transverse velocity and pressure distributions which would be detrimental to flow in the diffuser.

The improvement brought about by the smaller cone can be seen by comparing Figs. 30 and 29. The distance from the contraction in which a pressure increase of 0.01 $V_o^2/2g$ and a velocity decrease of 1/2 of 1 per cent occurs is 4.25, 3.9, and 2.4 in. for pick-up cone gaps of 0, 5/16, and 5/8 in., respectively. The change was not as great as had been desired or expected, but a definite improvement is evident. An important secondary advantage of the smaller pick-up cone is that the length of the alternate closed-jet test section (Part IV) can be increased from less than 1/2 diam to almost 1 diam. For these reasons the smaller pick-up cone was recommended for use in the prototype water tunnel.

The amount of energy actually lost in the open-jet test section was not determined, mainly because the lateral variations in static pressure could not be measured with suitable accuracy in high-velocity regions. The open-jet test section and main diffuser were, therefore, treated as one component in computing head loss, and the model experiments (Part V) showed that the total head loss in these two components was about 0.01 $V_o^2/2g$ greater with the 6 3/8-in. pick-up cone than with the 6 5/8-in. pick-up cone. This amounts to a 4 per cent increase in head loss and energy requirement for the tunnel circuit, but the prototype pump will be operating in a range where this increase in head will not appreciably affect the maximum test section velocity available. The pressure distribution in the prototype open-jet test section should be the same as in the model (Fig. 30) with a four-fold increase in the linear scale.

An examination of the possible existence of pressure pulses in the jet is of interest because some open-jet wind tunnels have exhibited rapidly pulsing flow which excited vibrations in the structure. In the case of the wind tunnels, it was shown that the pulsations were the result of more air being conducted into the diffuser by the flaring pick-up cone, or exit nozzle, than was being discharged by the contraction. This excess discharge was continually being forced into the circuit, and when the pressure in the diffuser

had built up to a sufficiently high value, some of the flow momentarily reversed in direction and was forced out backwards through the diffuser throat. Rapid repetition of the filling and spilling cycle resulted in pressure fluctuation of high magnitude. The condition has been alleviated either by placing deflectors in the jet so that not so much air was carried into the diffuser or by making holes in the diffuser so that the excess flow could be spilled without backflow occurring. This same function will be served by the gap between the pick-up cone and diffuser in the water tunnel. Since the gap will be adjustable, it will be possible to allow for the necessary steady spilling, or filling in some cases, at the diffuser throat. It seems unlikely, however, that pressure fluctuations of appreciable magnitude could be set up in an open-jet water tunnel if the test section chamber is maintained full of water. Water being relatively incompressible, only a very small quantity of fluid could be drawn out of the test section chamber before the pressure differences would be large enough to cause backflow spillage. Since a relatively great discharge is being continuously circulated, the resultant cyclic pressure pulses would be very small and of high frequency. The above reasoning would not apply if there were a large amount of gas in the test section chamber, either in the form of cavitation or air bubbles, or as a large pocket of air. An appreciable amount of water could then be drawn out of the test section chamber and the volume of the gas pockets could be increased if the tunnel walls were sufficiently elastic or if gas pockets existed in other portions of the circuit. This relatively greater mass of water could then surge in and out of the test section chamber and cause noticeable pulses. This condition was actually observed in the model when it was operated at low pressure and high speed so that a large number of gas bubbles were present in the fluid. A distinct throbbing of about 30 cycles per second could then be heard. The throbbing could not be observed if the tunnel pressure were raised so that the gas bubbles were dissolved.

C. Velocity Distribution

Velocity traverses made in the open-jet test section were measured using the 1/4-in. Pitot cylinder described in Part I. Three traverse stations, designated as Stations 1, 2, and 3, were located respectively, 1 5/16 in., 2 7/8 in., and 4 7/8 in. downstream of the contraction (Fig. 27). Traverses were made on horizontal and vertical diameters at test section speeds of 18,

30, and 48 fps and at pick-up cone gaps of both 0 and 5/8 in., with the 6 5/8-in. pick-up cone installed both with and without the contraction dynamometer shaft, and with the 6 3/8-in. pick-up cone installed.

Early in the testing program it was confirmed that neither the test section speed nor the pick-up cone gap had a noticeable effect on the dimensionless velocity distribution. It was expected that the dimensionless velocity distribution would be independent of the test section speed within the range tested, since numerous other investigators had previously shown that free-turbulence diffusion processes are only slightly, if at all, affected by Reynolds number. This independence occurs because the shearing action is not exerted against solid boundaries along which a laminar sublayer can develop. Rather, the shear forces set up in the diffusion region at the boundary of the jet are the result of momentum transport between finite quantities of fluid, a process which is independent of Reynolds number once it has been fully developed. The large velocity discontinuity set up at the end of the contraction insures that the fully turbulent state will be reached at quite low velocities.

It is reasonable that the measured velocity distribution should be independent of the pick-up cone gap if it is remembered that the Pitot cylinder measures the total head at a point. The velocity head was computed by subtracting a constant pressure head from this measured total head; the pressure head to be subtracted was determined by measuring the head on the Pitot cylinder opening when it was near enough to the wall of the test section chamber so that there was no consistent variation when the Pitot cylinder was rotated through 360°. Therefore, even though the jet core pressure was higher and the core velocity correspondingly lower for some conditions than for others, the measured total head and computed velocities were constant in the core for all conditions. The mean pressure in the dead-water region outside of the jet showed no consistent or appreciable variation either in a longitudinal direction or for different pick-up cone conditions. This indicates that the mean pressure in the diffusion region was very nearly constant for all conditions of flow, and thus that the diffusion process and velocity distribution in the boundary of the jet should not change for different conditions at the pick-up cone.

It should be noted here that the velocity distributions computed from the total head traverses may be appreciably in error in the low-velocity

regions of the diffusion layer. The manometer reading obtained with the Pitot cylinder represents the mean of the velocity head and pressure fluctuations at a point. The square root of this mean total head, when interpreted as a velocity, is larger than the mean velocity which actually exists at the point. The error will be dependent on the ratio between the mean velocity and the root mean square velocity fluctuations; this ratio is large in regions of low velocity.

Typical velocity distributions measured in the open-jet test section are shown in Figs. 31, 32, and 33. All of these curves are plotted so that the left side of traverses on horizontal diameters corresponds to the side of the tunnel nearest the control tower (Fig. 4), and the left side of traverses on vertical diameters corresponds to the outside of the tunnel loop. This convention is adhered to throughout the report. It will be noted that the measured velocity distribution in the core is satisfactorily uniform; the average variation in the velocity is 1 per cent, except when the contraction dynamometer shaft is installed in the tunnel. When this shaft is installed, both the struts which support the shaft and the shaft itself leave quite noticeable wakes in the test section. The wake of the shaft itself is exhibited as a zone of increasing lateral extent in which the velocity deficiency is steadily being reduced.

As shown in Fig. 6, the contraction dynamometer shaft terminated in a pointed tailpiece which extended 1 1/2 in. into the test section. Since in the prototype installation, the shaft will terminate at the hub of the model propeller, the shaft itself will not cause a free-turbulence wake. For this reason, this type of wake will not appear in the prototype; the data are presented only so that some estimate of the disturbance produced by the boundary layer of the shaft can be made. It might also be noted that the shaft wake broadens faster in the horizontal direction than it does in the vertical direction; this is probably due to some misalignment in the tunnel and would invalidate conclusions drawn from the model studies concerning the wake of the shaft.

The wakes of the struts which support the dynamometer shaft are a source of more useful information. Two sets of three struts each were used to support the shaft; the position and size of these struts are shown in Figs. 6 and 9. The wakes are evident only in the traverses on vertical diameters in Figs. 31, 32, and 33. No information concerning the lateral extent of the

wakes is available from the traverses with the Pitot cylinder, since traverses could be made only along a diameter. For this reason a special Pitot tube was constructed which could be traversed on any tangential line by rotating the instrument about its axis (Fig. 22a). The effect of yawing the Pitot tube was determined by calibrating it in a region of the jet which the wakes did not affect. The lateral extent and velocity deficiency of the wakes of the struts is shown in Fig. 34, as determined when the tip of the Pitot tube was 1 in. from the end of the contraction and 1 1/2 in. from the axis of the test section. These same dimensionless values should also be applicable to the prototype, since here again it is a case of free-turbulence mixing which is unaffected by Reynolds number. The fact that the wakes are almost exactly diametrically symmetrical in the cross section measured indicates that the flow in the model is satisfactorily free from rotation. All of the supporting struts in the prototype are to be installed with included angles of 115° or 130° to avoid synchronization of the strut wakes with the blades of a three-bladed model propeller.

After the above tests were completed, it was decided at Taylor Model Basin that the strut system tested in the model would not adequately support the dynamometer shaft in the prototype. Three additional struts having thicknesses of 0.22 in. and chords of 6.6 in. with their leading edges 27.3 in. from the downstream end of the contraction have been designed to remedy the support problem in the prototype. The influence of the three additional struts in the prototype tunnel can be computed with acceptable accuracy, since a great deal of analytical and experimental work has been done on wakes in a uniform pressure field. This has been especially developed in aeronautical research because the profile drag of a wing section can be computed from a survey of the velocity deficiency in the wake of the wing.

The following analysis of the strut wakes is based on work reported by Silverstein [8], which was conducted on a series of NACA symmetrical four-digit airfoils of varying thickness ratio. Since the thickness ratio of the struts is somewhat smaller than that of the finest airfoil tested, it is necessary to extrapolate the data to determine one of the constants in the semi-empirical equations that will be used. The difference between the thickness distribution of the tunnel struts and the NACA four-digit series will not introduce appreciable error. The variation in static pressure in the wake

caused by secondary flows in the wake and the presence of the strut can be computed from the semi-empirical equation,

$$\frac{\Delta p}{q_o} = \frac{t/c}{(0.77 + 3.1\xi)^2} \tag{1}$$

where Δp is the pressure excess in the wake,

q_o is the stagnation pressure,

t/c is the thickness ratio of the strut, and

$\xi = x/c$ is the distance behind the trailing edge in chord units.

Substituting $t/c = 0.033$ and $\xi = 3.14$ in Eq. (1) shows that $\Delta p = 0.0003\ q_o$, which insures that the pressure measured by piezometer taps at the lip of the contraction will not be affected by the strut wakes.

The width of the wake can be computed from the formula,

$$\zeta = K\ (\xi + 0.15)^{1/2} \tag{2}$$

where ζ is the wake width measured in chords, and

K is the numerical constant dependent on coefficient of drag.

Extrapolation of values given by Silverstein indicates that K will equal 0.050 for the assumed drag coefficient of 0.0032 (Part II). Substituting appropriate values shows that the wake width will be 0.60 in. at the end of the contraction. The maximum total head deficiency can be computed from the formula,

$$\eta = \frac{0.170}{(\xi + 0.05)^{1/2}}$$

where η is the ratio of the total head deficiency at the center of the wake to the total head of the free stream. Substituting appropriate values shows that the maximum total head deficiency at the end of the contraction will be 9.5 per cent of the free-stream velocity head. The above conclusions must be modified somewhat because there will be a pressure drop of $0.13\ V_o^2/2g$ and an area contraction of 94 per cent between the strut centerline and the end of the contraction. If it is assumed that the same energy difference exists between the wake centerline and the undisturbed stream at the end of the contraction that would exist if the pressure and velocity field were constant downstream of the strut, the resulting minimum velocity in the wake will be

0.957 V_o. The wake width will probably be reduced as the square root of the area ratio, indicating that the wake width will be 0.58 in. at the end of the contraction. The probable distribution of velocity in the wake is shown in Fig. 34.

The velocity traverses in Figs. 31, 32, and 33 show quite graphically the increase in extent of the diffusion zone at the boundary of the jet. The distribution of velocity in this region follows closely the theoretical velocity distribution determined by Tollmien [9] for the turbulent diffusion region of plane jets in a field of uniform pressure. Tollmien's analysis is based on the experimentally verified assumption that the width of the diffusion region increases linearly with x, where x is measured in the direction of flow from the point where mixing begins. Corrsin [10] has pointed out that the linear spread of the diffusion region results from the dynamic similarity of the mean and turbulent motions. This similarity is not strictly valid in the zone of establishment of axially symmetric jets. However, experiments and an approximate analysis by Keuthe [11] have shown that the velocity distribution in the upstream portion of the zone of establishment of axially symmetric jets should be, for practical purposes, the same as the distribution in two-dimensional jets. Intuitively, this would seem to be true in regions where the thickness of the diffusion region is small compared to its radius of curvature, as it is in the open-jet test section.

The velocity distribution to be expected from a direct application of Tollmien's analysis is shown in Figs. 35a and 36a. Figure 35a shows that the theoretical lines of constant velocity in a plane through the axis of symmetry will be straight lines. The rate of spreading of the diffusion region and of the lines of constant velocity had to be determined experimentally by Tollmien, and the constant determined by him ($\sqrt[3]{2c^2} = 0.0845$) has been used in plotting Fig. 35a. Figure 36a shows the same velocity distribution plotted in a manner similar to Figs. 31, 32, and 33. The distance x, which is the distance from the end of the contraction to the hole on the Pitot cylinder which measured the total head, has been corrected from the distances given in Fig. 27 to take into account the deflection of the Pitot cylinder caused by drag on the Pitot cylinder at a test section velocity of 30 fps.

One modification of Tollmien's analysis was necessary to bring the measured velocity distribution into good agreement with the theory. The theoretical analysis is only strictly valid for a flow system in which the distribution of velocity is absolutely uniform (zero boundary-layer thickness) up

to the point where the diffusion process begins. If a boundary layer does exist in the conduit (which, of course, must be the case for any real fluid) the retardation of the fluid near the walls of the conduit would measurably affect the diffusion process immediately adjacent to the end of the conduit. Experimental evidence of this influence has not been reported in any of the available published reports on turbulent jet diffusion. Failure to detect the boundary-layer influence in the reported investigations on circular jets may be attributed to the fact that measurements were not made at distances less than 1/2 diam from the end of the contraction. In addition to influencing the velocity distribution immediately downstream of the contraction, the boundary layer should have the effect of making the diffusion process appear to start at some section upstream of the lip, since the fluid in the diffusion layer is somewhat retarded even before it leaves the contraction. Also, it would be expected that the diffusion layer would be shifted towards the center of the jet by a distance equal to the displacement thickness of the boundary layer at the end of the contraction. This last factor would ordinarily be of little importance since the displacement thickness is ordinarily of the order of 1 per cent or less of the jet diameter.

The influence of the contraction boundary layer on the diffusion process in the model can be seen in Figs. 35b and 36b. If the hypothetical apex of the diffusion layer is shifted 0.60 in. upstream and 0.08 in. outward from the lip of the contraction, this resulting modified theoretical velocity distribution is in good accord with the experimental data. The outward shift of the apex is in the opposite direction from that hypothesized as due to the displacement thickness. The pick-up cone is retarding the core of the jet, which explains this discrepancy for this particular case. This retardation results in a slight expansion in order that continuity of discharge in the core may be maintained. In Fig. 37, the experimental data and the modified theoretical velocity distribution in the open jet are compared. The plotted points were chosen at random from data taken at the three different velocities and with different forms of the pick-up cone.

The velocity distribution at Station 1 was appreciably influenced by the boundary layer in the contraction. The agreement at the two stations farther downstream from the contraction is quite satisfactory, indicating that the modified theoretical distribution will predict the flow conditions in the prototype with sufficient accuracy. This conclusion implies that: (1) the

experimental constant determined by Tollmien is applicable for the present installation, (2) the diffusion process is not appreciably affected by Reynolds number, and that (3) rational reasons have been hypothesized for modifying the theoretical velocity distribution which will be equally applicable to model and prototype. Actually, the contraction boundary layer will have somewhat less influence in the prototype than in the model, since the boundary layer will be relatively thinner at higher Reynolds numbers. Any changes brought about by this small dissimilarity between the model and prototype are not thought to be important. A direct application of the model results indicates that the nominal boundary of the prototype jet core will have a diameter of 23.0 in. at the end of the contraction and a 20-in. diameter 24 in. downstream of the contraction, if the jet core is assumed to extend to where the velocity is 99 per cent of the centerline velocity.

D. Test Stream Turbulence

If Reynolds number is an important variable in testing a model in the prototype tunnel, it is of some importance to know the amount of turbulence in the test jet in order to interpret the test results accurately. This fact has long been recognized in aeronautical research, and in the past it has been the practice to determine the so-called turbulence factor of a wind tunnel before putting it into operation. The turbulence factor used to be conventionally determined by employing a turbulence sphere; this method has been superseded by more accurate methods. The improved methods are not sufficiently developed to permit their use with systems employing water as a fluid as in the present application; consequently, a turbulence sphere installation was constructed for use in the model. The turbulence sphere was used to determine the turbulence factor of the model tunnel both in its original form and with a simple modification intended to reduce the test section turbulence level.

The main effect of turbulence in the test stream is to cause an earlier transition from laminar to turbulent flow in the boundary layer of a test body. The point of transition of the laminar boundary layer in turn influences to a marked degree both the drag coefficient and the maximum left coefficient of an airfoil shape or of a blade section of a propeller. It is precisely this effect on transition that is measured with the turbulence sphere. It is well known that the coefficient of drag of a sphere decreases sharply as the Reynolds number is increased beyond a certain critical value.

If the Reynolds number is low enough, the boundary layer separates upstream of the equator of the sphere as a laminar boundary layer. As the Reynolds number is increased, the boundary layer becomes turbulent before separation, and separation occurs downstream of the equator, since the turbulent boundary layer can penetrate farther into the adverse pressure gradient at the rear of the sphere. This delayed separation results in a lowered coefficient of drag and a higher wake pressure. In air with very slight turbulence it has been found that the critical Reynolds number of the sphere (defined as the Reynolds number when the coefficient of drag is 0.3) is 385,000. The critical coefficient of drag occurs at lower Reynolds numbers with streams of higher turbulence. A discussion of the turbulence sphere is given in reference [12].

The actual drag of the turbulence sphere was not measured in these tests. A simplification of experimental procedure results from the fact that there is a unique relationship between the drag coefficient of the sphere and the pressure coefficient in the wake of the sphere. Defining the pressure coefficient of the wake (C_p) as the difference in pressure between the stagnation point and the wake of the sphere divided by the free-stream stagnation pressure, it has been determined that the drag coefficient of 0.3 corresponds to a pressure coefficient of 1.22 [12]. The critical Reynolds number for any stream may be obtained by measuring the variation of the wake pressure coefficient with Reynolds number and selecting, by interpolation if necessary, that value corresponding to a pressure coefficient of 1.22. The turbulence factor is obtained by dividing 385,000 by the critical Reynolds number for the given stream. Once the turbulence factor of a test stream has been determined, multiplication of this factor by the Reynolds number at which a test is being made gives the effective Reynolds number in a stream free of turbulence.

A simple procedure was used in determining the critical pressure coefficient. The difference in pressure between the stagnation hole of the sphere and the two holes in the supporting rod adjacent to the sphere was divided by 99 per cent of the pressure difference between the stagnation hole and a wall tap opposite the sphere in the cylinder surrounding the test section. The factor 99 per cent was used to take into account the 1 per cent $V_o^2/2g$ of static head difference previously measured between the jet axis and the boundary of the test section. The free-stream velocity used in computing the Reynolds number was also obtained from these measurements. In order to give

valid results, the turbulence sphere must be free from vibrations and must have a smooth surface. The original mirror finish of the Monel ball bearing which was used for the sphere was not damaged when the sphere was machined, and no vibrations of the sphere could be seen while measurements were under way, except at speeds much higher than critical. Experiments have shown [13] that the sting diameter was not large enough to influence the critical Reynolds number, and it is not thought that the steadying rods (which replaced the steadying wires shown in Fig. 23) were close enough to the sphere to influence the test results. The center of the sphere was 1 1/4 in. downstream from the end of the contraction; the variations in pressure in the vicinity of the sphere were so small (Fig. 30) that it was not necessary to correct for "horizontal buoyancy" on the sphere.

The results of the turbulence sphere tests are summarized in Fig. 38. The run made in the tunnel without turbulence control indicates that the critical Reynolds number was 254,000. After this run had been completed, a screen with 40 meshes to the inch and a wire diameter of 0.01 in. was installed at the flange 1 ft upstream of the contraction to damp the turbulence in the stream entering the contraction. Four runs were then made at water temperatures from 87° to 102° F to find the effect of varying the factors in Reynolds number. These four runs grouped very closely and indicated that the critical Reynolds number had been raised to 262,000. Since this improvement was less than had been expected, two more check runs were made the following day with results that scattered badly and indicated that the critical Reynolds number was lower with the screen than without it. Examination showed that the screen had not been broken or plugged. It is believed that these last two runs might be in error because of vibrations which were not visible to the eye being introduced into the system. Vibration of the sphere would tend to reduce the critical Reynolds number, so that the highest critical Reynolds number measured is most likely representative of the true turbulence existing in the stream. The first four runs with the screen installed gave the same critical Reynolds number even though the test section velocity varied between 22.6 and 26.9 fps, which gives some indication that vibration was not a factor in these runs. The turbulence factor for the model tunnel is about 1.5 on this basis.

The influence of both the scale and intensity of turbulence on the critical Reynolds number of a sphere has been investigated quite thoroughly.

It has been shown analytically and verified experimentally [12] that the critical Reynolds number is a function of the quantity

$$\frac{\sqrt{\overline{u^2}}}{U}\left(\frac{D}{L}\right)^{1/5}$$

where $\sqrt{\overline{u^2}}$ is the root mean square speed fluctuation in isotropic turbulence,

U is the free-stream velocity,

D is the diameter of sphere, and

L is the scale of turbulence (area under correlation curve).

Reference [12] indicates that a critical Reynolds number of 255,000 corresponds to a value of $(\sqrt{\overline{u^2}}/U\ (\frac{D}{L})^{1/5})$ of 0.014. Since neither the scale nor the intensity of turbulence could be measured in the model water tunnel, these two factors cannot be separated. However, reference [13], in which the critical Reynolds number of spheres as determined in test sections of various wind tunnels is plotted against the turbulence intensity alone, indicates that $\sqrt{\overline{u^2}}/U$ = 0.8 per cent.

The intensity and scale of turbulence in the test section are determined primarily by the vaned elbow and stilling length immediately upstream of the contraction and the area ratio of the contraction. The intensity of turbulence upstream of the contraction can be quite accurately controlled by the introduction of damping screens. The effect of damping screens is to break up the relatively large-scale turbulence caused by the cascade in the vaned elbow into fine-scale turbulence which decays rapidly in a short distance. According to Schubauer [14] a screen will decrease the intensity of turbulence by a factor

$$f = \frac{1}{\sqrt{1 + k}}$$

where k is the head loss coefficient of the damping screen. There is little definite information available concerning the effect of contraction of stream lines on turbulence intensity. If it is assumed that there is no decay in the contraction, it can be shown that the intensity of turbulence will be decreased in the longitudinal direction and increased in a transverse direction. However, the effects of contraction and decay can substantially cancel each other [14]. Whether or not this is the case, a reduction in intensity of turbulence by a factor f upstream of the contraction should cause an approximately equal reduction in the test section. The screen installed in the water

The test section was then put at the desired pressure and the test section velocity was increased until cavitation was observed. The first signs of cavitation appeared at $\sigma = 0.60$ and could be observed as occasional intermittent white flashes in the diffusion layer starting near the downstream end of the test section. At this cavitation index the noise produced by the cavitation was also intermittent. When the test section velocity was increased until $\sigma = 0.48$, several white streaks that appeared to start midway in the test section and end at the pick-up cone were always visible and the noise produced by the cavitation was steady. When the test section velocity was further increased until σ was as low as 0.40, cavitation was generally visible in the downstream half of the test section.

Under no conditions of operation, even when σ was as low as 0.20, was cavitation observed to form on any of the boundaries of the open-jet test section or diffuser. This was true with both pick-up cones tested and for pick-up cone gaps from 0 to 5/8 inch. The vapor pockets that were formed in the diffusion layer collapsed against the upstream portion of the pick-up cone, but it was apparent that there was no formation of cavities at this point. There was no observable cavitation in the upstream one-third of the diffusion layer at cavitation indices as low as 0.20.

Visual observation gave a false impression of the amount of cavitation which actually existed in the test section at an instant. At a test section velocity of 48 fps, the time that a vapor pocket remained in the test section was less than 0.01 sec. Consequently, persistence of vision gave the impression that the downstream end of the test section was entirely surrounded by vapor pockets at low-cavitation indices. That this was not the case can be seen in Figs. 39 and 40. These photographs were taken with a light source of 20-microsecond duration and give effectively instantaneous pictures of the cavitation in the test section. The test section velocities for all of these pictures was 48 fps, and the cavitation index was changed by lowering the pressure. The 6 3/8-in. pick-up cone was installed with the gap closed. Several photographs taken when σ was greater than 0.45 did not show any cavitation in the test section. This indicates that the frequency of formation of cavitation bubbles was so small at the higher pressures that there was little probability of a cavitation bubble being in the test section at a given instant. The photographs in Fig. 40 show the increasing severity of cavitation as the pressure and cavitation index are lowered. It will be noted that no cavitation bubbles are seen in the upstream half of the test section and that the cavitation seems to be more severe in the upper portion of the jet where

the absolute pressure is lower because of the effect of gravity. In the last two pictures, cavities can be seen collapsing against the pick-up cone. The fine-grained spherical bubbles in these pictures are air bubbles that were drawn out of the water at low pressures and held in suspension in the water surrounding the jet. When these bubbles were in the flow, it was quite clear that the recirculating vortex set up by spilling from the cone was confined to the downstream half of the test section. This is not thought to have any effect on cavitation, but it does indicate that the refinement of hollowing the upstream end plate of the test section is wasted. When the tunnel had been operating for only a short time at low pressure, the test section chamber became so filled with air bubbles that it was impossible to see through to the jet. This could be a serious limitation on the operation of the prototype if it is desired to photograph cavitation on test bodies. Indications were that the model was 80 per cent saturated with air at atmospheric pressure when most of the tests were made. If the prototype tunnel can be deaerated to lower values, the presence of these air bubbles in the test chamber will not be detrimental.

The application of the model cavitation tests to the prototype is quite direct, since the cavitation is caused by pressure fluctuation in a free-turbulence process which is effectively independent of Reynolds number. Theoretically [17],

$$\frac{\sqrt{\overline{p}^2}}{w} = K \frac{\overline{u}^2 + \overline{v}^2 + \overline{w}^2}{2g}$$

where $\sqrt{\overline{p}^2}$ is the root mean square pressure fluctuation,
$\overline{u}^2$, $\overline{v}^2$, $\overline{w}^2$ are mean square velocity fluctuations, and
K is the constant of order unity.

It has been confirmed experimentally [18] that the mean square velocity fluctuations are constant along one of the lines of constant velocity in Fig. 35, when the free turbulence has been fully developed. The constant K depends upon the form of the eddy, and since the mean eddy form will be similar in model and prototype, it seems safe to say that the root mean square pressure fluctuation in model and prototype will be equal. These mean square pressure fluctuations should also be constant along a line of constant velocity, but the thin boundary layer in the contraction evidently has the effect of suppressing the velocity fluctuations in the upstream portion of the model test section. This, combined with the fact that it takes a cavitation pocket a finite amount

of time to be formed, explains why the upstream end of the test section in the model tunnel was free of cavitation. A few inches of the upstream portion of the prototype tunnel should likewise be free of cavitation at low-cavitation indices, but it is unlikely that this length will equal one-half test section diameter as it did in the model. Cavitation should first be evident when the cavitation index at the top of the jet falls to 0.60 and should be generally visible when σ is as low as 0.40, according to the results of the model studies. If the air content of the prototype tunnel water is quite low, the incipience of cavitation may be delayed somewhat.

F. Conclusions

On the basis of these experimental and analytical studies of the open-jet test section, it is concluded that:

1. The pick-up cone in the prototype tunnel should be constructed to correspond to the smaller pick-up cone tested in the model.

2. There will be a 6 per cent retardation in velocity and an accompanying rise in pressure in the core flow as it passes through prototype test section.

3. The diameter of the core of uniform total head will vary from 23 in. at the upstream end to 20 in. at the downstream end of the test section.

4. There will be an approximate 1 per cent radial variation in velocity in the core flow.

5. The contraction dynamometer shaft and its supporting struts will leave appreciable wakes in the test section.

6. Intermittent cavitation will begin in the diffusion region above the core of uniform head when the cavitation index at the top of the test section falls to 0.50.

7. The root mean square isotropic turbulence intensity in the core flow will be about 0.8 per cent; this intensity can be reduced by installing several screens upstream of the contraction.

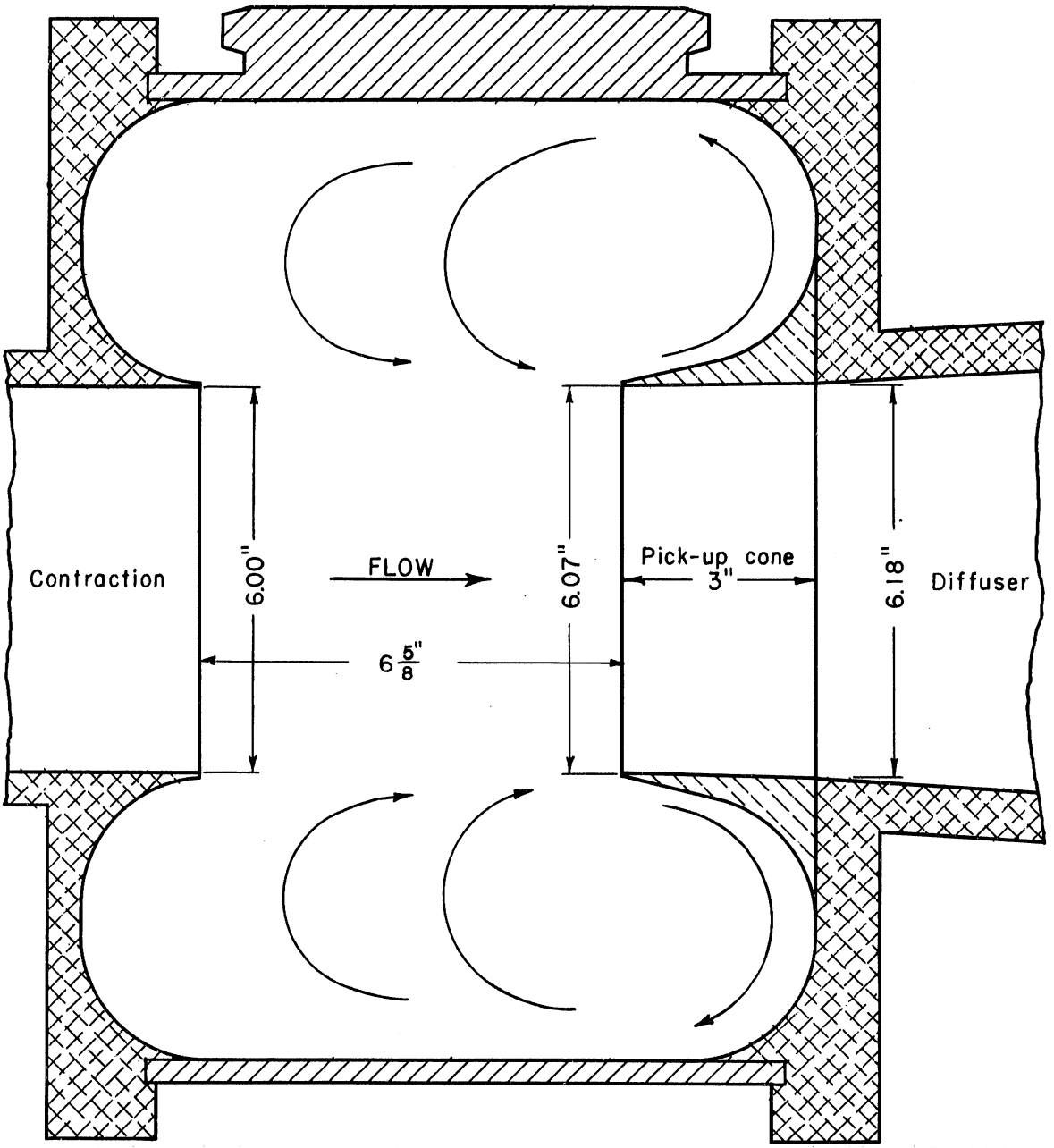

Fig. 26 - Suggested Design of Open-Jet Test Section to Provide Uniform Velocity and Pressure in Jet Core

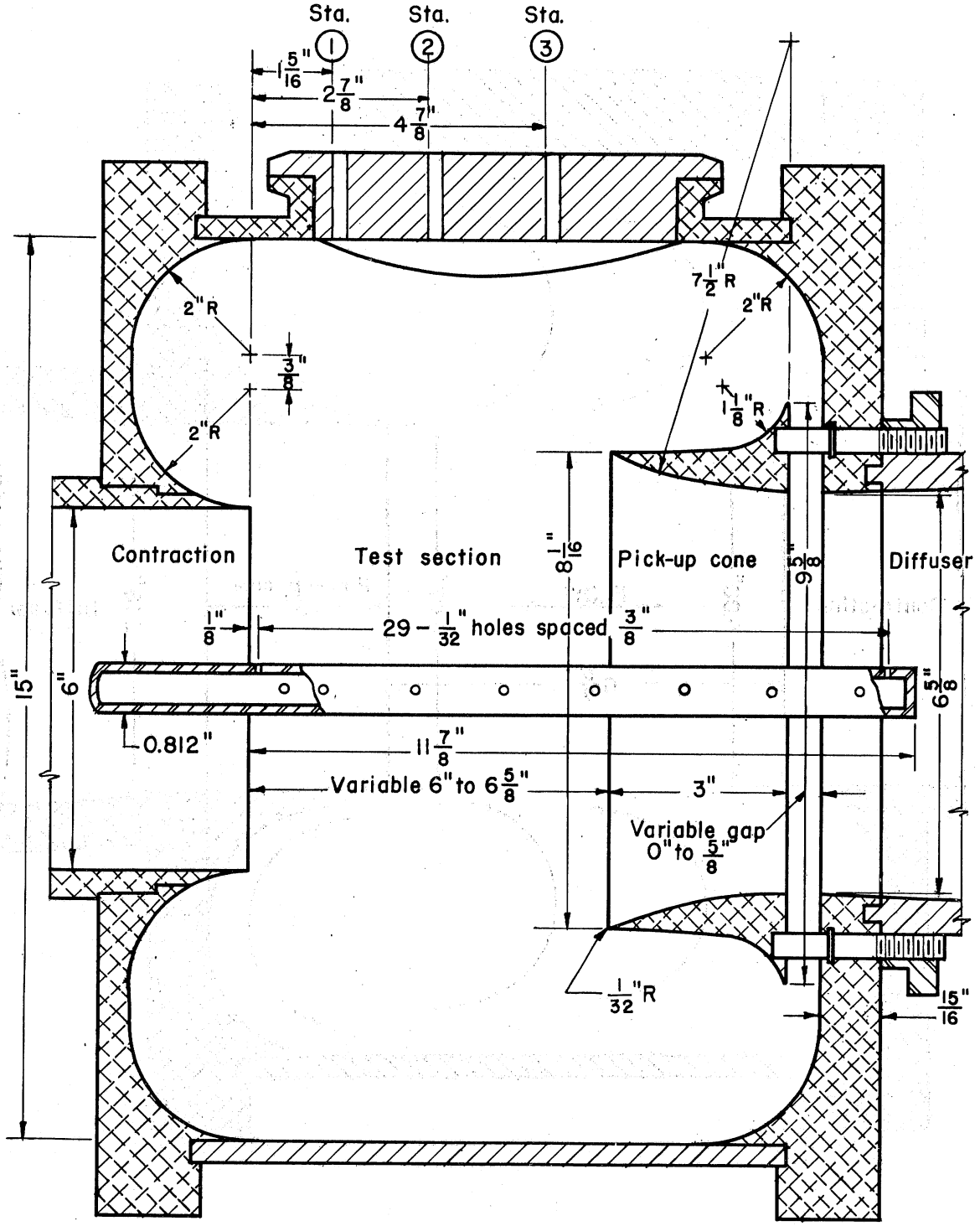

Fig. 27 - Model Open-Jet Test Section with 6 5/8-in. Pick-Up Cone and the Contraction Dynamometer Shaft Extension Used for Measuring Axial Pressure Variation

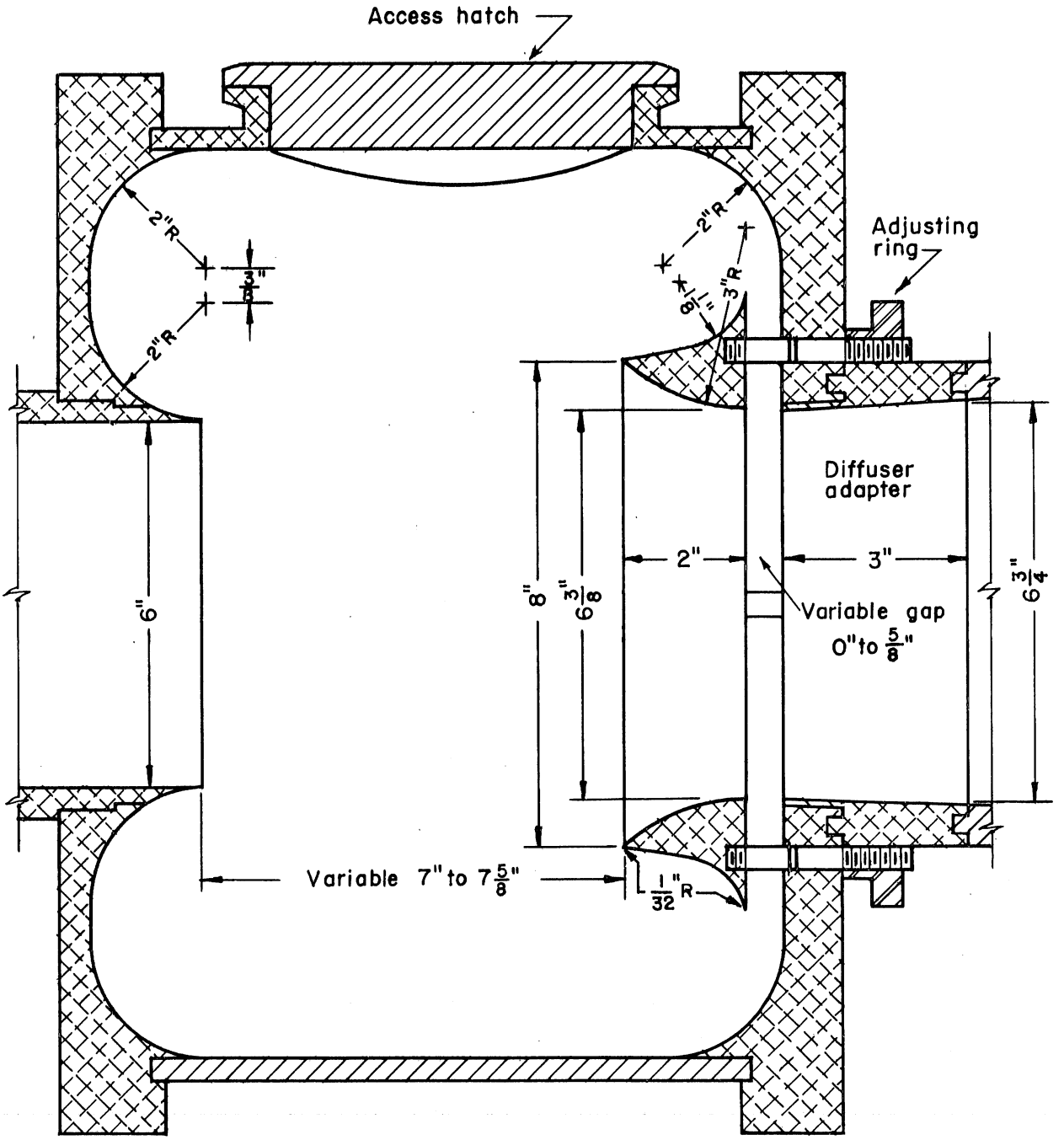

Fig. 28 - Model Open-Jet Test Section with 6 3/8-in. Pick-Up Cone

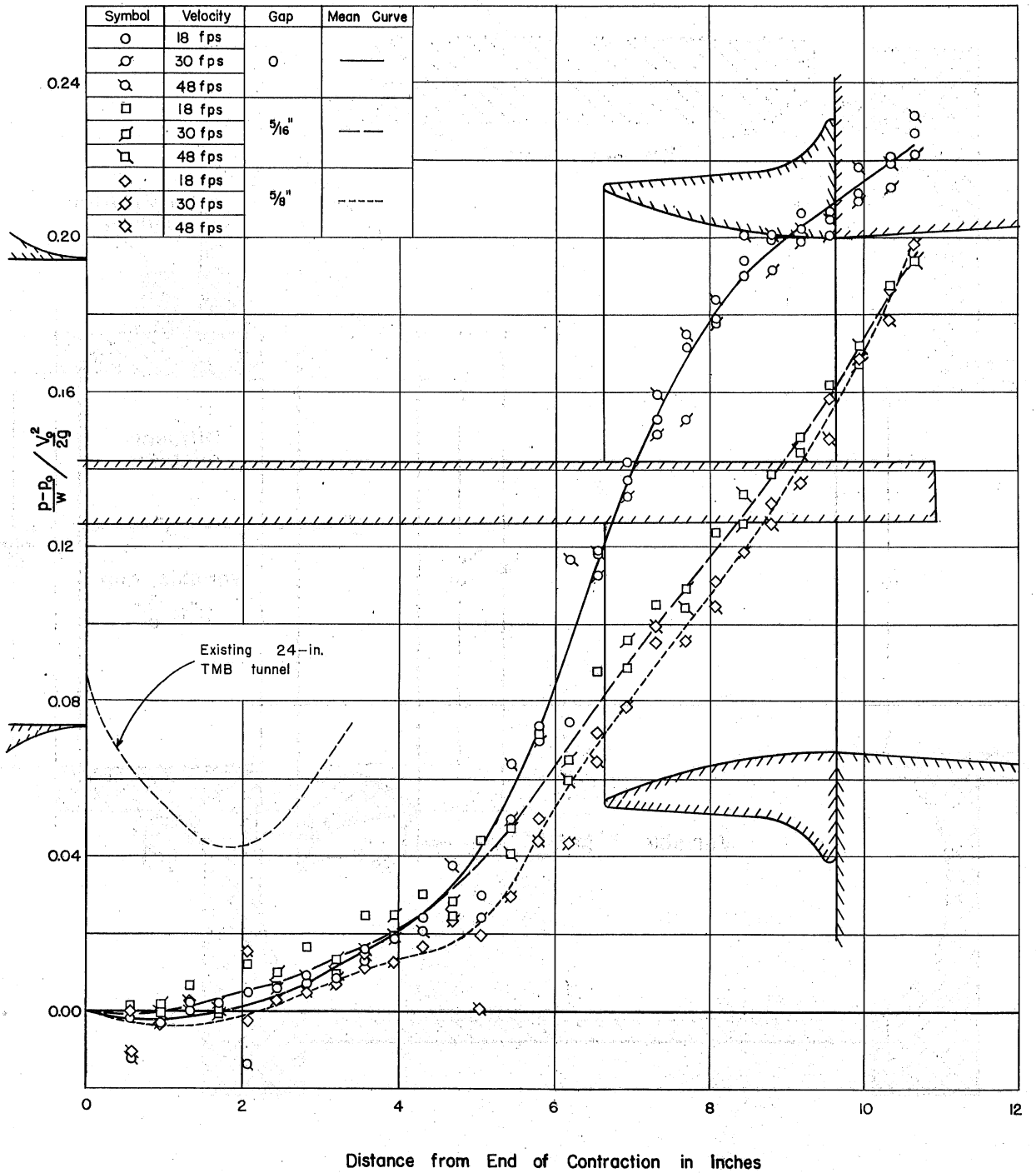

Fig. 29 - Axial Pressure Variation in Open-Jet Test Section with 6 5/8-in. Pick-Up Cone

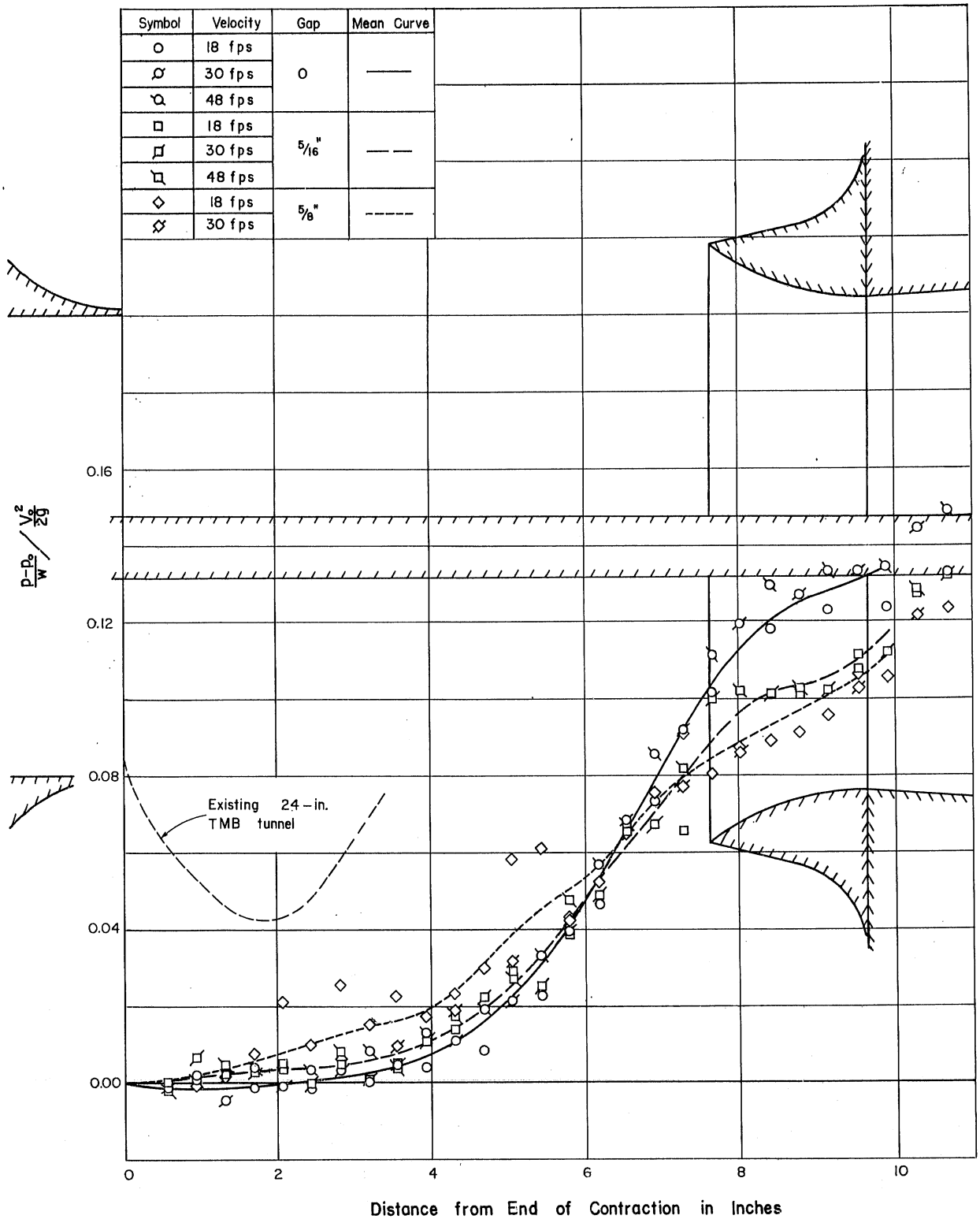

Fig. 30 - Axial Pressure Variation in Open-Jet Test Section with 6 3/8-in. Pick-Up Cone

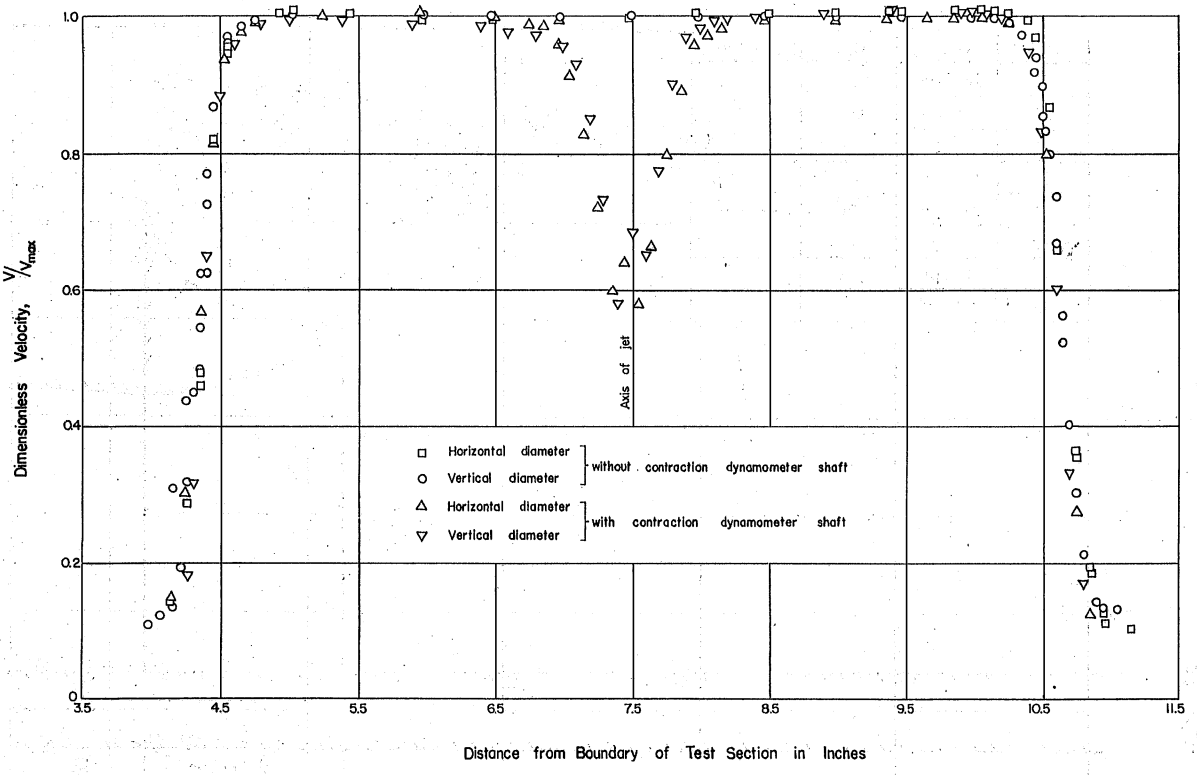

Fig. 31 - Velocity Distribution at Station 1 with and without the Contraction Dynamometer Shaft

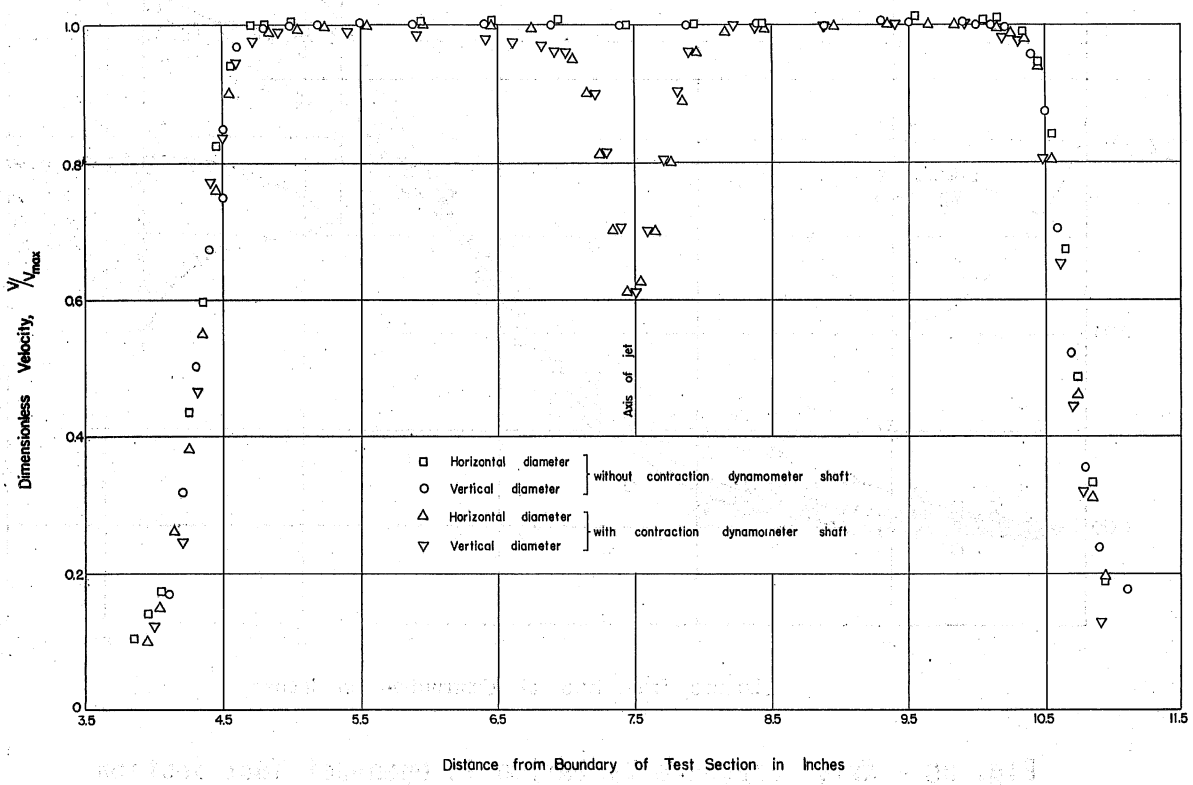

Fig. 32 - Velocity Distribution at Station 2 with and without the Contraction Dynamometer Shaft

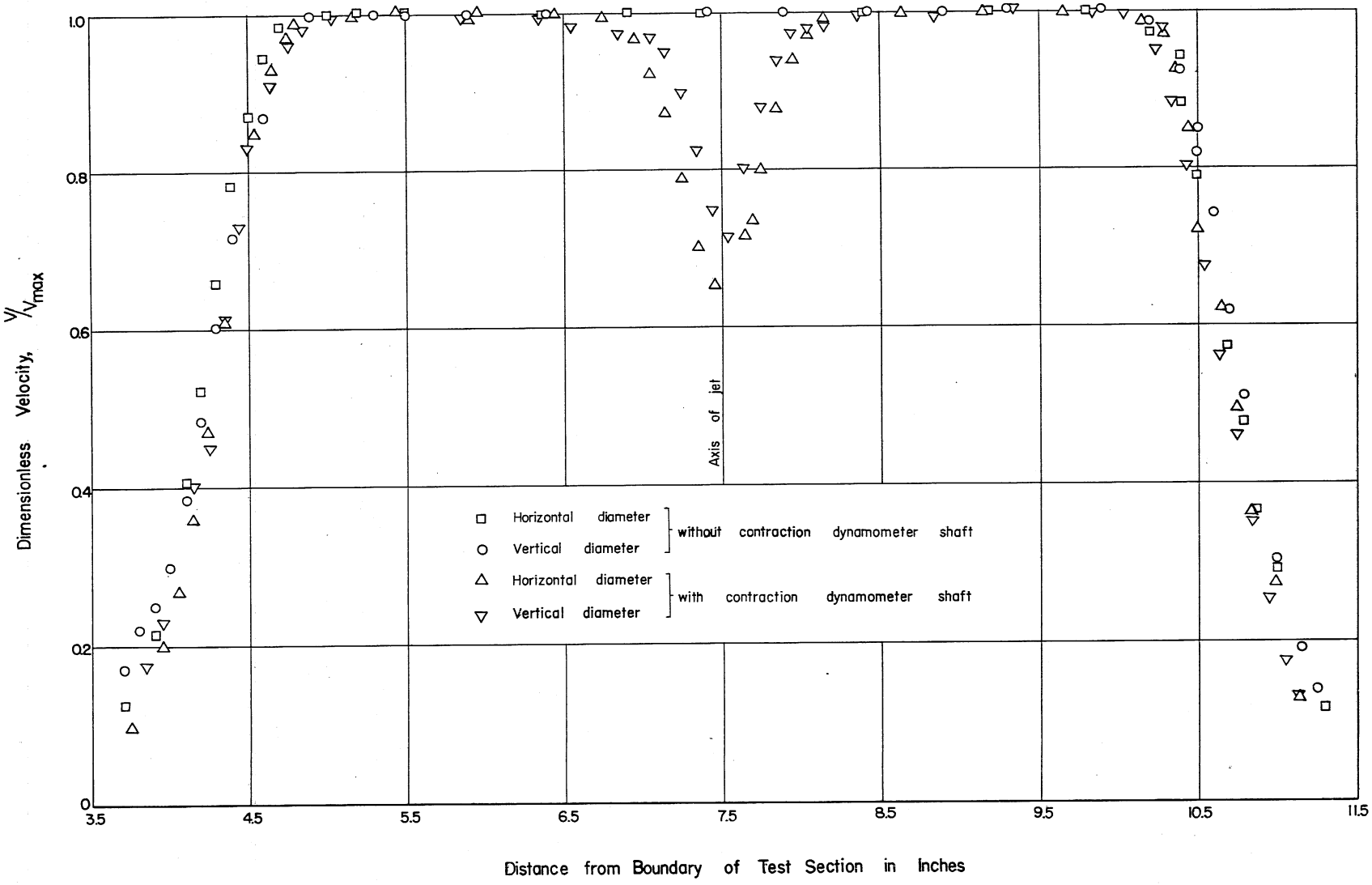

Fig. 33 - Velocity Distribution at Station 3 with and without the Contraction Dynamometer Shaft

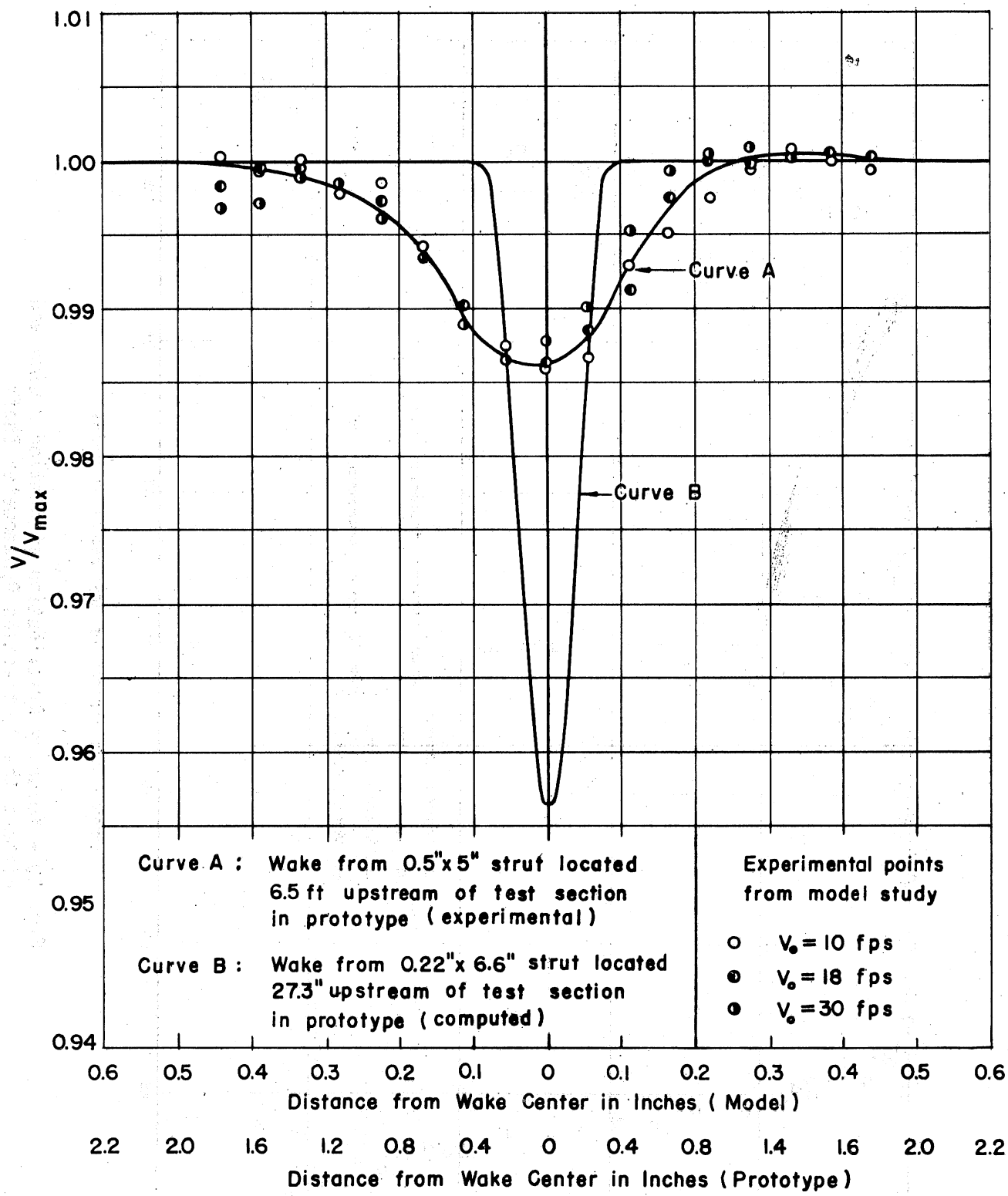

Fig. 34 - Velocity Distribution in Test Section in the Wake of Contraction Dynamometer Shaft Support Struts

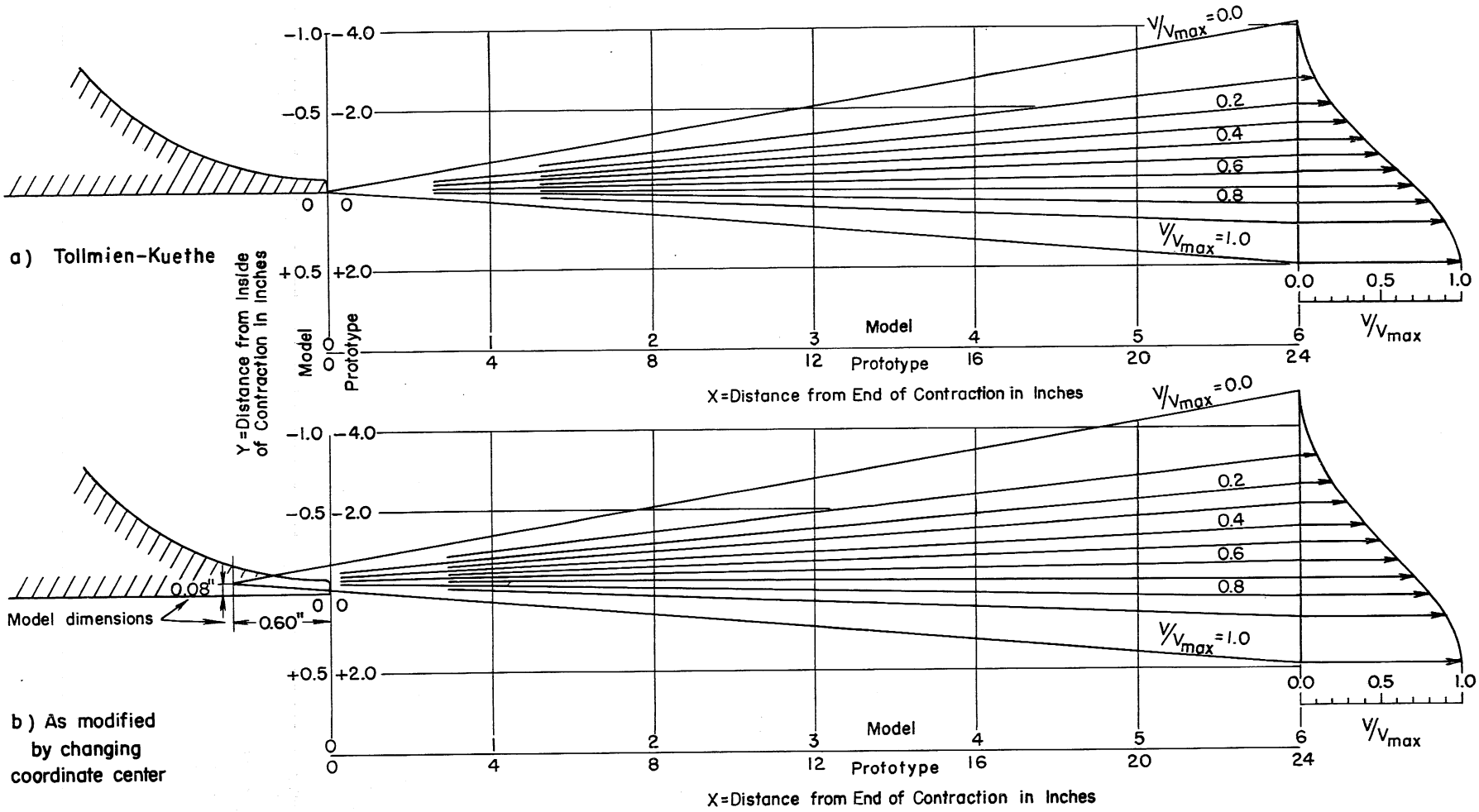

Fig. 35 - Theoretical Distribution of Longitudinal Velocities in Diffusion Region of Open-Jet Test Section

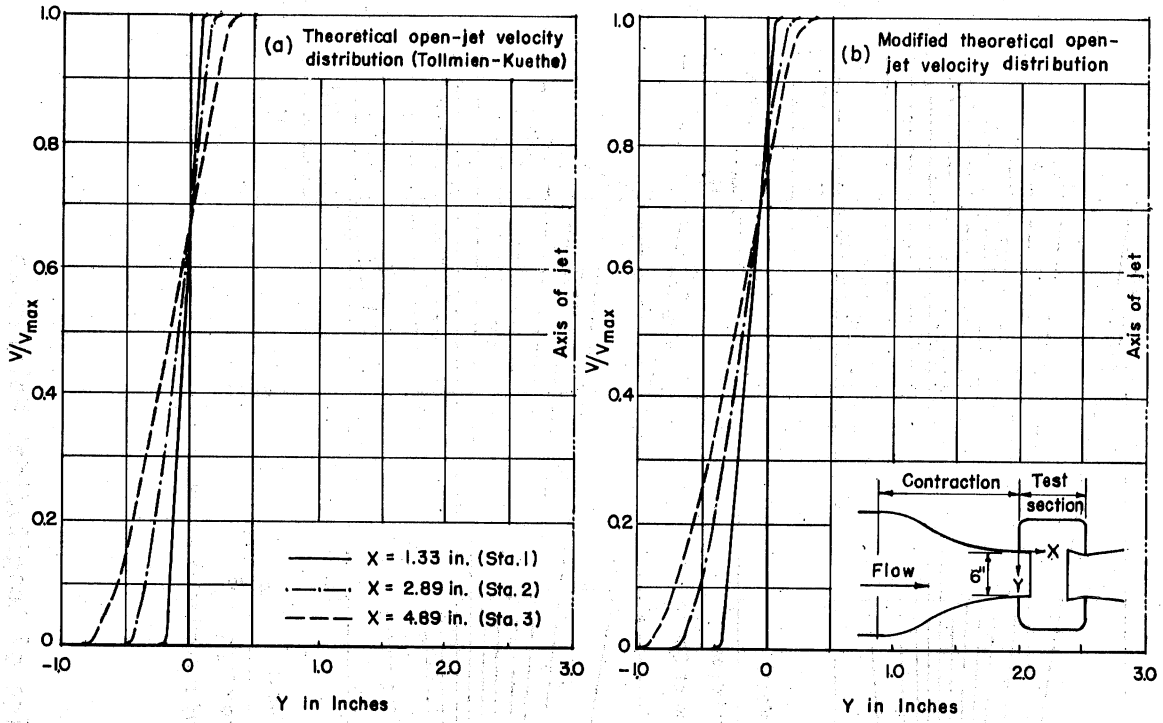

Fig. 36 - Theoretical Velocity Distributions at Traverse Stations in Model Open-Jet Test Section

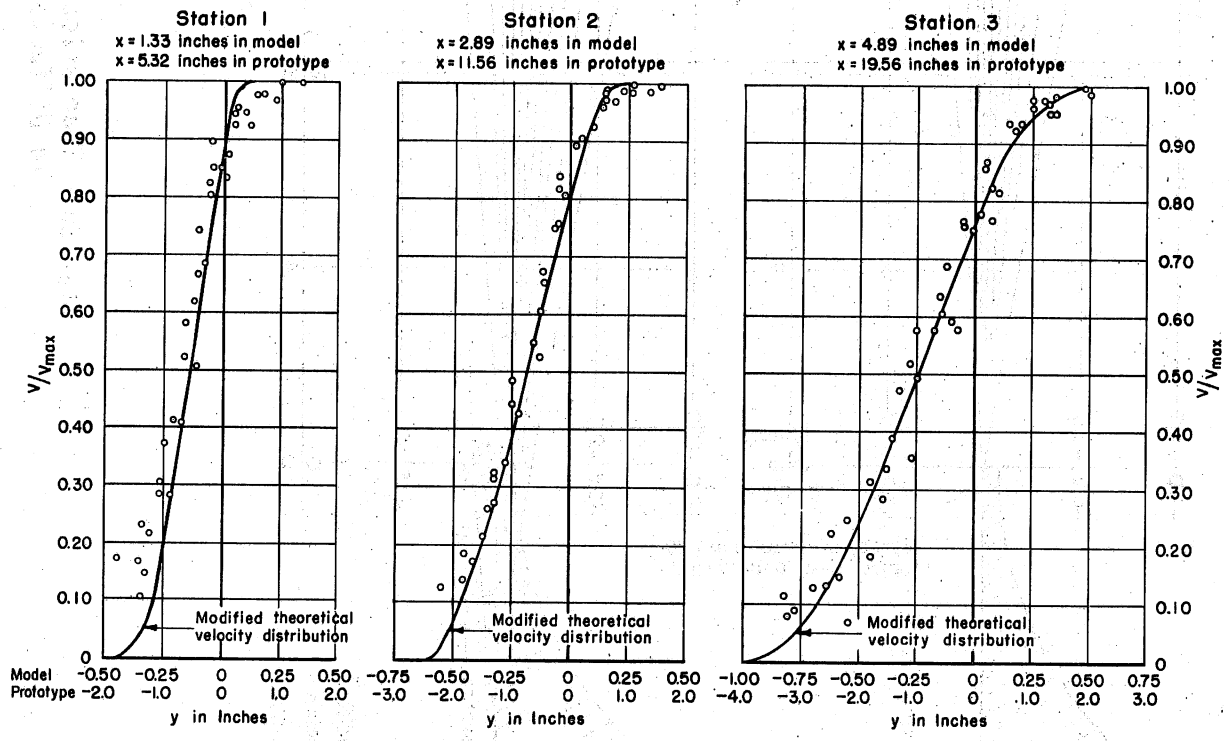

Fig. 37 - Measured Velocity Distribution in Diffusion Region of Model Open-Jet Test Section

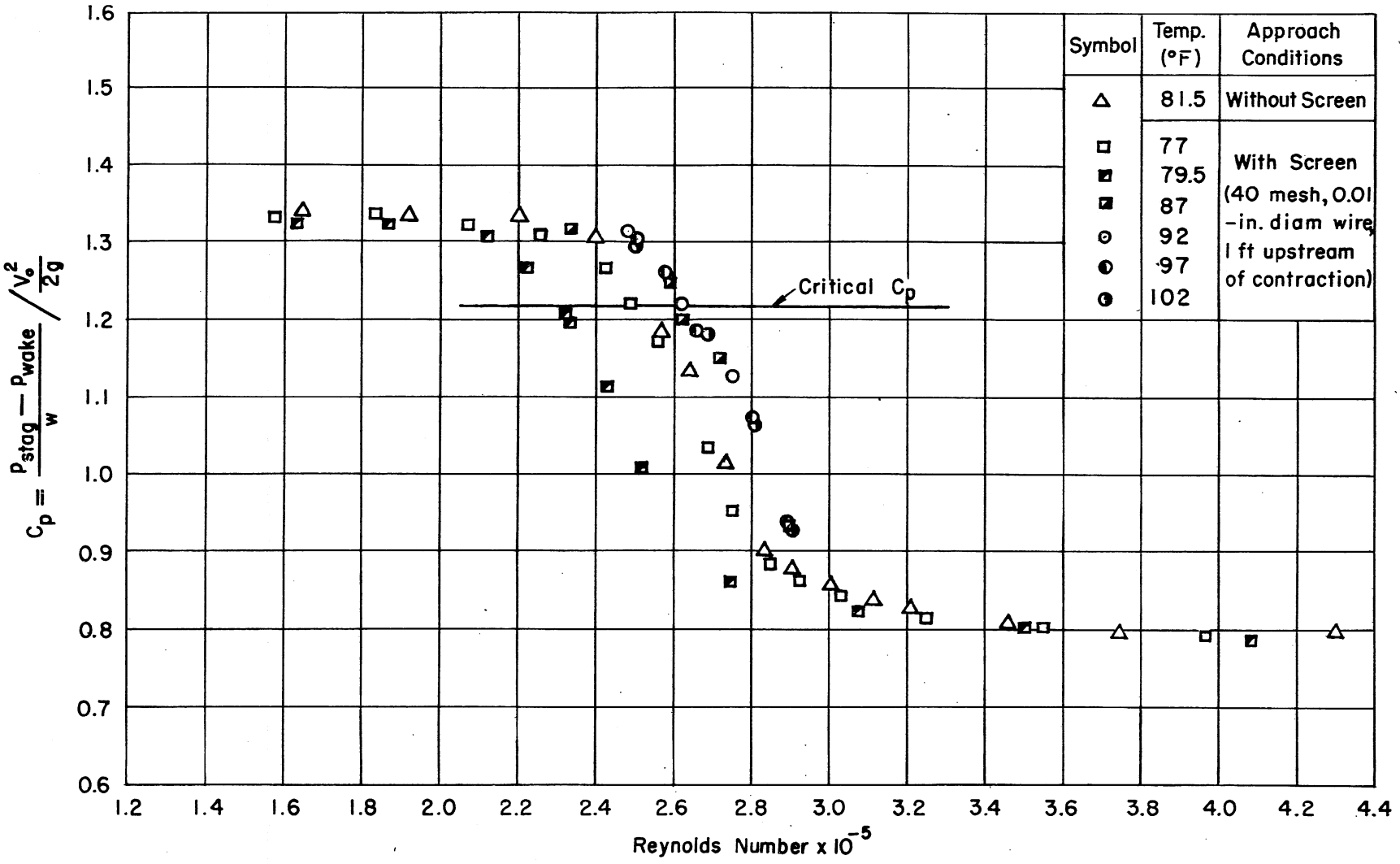

Fig. 38 - Critical Reynolds Number in Model Open-Jet Test Section as Determined by Turbulence Sphere

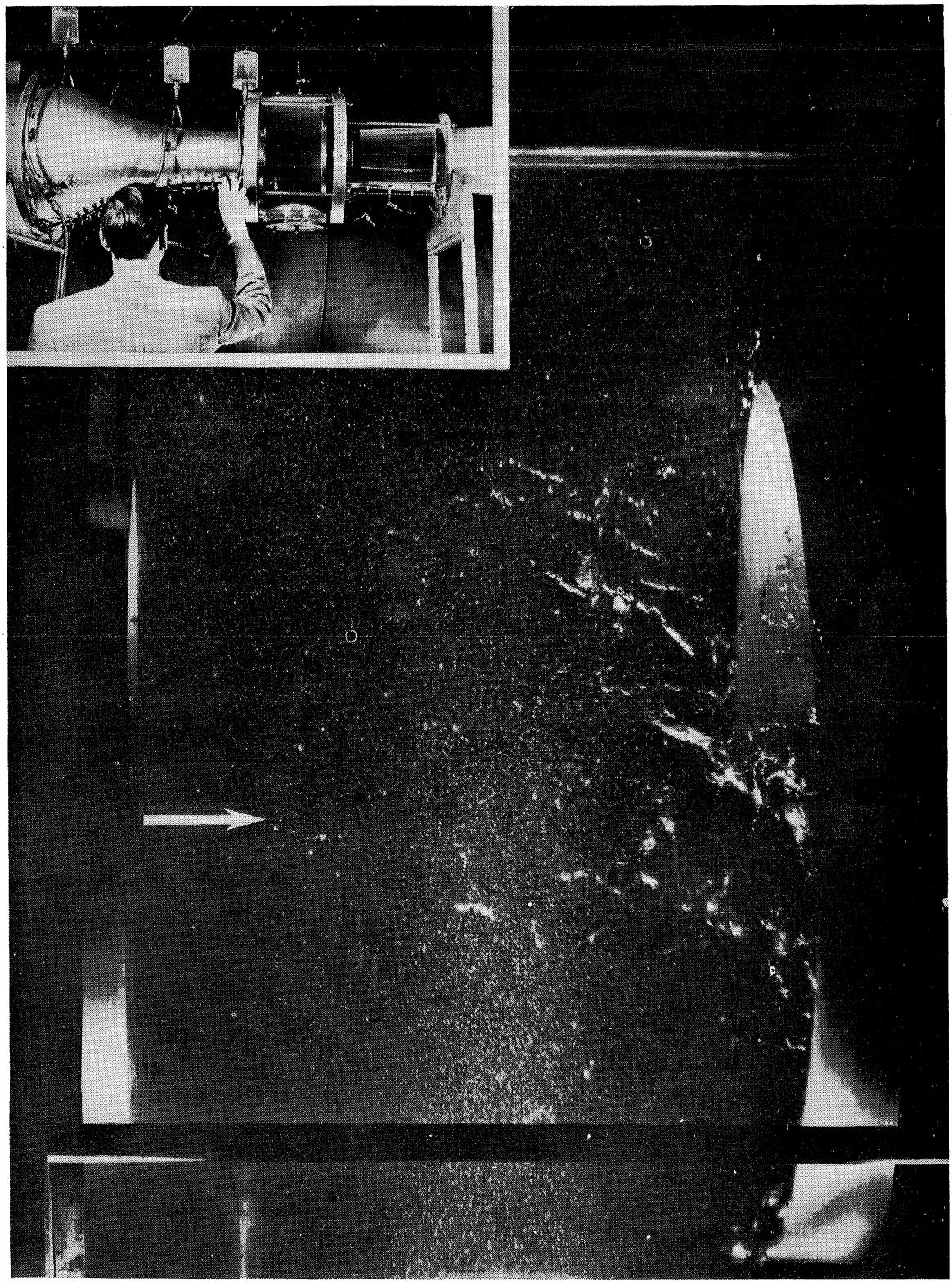

Fig. 39 - Severe Cavitation in the Diffusion Layer of the Model Open-Jet Test Section

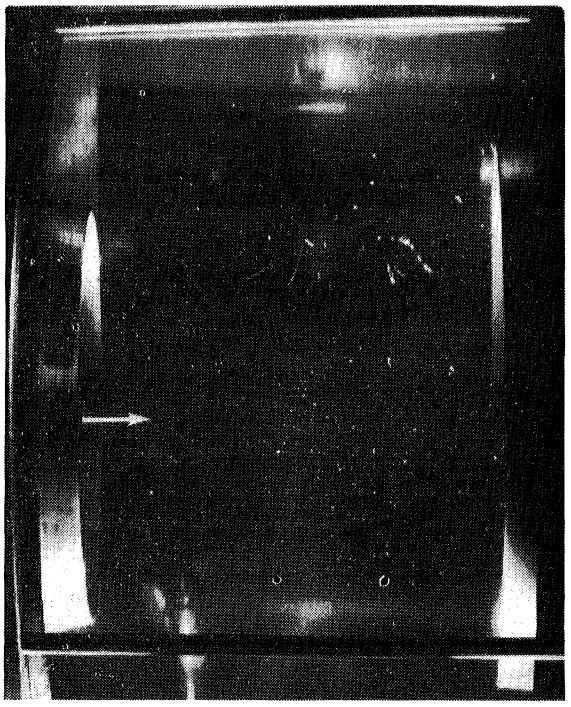

σ = 0.410

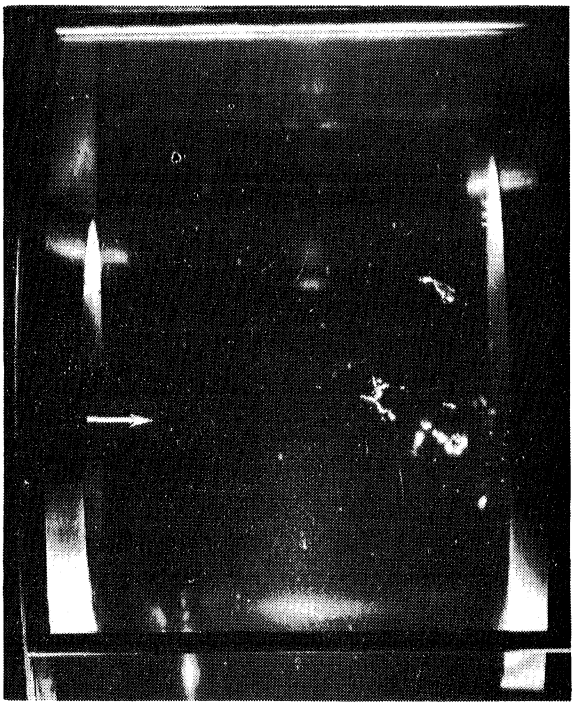

σ = 0.375

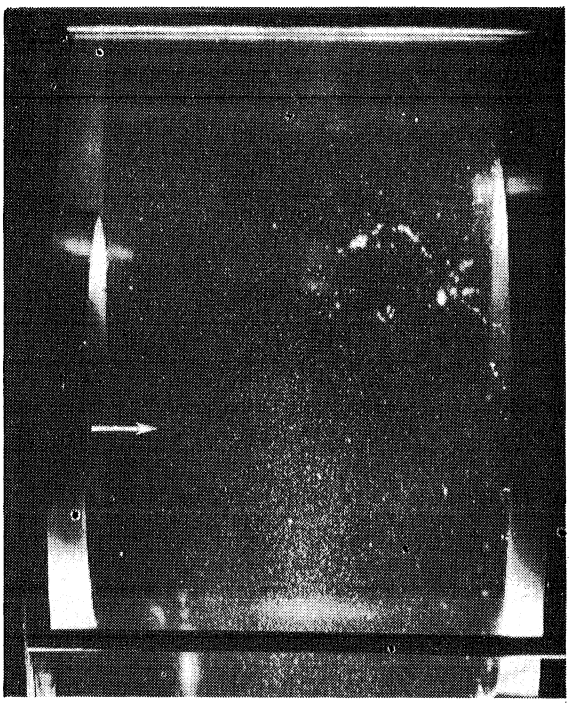

σ = 0.320

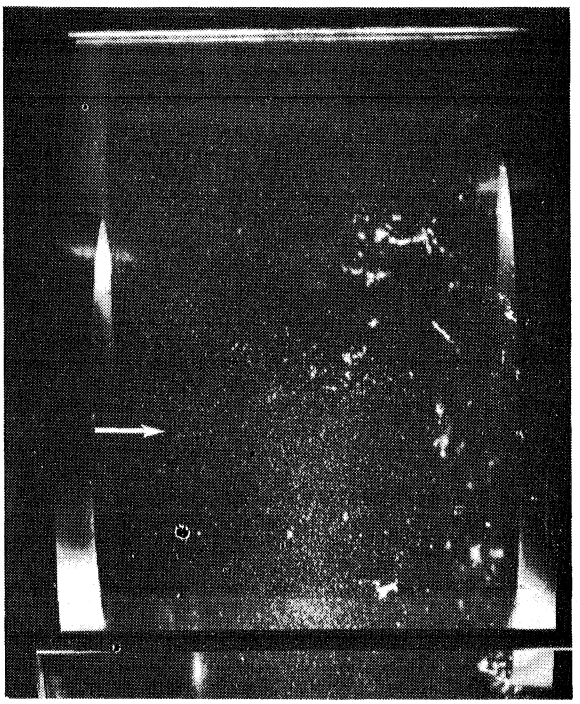

σ = 0.285

Fig. 40 - High-Speed Photographs of Cavitation in the Diffusion Layer of the Open-Jet Test Section at Different Cavitation Indices (σ)

PART IV. CLOSED-JET TEST SECTION AND CAVITATION INDEX

A. Introduction

The prototype water tunnel was designed in such a manner that an alternate closed-jet test section sleeve could be substituted for the open-jet test section in order to increase the usefulness of the tunnel for certain types of research. The closed-jet test section will permit operations at lower cavitation indices and at higher speeds than are possible in the open-jet test section, and thus will increase the scope of cavitation tests that can be made on stationary bodies.

Lower cavitation indices in the closed-jet test section, as compared to those obtainable in the open-jet test section, are made possible because no zone of free-turbulent mixing with its accompanying high turbulence is present in the closed jet. Also, the head loss in the closed-jet test section and main diffuser will be much smaller than in the open-jet test section and main diffuser; lower head loss permits higher speeds of operation for the same power installation. The turbulent boundary layer which builds up along the boundary of the closed-jet test section will grow less rapidly than the turbulent mixing region surrounding the open jet, and the test stream will have a uniform velocity distribution over a greater area in the closed-jet test section. For testing model propellers, however, all of these advantages in operation are offset by the size limitation imposed on the propeller to eliminate serious influences of the closed boundaries.

B. Theoretical and Experimental Pressure and Velocity Distribution in the Closed-Jet Test Section and Diffuser Transition

It is necessary to provide a smooth transition curve between a cylindrical test section and conical diffuser in order to avoid a discontinuity in direction in the tunnel boundary at the junction of these two components. The transition curve used in the model tunnel was a parabola in longitudinal section, which is one of the simplest curves that could be used; the transition was designed to be one test section radius long. This transition curve is an important factor in determining the minimum cavitation index available in the test section, and to some extent it influences the distribution of velocity in the test section. Because the transition curve plays an important role, and in one sense, a limiting role, in the operation of the closed-jet tunnel, added emphasis was placed on the investigation of this section of the tunnel.

A thorough theoretical investigation was especially desirable in order to explain the experimental results and to provide a basis for extrapolation to prototype dimensions since the experimental results were subject to error for several reasons. First, it was impossible to machine the transition curve to the exact desired dimensions. The equation of the curve in the model was

$$r = 3.0 + 0.009707x^2$$

where r is the radius of the transition in inches, and

x is the distance downstream from the beginning of the transition in inches.

This equation and the measured radii of the machined transition are shown in Fig. 15; the average measured error in machining the transition was ± 0.001 inch. The possible error in measuring the machined radius was ± 0.001 in., indicating that the probable maximum deviation of the model transition from the designed radius was ± 0.002 inch. Second, and perhaps of more importance, it is highly probable that piezometer taps in the test section and diffuser transition give a slightly erroneous indication of the wall pressure. Taps in this section of the tunnel are especially subject to the influence of dynamic effects of the stream since the boundary layer is thin and the wall velocity correspondingly high. Third, the upstream influence of the transition might cause appreciable errors in interpreting experimental measurements made at the downstream end of the test section.

The prototype tunnel will have a closed-jet test section 20.24 in. long (0.844 diam), which is 0.387 diam longer than the test section which was actually tested in the model. This increase in length of the closed-jet test section is made possible by adoption of the smaller pick-up cone for the open-jet test section. Experiments were not made with the longer test section because it was possible to take into account this change in length in applying the analytical method.

From previous experimental work [4], it was apparent that the wall pressure in the upstream end of the transition would be lower than the wall pressure in the downstream end of the test section. Application of Bernoulli's equation to the mean axial velocity indicates that the pressure should be higher in the transition than in the test section. However, a local reduction

in pressure at the boundary is brought about by the convex longitudinal curvature of the boundary in the transition, and this pressure reduction is further intensified by a continuing drop in pressure caused by the formation of a boundary layer in the test section and transition. The analytical method of attack in determining the pressure distribution was to superpose two pressure distributions, one being the pressure distribution of an ideal (frictionless) fluid and the other the pressure distribution due to formation of a boundary layer in the conduit.

The velocity and pressure distribution for an ideal fluid were determined by the relaxation method. The process of applying this method is explained in the appendix to this report. Only the results of the computations and the significance of these results will be discussed in this part of the report. The velocity distribution resulting from the analysis is shown in Figs. 41 and 42 and the wall pressure distribution is shown as the long-dashed line in Fig. 43.

The pressure distribution due to the boundary-layer formation, also shown in Fig. 43, was computed using formulas obtained for friction drag on flat plates parallel to the stream. The validity of applying this method had been verified for even longer test sections in a previous model study [4].

Writing the equation for power loss in a closed cylindrical conduit,

$$\int_{A_1} p_1 V_1 dA_1 + \int_{A_1} \frac{w\bar{V}_1^3 dA_1}{2g} - \int_{A_2} p_2 V_2 dA_2 - \int_{A_2} \frac{w\bar{V}_2^3 dA_2}{2g} = P_e \qquad (1)$$

where P_e equals the lost power. Substituting

$$\alpha = \frac{\int_A V^3 dA}{A\bar{V}^3}$$

and assuming that the pressure is constant in a cross section, one obtains, since $A_1 = A_2$,

$$C_p + (\alpha_1 - \alpha_2) = \frac{P_e}{\frac{A_1 w \bar{V}_1^3}{2g}} \qquad (2)$$

where C_p is the conventional pressure coefficient

$$C_p = \frac{\frac{p_1 - p_2}{w}}{\frac{\bar{V}_1^2}{2g}}$$

It will now be assumed that the power loss in the conduit is the same as the power loss on one side of a flat plate having a length equal to the length of the conduit under consideration and having an area equal to the wetted area of the conduit. If the conduit is circular and has a diameter d_1 and length $\underline{x}$, the power loss on one side of a flat plate $\underline{x}$ in. long and πd_1 in. deep when held in a uniform stream of velocity $\bar{V}_1$ would be

$$P_e = \pi d_1 C_d x w \frac{\bar{V}_1^3}{2g} \tag{3}$$

where C_d is the average coefficient of drag on the flat plate.

The Prandtl formula for the mean coefficient of skin drag on a flat plate held parallel to the flow is

$$C_d = \frac{0.074}{Re_x^{1/5}} \tag{4}$$

This formula is supposedly valid for turbulent boundary layers up to $Re_x = 20{,}000{,}000$, or in the region in which the seventh-root law of velocity distribution applies. This Reynolds number will not be exceeded in the operation of the prototype.

Substituting Eq. (3) in Eq. (2) gives

$$C_p = (a_2 - a_1) + 4C_d \left(\frac{x}{d}\right) \tag{5}$$

The average skin-drag coefficient C_d can be determined from Eq. (4) if it is assumed that the boundary layer begins to develop as a turbulent boundary layer in the conduit from the point from which $\underline{x}$ is measured. The reference point for the experimental measurements in Fig. 43 was the pressure manifold which was in the contraction and $1\frac{1}{2}$ in. upstream of the beginning of the test section. Since the diameter of the contraction was 6.000 in. at this

point and since the surface was the same (smooth, machined aluminum) as the test section, the portion of the contraction cone downstream of the reference manifold was considered as part of the test section. The head loss coefficients for the closed-jet test section thus include the loss in the 1 1/2 in. of the model contraction, which was not taken into account in computing the head loss in the contraction, and the 2.76-in. length of cylindrical test section shown in Fig. 5, a total of 4.26 inches.

Assuming that $\alpha_1 = 1.0000$ at the reference manifold and using $\alpha_2 = 1.0037$, as determined from the velocity traverses shown in Fig. 45, then

$$C_p = 0.0037 + \frac{4 \cdot 4.26}{6} \cdot \frac{0.074}{\left(\frac{V_o \cdot 4.26 \cdot 10^5}{0.908 \cdot 12} \right)^{1/5}} \qquad (6)$$

at the downstream end of the test section. (In Eq. (6), the kinematic viscosity is taken as $0.908 \cdot 10^{-5}$ corresponding to a water temperature of 82° F.)

Two values of this coefficient are joined by straight lines to the origin in Fig. 43, since previous experiments had shown that the pressure drop due to this boundary-layer formation is practically linear[4]. These straight lines are extended as dotted lines into the diffuser transition to indicate the approximate pressure drop in the transition attributable to wall drag and change of α.

The curves labeled "Predicted Pressure Distribution" in Fig. 43 are obtained by adding the pressure distribution for the ideal fluid flow to the pressure distribution resulting from the boundary-layer growth. Some error is undoubtedly involved in superposing the two results. A more exact method of computing the boundary pressure distribution would be to compute the displacement thickness of the boundary layer, decrease the conduit radius by the displacement thickness, and compute the pressure distribution of an ideal fluid on this fictitious boundary. This method could not be used in the present case because the displacement thickness in the contraction throat could not be determined and because no proved method is available for computing changes in displacement thickness in smooth, closed conduits.

The experimentally measured wall pressure distribution is shown in Fig. 43. The average pressure difference between the reference manifold and

each of two diametrically opposed taps was divided by the head of the mean test section velocity to give the pressure coefficients

$$C_p = \frac{\frac{p - p_{ref}}{w}}{\frac{V_o^2}{2g}} \tag{7}$$

which are plotted in Fig. 43. The agreement between theory and experiment is reasonably satisfactory.

The most important difference between the theoretical and actual pressure distribution shown in Fig. 43 occurs at Tap A, which is at the downstream end of the test section. The experimentally measured pressure is $0.01\ V_o^2/2g$ higher than the calculated value. If it is assumed that the pressure drop due to boundary-layer formation has been computed correctly, the experiment indicates that wall curvature caused no pressure reduction upstream of the transition. However, the influence of the transition must extend along the wall for some distance upstream if fluid accelerations are to occur gradually as the beginning of curvature is approached, and the above hypothesis is not tenable.

A second hypothesis to explain the difference between theory and experiment is that the pressure drop caused by the boundary-layer formation has been computed incorrectly. Aside from the assumptions made in applying the theory of two-dimensional flow, there remain the objections that the boundary layer does not have zero thickness at the reference manifold and that there may be a transition from laminar to turbulent flow in the boundary layer. There seems to be little justification for assuming that the boundary layer is laminar near the reference manifold, since the boundary layer is actually a continuation of the contraction boundary layer which was undoubtedly turbulent, and it does not seem likely that a transition from turbulent to laminar flow would occur. If it is admitted that the boundary layer has appreciable thickness at the reference manifold, the pressure drop caused by boundary-layer development would be reduced, since a_1, which was assumed equal to unity in Eq. (5), would be increased and C_p would be decreased. This adjustment in a_1 would improve the agreement between theory and experiment for all except one of the taps in the diffuser transition; the adjustment was not

applied to the calculations because the boundary-layer thickness at the reference manifold could not be determined. However, a previous experiment with the same contraction but with a longer test section [4] indicated that the assumption of zero boundary-layer thickness at the reference manifold gives good agreement between Eq. (5) and the experimental pressure drop.

Another explanation for the difference between the predicted and measured pressure at Tap A is that the experimentally measured pressure does not actually represent the average wall pressure at this cross section. It is entirely possible that the piezometer taps, although carefully formed, gave readings that were as much as $0.01\ V_o^2/2g$ in error, since the wall velocity is high in this section of the tunnel circuit.

C. Closed-Jet Test Section Head Loss

Assuming that the two-dimensional boundary-layer theory has been legitimately applied to this problem, the energy loss coefficient for the section of the tunnel between the reference manifold and the downstream end of the test section is given by the second term on the right of Eq. (6)

$$K_f = 4 \cdot \frac{4.26}{6} \cdot \frac{0.074}{\left(\frac{V_o \cdot 4.26 \cdot 10^5}{0.908 \cdot 12}\right)^{1/5}} = 0.0253\ V_o^{-1/5}$$

(It appears that the wall pressure measured at Tap A is the wall pressure which would exist in the absence of a transition downstream of the test section; that is, the measured pressure at Tap A is very close to the average cross-sectional pressure. This is fortunate because the head loss coefficient for the diffuser following the closed-jet test section was determined by measuring the pressure difference between Tap A and the downstream end of the diffuser. If the measurement at Tap A had given the true wall pressure, a correction from wall pressure to average cross-sectional pressure would have had to be applied when computing the head loss in the diffuser.)

The friction loss coefficient (head loss at 76° F divided by test section velocity head) for the redesigned, untested, prototype closed-jet test section (a cylindrical section 20.24 in. long) and downstream 6 in. of the

prototype contraction can be computed from the equation

$$K_f = 4 \cdot \frac{26.24}{24} \cdot \frac{0.074}{\left(\frac{V_o \cdot 26.24 \cdot 10^5}{12}\right)^{1/5}} = 0.0277\ V_o^{-1/5}$$

The values so determined are $K_f = 0.0155$ at $V_o = 18$ fps, 0.0140 at 30 fps, 0.0127 at 50 fps, and 0.0118 at 70 fps. It is estimated that the value of α at the downstream end of the prototype closed-jet test section will be about 1.0045. The coefficient C_p of Eq. (5), which is approximately the pressure coefficient of the core flow, will vary between -0.0200 and -0.0173 for normal testing speeds.

D. Velocity Distribution and Boundary-Layer Thickness

The velocity traverses which were made at the downstream end of the test section (2.76 in. from the end of the contraction) are plotted dimensionlessly in Fig. 44. It will be noted that the velocity is very uniform over the central area of flow; the variation present is about 1/3 of 1 per cent of the maximum velocity. Only in the boundary layer does the velocity fall below 99 per cent of the velocity on the axis of the test section.

Boundary-layer thickness is important inasmuch as it determines the cross-sectional area of the test stream which can be used for testing purposes. The growth of the boundary layer and consequent retardation of a portion of the test stream forces the central core of the flow to increase in velocity in order to maintain continuity of discharge. Associated with this redistribution of velocity are an increase in the total kinetic energy of the stream and a reduction in pressure in order to maintain constant the total head of the core flow, which has no shear or energy dissipation.

As previously stated, the thickness of the boundary layer in the test section could probably be computed quite accurately if it had zero thickness at the entrance to the test section. However, the boundary layer is in the process of formation in the throat of the contraction, and this greatly complicates any theoretical attack of the problem. Also, the longitudinal decrease in pressure and the three-dimensional character of the flow necessitate making additional changes in applying the well-developed theory of two-dimensional boundary layers. Fortunately, velocity distributions formerly

determined in a 36-in. long test section following the same contraction [4], together with the experimental work done in this study, permit interpolation to determine the boundary-layer thickness in the redesigned, longer closed-jet test section of the prototype.

Defining the boundary-layer thickness as the distance from the wall where the velocity is 99 per cent of the maximum velocity, the average boundary-layer thickness from Fig. 44 is 0.29 in., 2.76 in. from the end of the contraction. From reference [4] the boundary-layer thickness 1/2 in. from the end of the contraction is 0.18 in. and it is 0.90 in., 36 1/2 in. from the end of the contraction. The boundary-layer thickness is increasing faster in the upstream end of the test section than in the downstream end. Interpolating among these values shows that the boundary-layer thickness would have been about 0.35 in. at the end of the test section had it been 5.06 in. long, corresponding to the length of the redesigned closed-jet test section. Theory indicates that the boundary layer should be relatively thinner at higher Reynolds numbers, but the model tests were not conclusive in this respect due to small inaccuracies in measuring distance from the wall of the test section. According to the theory of Prandtl, for Re_x less than $2 \cdot 10^7$,

$$\frac{\delta}{x} = \frac{0.377}{Re_x^{1/5}}$$

where δ is the boundary-layer thickness,

x is the distance along the flow direction from the point where the boundary layer begins to form, and

Re_x is equal to Vx/ν .

If ℓ_r is the scale ratio between prototype and model (in this study $\ell_r = 4$) for equal mean velocities of flow and equal kinematic viscosities, dimensional analysis will show that

$$\frac{\delta_p}{\delta_m} = \ell_r^{4/5} = 4^{4/5} = 3.12$$

In this formula δ_p is the boundary-layer thickness in the prototype and δ_m is the boundary-layer thickness in the model. The average boundary-layer thickness at the downstream end of the redesigned prototype test section will therefore be $0.36 \cdot 3.12 = 1.12$ inches.

In contrast to the flow in the open-jet test section, there will be an increase in the velocity of the central core of the test stream as it passes

through the closed-jet test section. At the end of the model closed-jet test section, the centerline velocity was 1.0146 V_o, where V_o is the average velocity of flow in the closed-jet test section. Assuming that no energy is lost in the central core*, the velocity of the central core at any cross section of the test section can be computed if the longitudinal pressure distribution is known. The average pressure head drop between the reference manifold 1 1/2 in. upstream of the contraction and the downstream end of the test section was 0.0169 $V_o^2/2g$ ft. If it is accepted that the measured wall pressure represents the average pressure of the core flow, application of Bernoulli's theorem will show that the velocity of the core at the reference manifold (V_c) is

$$V_c = V_o\sqrt{(1.0146)^2 - 0.0169} = 1.0061\ V_o$$

It has been shown that the difference in mean core pressure head between a point in the prototype tunnel corresponding to the reference manifold and the downstream end of the redesigned test section will be about 0.0200 $V_o^2/2g$ ft. Assuming that the same velocity distribution occurs in the model and prototype contraction, the velocity of the central core at the downstream end of the closed-jet test section (V_{max}) will be

$$V_{max} = V_o\sqrt{(1.0061)^2 + 0.0200} = 1.0160\ V_o$$

Figures 41 and 42, which show the velocity distribution for an ideal fluid as determined by the relaxation method, are of interest at this point because they indicate that the velocity in the core was probably not uniform, even though the velocity distribution measured with the Pitot cylinder (Fig. 44) showed very little variation. The curve $\xi = 0$ of Fig. 41 shows that there should be an approximate 1 per cent variation in velocity (and 2 per cent variation in pressure) in the cross section at the end of the test section. However, the Pitot cylinder measured only the total head at a point, and thus was incapable of recording a variation in velocity when the pressure varied in such a manner that the total head was constant. Figure 41 indicates that

*That the total head in the central core is actually constant can be confirmed by analyzing the data in reference [4]. The increase in core velocity head in 36 in. of the cylindrical test section (6 diam) of the model of the 60-in. prototype tunnel was 0.0825 $V_o^2/2g$, and the average drop in pressure was 0.0830 $V_o^2/2g$.

the radial variations in longitudinal velocity are very small in the upstream portion of the test section; the indicated velocity variation at the midpoint of the test section is approximately 0.25 per cent. The radial velocities in the test section which are set up by the diffuser transition are very small, as can be seen from the curve $\xi = 0$ in Fig. 42. Consequently, the transition does not appreciably affect the parallelism of the stream lines in the test section.

E. Critical Cavitation Index

If the cavitation index in the test section is lowered sufficiently, cavitation will begin at some point on the tunnel structure. The noise, vibration, and flow instabilities resulting from this cavitation can seriously affect the test procedures, and tests cannot ordinarily proceed to lower cavitation indices in the test section. If the vaned elbows and pump have been satisfactorily designed, and if the contraction has a monotonically decreasing pressure, the diffuser transition will be the point of initial cavitation in a closed-jet water tunnel. The shape of the diffuser transition thus imposes an important limit on the range of operation, and it is of importance to know whether the parabolic transition is an adequate design or whether significant improvement could be made by using a different transition curve.

The critical cavitation index is defined as the local cavitation index in the test section when cavitation is incipient in the diffuser transition. The critical index can be expressed as

$$\sigma_{cr} = \frac{\frac{p_{cr} - p_{vp}}{w}}{\frac{V_o^2}{2g}} \tag{8}$$

where p_{cr} is the absolute static pressure at any point in the test section when cavitation is incipient in the transition,

p_{vp} is the vapor pressure of the fluid, and

V_o is the mean test section velocity.

This critical index will vary from point to point in the test section because of hydrostatic and longitudinal pressure variations, and the longitudinal pressure variations will be dependent on Reynolds number. However, all of

these factors can be taken into consideration and the critical cavitation index at any point in the test section can be computed with acceptable accuracy for any closed-jet design by using the methods outlined in section B of this part of the report.

If, for the present, interest is confined to the section of the tunnel corresponding to the reference manifold (1 1/2 in. upstream from the end of the contraction in the model), the critical pressure at a point in this section will be

$$\frac{p_{cr}}{w} = - C_{p_{min}} \cdot \frac{V_o^2}{2g} + \frac{p_{inc}}{w} + Z \tag{9}$$

where $C_{p_{min}}$ is the minimum coefficient of pressure defined by Eq. (7),

p_{inc} is the time mean of the absolute static pressure at the point where cavitation is incipient, and

Z is the elevation of the point of incipient cavitation above the point for which p_{cr} is being computed.

Substituting Eq. (9) in Eq. (8) gives

$$\sigma_{cr} = - C_{p_{min}} + \frac{\left(\frac{p_{inc} - p_{vp}}{w} + Z\right)}{\frac{V_o^2}{2g}} \tag{10}$$

All of the factors in this equation can be computed except the difference between the incipient pressure and the vapor pressure. This difference will depend on at least two factors: the amount of dissolved gases in the water and the intensity of time variations of pressure at the point of incipient cavitation. The influence of dissolved gases on cavitation is the subject of considerable current research. However, this factor can be assumed to be of small importance for the present application if most of the dissolved gases are removed from a water tunnel before cavitation tests are begun. The unsteady variations in pressure will probably be of some importance because the point of incipient cavitation is in the turbulent boundary layer at the top of the transition. Cavitation will begin at this point when the fluctuating pressure falls to vapor pressure for a sufficient length of time. It is

therefore feasible that cavitation will form even though the mean pressure is higher than the vapor pressure. The dependency of the pressure fluctuation on the turbulent velocity components is shown in Eq. (1) of Part III. This equation cannot be used directly for purposes of computation, but the effective influence of the pressure fluctuations can be determined from the model tests.

Cavitation tests were made on the model tunnel after subjecting the tunnel to a very low pressure for a sufficient amount of time so that no more dissolved gases could be withdrawn from the water. The tunnel was then set at a certain pressure and the velocity was increased until cavitation could be heard; the absolute pressure at the reference manifold was determined at this time. The average critical cavitation index was 0.0565 at the top of the tunnel at the reference manifold for test section velocities between 40 and 50 fps; that is, the critical absolute static pressure at this point was

$$\frac{p_{cr}}{w} = 0.0565 \frac{V_o^2}{2g} + \frac{p_{vp}}{w}$$

The experimental minimum pressure coefficient was -0.0400. Substituting these values in Eq. (9) shows that

$$\frac{\frac{p_{inc} - p_{vp}}{w}}{\frac{V_o^2}{2g}} = 0.0165 \qquad (11)$$

This result assumes that Tap B (Fig. 43) was at the section of minimum pressure and was recording the correct pressure; both assumptions are apparently correct in view of the comparison of theory and experiment in Fig. 43.

The diffuser transition in the prototype will have a slightly sharper curvature than in the model because the prototype transition must become tangent to a line having a slope of 3° 30' instead of 3° 20', as in the model. However, the change in shape is so slight (Fig. 15) that there will be no important difference in the dimensionless wall pressure distribution for the ideal-fluid flow. The minimum pressure coefficient in the prototype, however, will not be the same as in the model because of the influence of Reynolds

number and because the test section of the prototype will be dimensionlessly longer. The difference in wall pressure between a section 6 in. upstream of the prototype test section and the section of minimum pressure in the transition will be

$$\frac{\frac{p_{min} - p_{ref}}{w}}{\frac{V_o^2}{2g}} = C_{p_{min}} = -0.0166 - (0.0045 + 0.0277\, V_o^{-1/5})\,\frac{28.64}{26.24} \qquad (12)$$

The first term on the right-hand side of Eq. (12) is the pressure difference with an ideal fluid (Fig. 43) and the second term is the pressure difference due to boundary-layer formation [Eq. (5)]. Substitution of Eqs. (11) and (12) in Eq. (10) gives

$$\sigma_{cr} = 0.0166 + (0.0045 + 0.0277\, V_o^{-1/5})\,\frac{28.64}{26.24} + 0.0165 + \frac{Z}{\frac{V_o^2}{2g}}$$

as the function defining the critical cavitation index 6 in. upstream from the beginning of the test section in the prototype. Since the pressure drop in the test section is approximately linear, the critical cavitation index at any point ℓ in. downstream from the section, 6 in. upstream of the test section, and $\underline{Z}$ ft below the crown of the test section will be given by the formula

$$\sigma_{cr} = 0.0166 + (0.0045 + 0.0277\, V_o^{-1/5})\,\frac{28.24 - \ell}{26.24} + 0.0165 + \frac{Z}{\frac{V_o^2}{2g}} \qquad (13)$$

This formula is plotted in Fig. 45 for two values of $\underline{Z}$ and three values of V_o.

The extent to which the diffuser transition influences the critical cavitation index at any point can be seen by reference to Fig. 45 or Eq. (13). The term 0.0166 is the only factor which would be influenced by a change in the shape of the transition, and this term can never be reduced to zero. It could probably be reduced somewhat by increasing the length of the transition, but this would cause an increase in energy requirement and cost of construction of the tunnel. A transition of about the same length (1 radius long) but chosen to produce a more gradual change in area near the test section would

probably result in some improvement. The amount of improvement could be computed by performing the relaxation process on the chosen boundary; if a digital or analogue computer were available, the relaxation could probably be performed quite easily, as is indicated in the Appendix.

At any rate, the critical cavitation index for the present design is determined primarily by the dimensions of the test section so that the parabolic transition 1 radius long is an adequate, though probably not optimum, design. If it is desired to attain lower cavitation indices, a change in the design dimensions of the test section would be of more value than a change in the dimensions of the transitions. If the test section flared outward slightly in the direction of flow, the pressure drop caused by the boundary-layer formation could be nullified, and there would be a very significant decrease in the critical cavitation index. The test section could be designed so that the pressure, and therefore the critical cavitation index, were constant in the direction of flow for one particular Reynolds number. Slight pressure gradients would exist if the Reynolds number were different from the design Reynolds number, but these pressure gradients would in no case be as large as those that would exist in a cylindrical test section.

The foregoing analysis of the cavitation characteristics of the closed-jet test section is strictly valid only if the diameter of the test body, or the diameter of the steady-state cavitation bubble formed by the body, is small compared to the diameter of the test stream. If the stream is forced to undergo an appreciable constriction in passing by the test body, local accelerations will take place which could cause cavitation at the crown of the test section in the plane of maximum diameter of the cavitation bubble before cavitation begins at the diffuser transition. If the bubble diameter is known, the magnitude of this influence can be computed by application of Bernoulli's equation, since the total head is constant in the core. The drag of the test installation will also cause a pressure drop between the upstream and downstream end of the test section in excess of that caused by boundary-layer formation, which would also raise the critical cavitation index of the tunnel.

F. Conclusions

On the basis of these experimental and analytical studies of the closed-jet test section, it is concluded that:

1. Radial variations in longitudinal velocity in the test stream will be less than 1 per cent, except in the boundary layer, which will have a thickness at the downstream end of the redesigned

test section of about 4.5 per cent of the diameter of the test section. There will be a 1.6 per cent increase in core velocity as the stream passes through the test section.

2. The head loss from a section in the contraction 6 in. upstream of the beginning of the prototype test section to the downstream end of the test section will vary from 0.0155 $V_o^2/2g$ at a test section velocity of 18 fps to a 0.0118 $V_o^2/2g$ at a test section velocity of 70 fps.

3. The critical cavitation index at the crown at the upstream end of the test section will be approximately 0.05. The critical index on the axis of the test section will be appreciably greater than this and will vary with the speed of testing.

4. No significant improvement can be made in the limiting cavitation characteristics by changing the design of the diffuser transition that was tested.

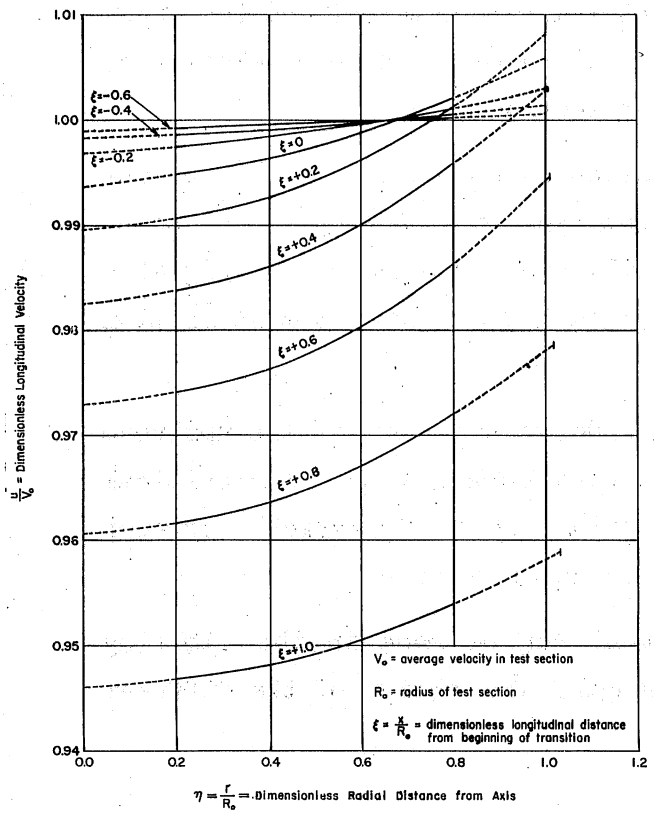

Fig. 41 - Theoretical Longitudinal Velocity Distribution in Closed-Jet Test Section and Diffuser Transition

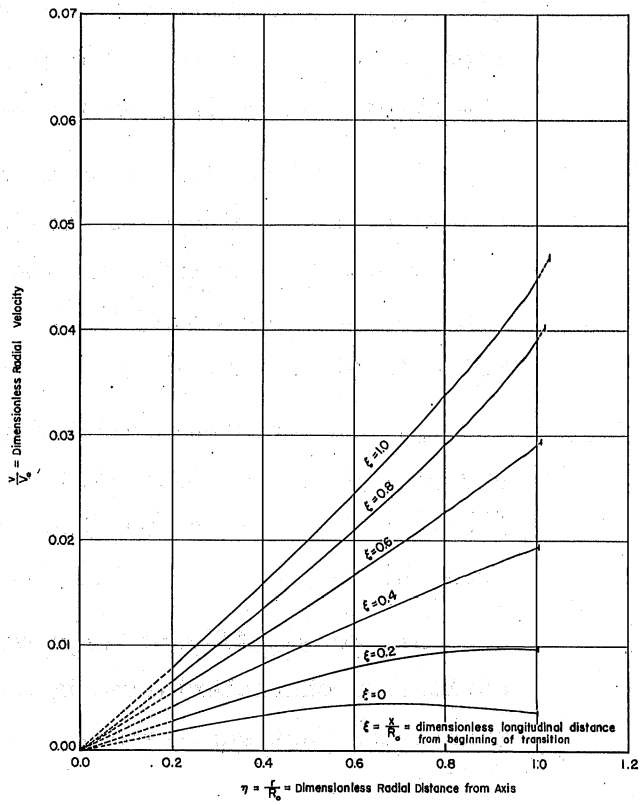

Fig. 42 - Theoretical Radial Velocity Distribution in Diffuser Transition

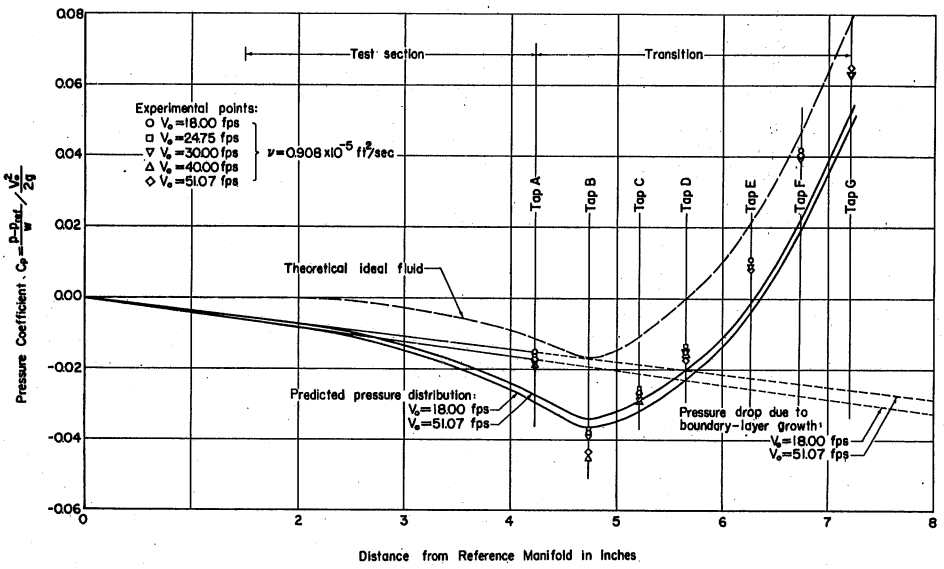

Fig. 43 - Boundary Pressure Distribution in Closed-Jet Test Section and Diffuser Transition

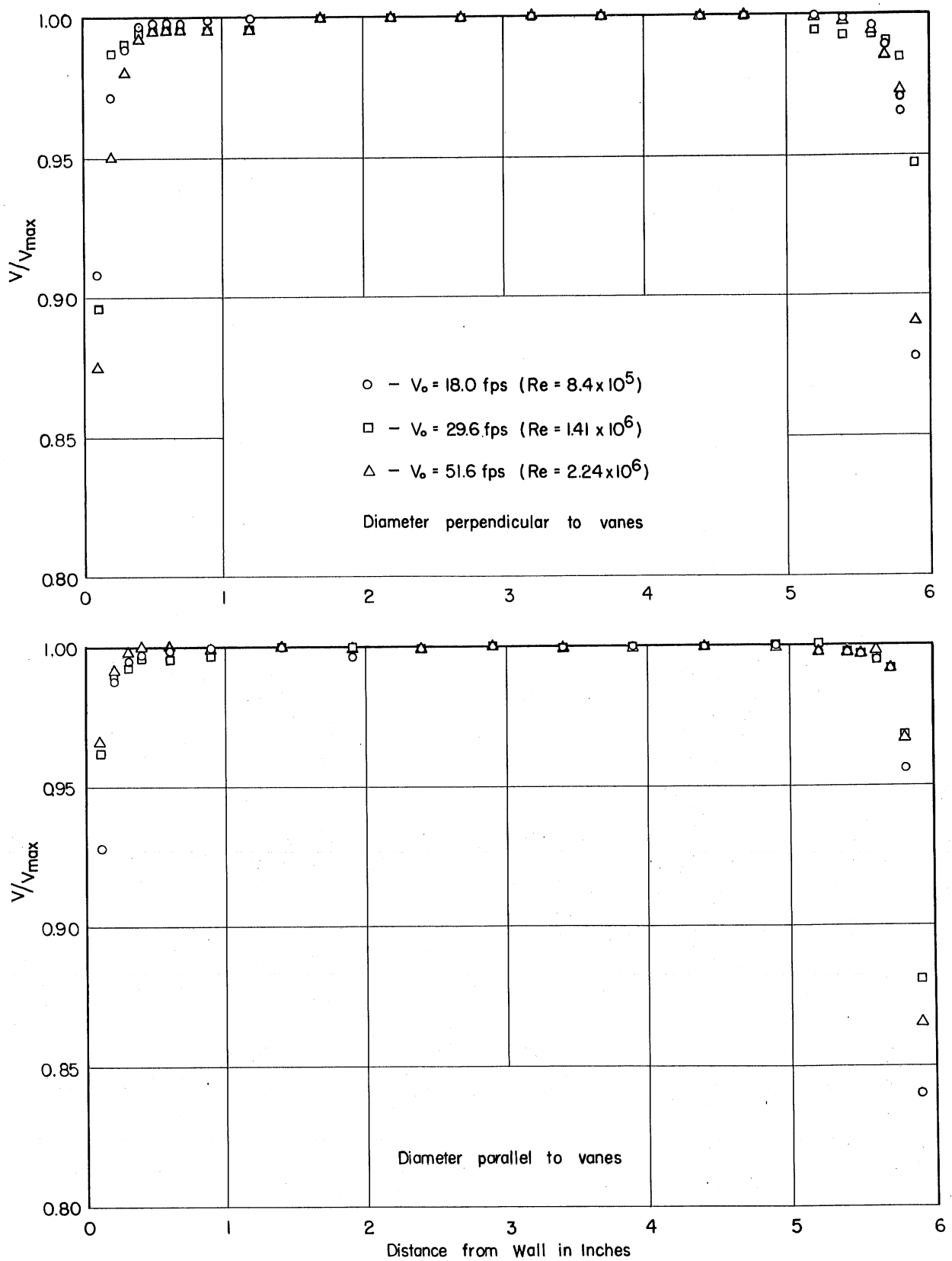

Fig. 44 - Measured Velocity Distribution at Downstream End of Closed-Jet Test Section

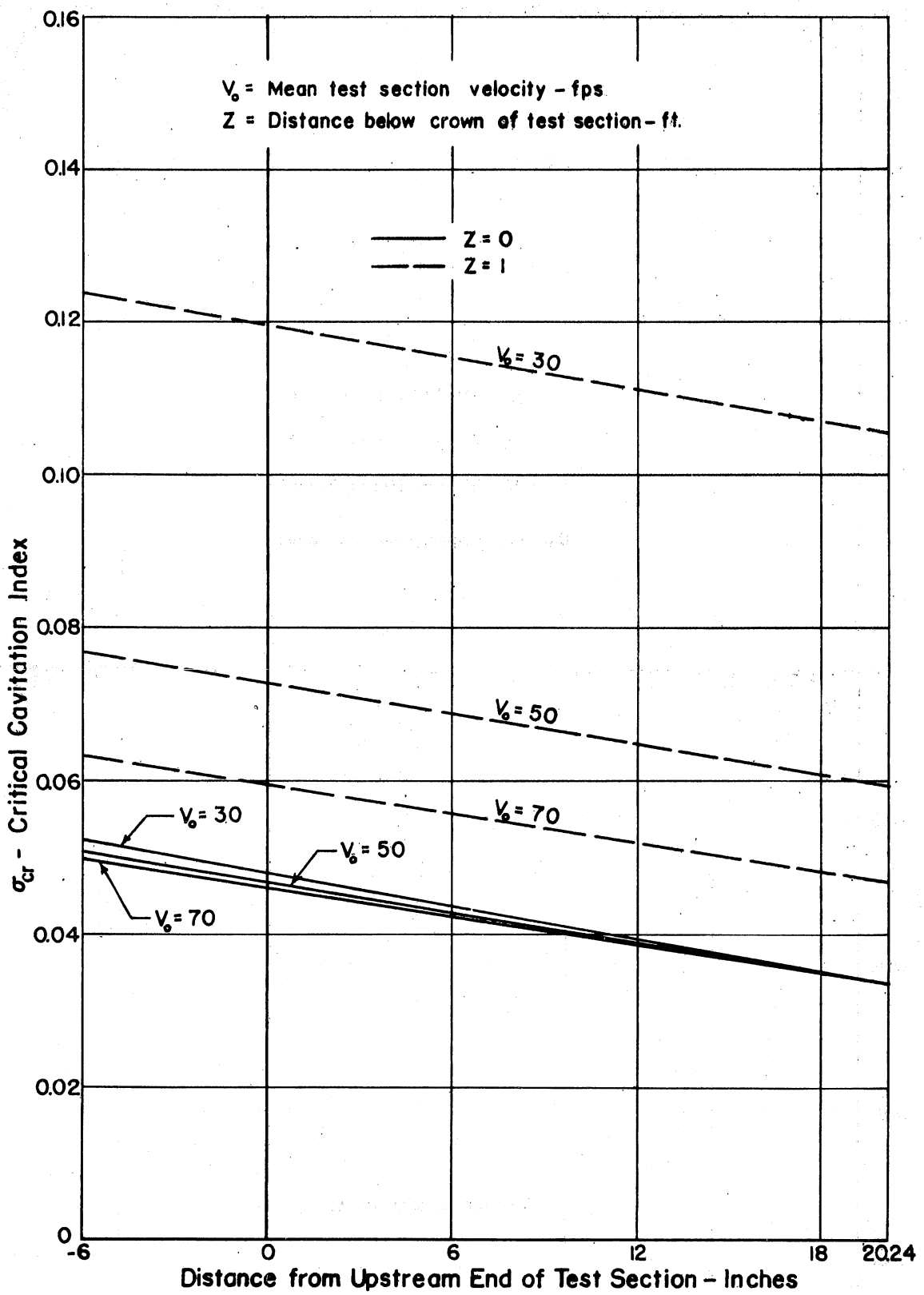

Fig. 45 - Critical Cavitation Indices in Prototype Closed-Jet Test Section

PART V. DIFFUSER STUDIES

A. Introduction

The function of the diffusers in the water tunnel circuit is to reduce efficiently the velocity of the test jet so that the stream may be accelerated as it enters the test chamber. This deceleration permits the velocities in the return circuit to be relatively low compared to the velocity of the test stream, and thus the head loss and power requirement of the tunnel are substantially reduced. The reduction in velocity and accompanying rise in pressure also increase the minimum cavitation index which will exist at the vaned elbows and the pump. This makes the satisfactory design of these components easier.

In decelerating the flow, the diffusers are expected to convert most of the kinetic energy of the test stream into pressure energy. This energy conversion must be accomplished with a minimum amount of energy loss and distortion of velocity distribution of the stream which might adversely affect other components of the circuit. Both of these conditions will be adequately fulfilled if the stream adheres to the walls of the diffuser throughout its entire length, that is, if no separation or backflow occurs in the diffuser. Separation occurs when the adverse pressure gradient in the diffuser becomes large enough to cause the fluid in the boundary layer near the wall to reverse its direction of flow. Since artificial methods of boundary-layer control are not considered feasible, primarily because of their expense and cavitation susceptibility, separation in a water tunnel diffuser must be prevented by making the angle of divergence of the diffuser small enough so that all of the stream can overcome the rise in pressure. Therefore, the diffuser downstream of the test section originally was designed to have a total angle of divergence of $6^\circ\ 40'$ and the diffuser following the pump in the prototype water tunnel was designed to be a 7° diffuser since divergence angles between 6° and 8° have been found to give optimum performance characteristics and economy of construction.

B. Velocity Distribution

Experimental studies on the diffusers consisted of determining velocity distributions at the entrance and exit of the two diffusers upstream of the pump and determining the pressure recovery and head loss in all three

diffusers. Velocity traverses at Station 4 were made with the 1/4-in. Pitot cylinder, and traverses at Stations 5, 6, and 7 (Fig. 21) were made with the 3/8-in. Pitot cylinder. In conformity with other sections of this report, velocity traverses made on diameters perpendicular to the guide vanes (in the plane of symmetry of the tunnel) are plotted with the abscissa scale measured from the wall which was on the outside of the tunnel loop. Traverses made normal to the plane of symmetry (parallel to the guide vanes) are plotted with the abscissa scale measured from the wall which was nearer to the control tower. The symbol V_o refers to the mean velocity of flow in a section 6 inches in diameter.

The distribution of velocity in the diffusers is of importance not only because it affects the energy loss in the diffusers and following tunnel components, but because a very nonuniform distribution at the exit of diffuser I may result in local velocities high enough to cause cavitation in the vaned elbow following it. These local high velocities also result in increased energy loss in the vaned elbow compared to what the loss would be if the velocity were more uniformly distributed. If the flow separates from the walls in the diffuser, the efficiency of the diffuser is made much lower because of the increased turbulent shear in the zone of separation. Finally, the excess kinetic energy in the nonuniform or separated stream will be almost entirely lost, since the distribution will become uniform at some point in the tunnel circuit, and the conversion of this excess kinetic energy to pressure energy is inherently inefficient. Thus it is seen that the more nonuniform the velocity distribution in a diffuser, the less satisfactory is its operation. If the velocity distribution of the stream leaving the diffuser is reasonably uniform, the pressure recovery of the diffuser will be high and the components of the tunnel following the diffuser will not be adversely affected.

The velocity distribution at the inlet to a diffuser is of great importance in determining the point of separation, exit velocity distribution, and head loss in the diffuser. This has been proved by several experimenters, and recent work on flow in diffusers at Pennsylvania State College [19 and 20] has shown that the efficiency is as much dependent upon the inlet velocity distribution as upon the angle of divergence. For this reason the velocity distribution at the entrance to the main diffuser was examined in some detail.

The distribution of velocity at Station 4 is presented in Figs. 46, 47, and 48. This station was 1/4-in. downstream from the entrance to the main

diffuser (diffuser I) when the open-jet test section was installed in the tunnel. Figure 46 represents the distribution of velocity which was measured when the 6 5/8-in. pick-up cone was installed; typical points have been plotted from traverses made on horizontal and vertical diameters at 18-, 30-, and 50-fps test section velocity and at pick-up cone gaps of 0 and 5/8 inch. No significant trend in variation of the test points for these 12 runs was noticed except that the velocity profiles were slightly unsymmetrical by differing amounts and in differing directions from run to run. It was decided that this asymmetry was the result of faulty alignment of the pick-up cone and downstream end plate with the jet axis. The misalignment was undoubtedly caused by straining of the whole tunnel structure either during assembly or after assembly when the temperature changed. This section of the tunnel had the least structural restraint and, therefore, most of the strain in the structure took place at this point. In no case did the asymmetry amount to as much as 0.1 inch.

It will be observed that the velocity distribution is essentially linear near the walls. This linearity is thought to be apparent rather than actual, since what is actually plotted is the square root of the measured total head minus a constant static head. However, the static pressure over the cross section of Station 4 was not constant but undoubtedly varied from a minimum near the walls to a maximum near the center of the stream, since the flow is converging as it enters the diffuser. The actual distribution of velocity is probably more nearly represented by the dashed line in Fig. 46. The fact that the measured total head is constant in the central region of the stream indicates that the velocity, and therefore the pressure, in this region must be practically constant. If this had not been so, energy would have been lost in the shear flow and the total head would not have been constant in this region.

Figure 47 shows the measured velocity distribution at Station 4 when the dynamometer shaft housing was installed in the contraction. The plotted velocity distribution was measured with zero pick-up cone gap at 18-fps test section velocity. The lack of similarity between the horizontal and vertical wake profiles mentioned in Part III is even more apparent here. The preceding discussion concerning the effect of flow curvature on the measured velocity distribution also applies to the runs made with the dynamometer shaft. One interesting feature of these traverses is that the velocity at the outside of

the tunnel loop is slightly lower than the velocity at the inside. This local velocity deficiency is believed to be caused by the wake of the struts which supported the contraction dynamometer shaft.

The velocity distribution presented in Fig. 48 was measured on diameters parallel and perpendicular to the guide vanes at a test section velocity of 18 fps with both 0- and 5/8-in. pick-up cone gaps when the 6 3/8-in. pick-up cone was installed in the test section. Evidence of curvature of the streamlines entering the diffuser is even more apparent in this plot; the indicated velocity distribution in the boundary layer is actually curved in the opposite direction from the normal velocity distribution in a boundary layer. This increase in curvature of the stream line is to be expected, since the smaller pick-up cone had a sharper curvature of its walls.

The velocity distribution in the entrance to the diffuser when the closed-jet test section was installed is presented in Fig. 44 and discussed in Part IV of this report.

The velocity distributions at the downstream end of diffuser I are presented in Figs. 49, 50, and 51. Figure 49 shows traverses at Station 5, which was in the diffuser 2 in. from its downstream end, made when each of the pick-up cones was in the open-jet test section. The curves are composites of runs at both 0- and 5/8-in. pick-up cone gaps, and show practically no difference in velocity distribution. The distributions are quite representative of fully developed diffuser flow and have the characteristic linear variation near the walls. The diffuser seems to be closest to separation at the top (on the outside of the tunnel loop) but separation has evidently not yet occurred.

The traverse shown in Fig. 50, which was made with a dynamometer shaft in the contraction, shows that the diffuser flow is just on the verge of separating at the top of the tunnel. The traverses made with the diffuser dynamometer shaft show no separation, but they do indicate how a boundary layer has been built up along the shaft. There was no discernible systematic difference in the velocity distribution between runs made with the two-strut shaft supports and the three-strut shaft supports.

Figure 51 shows that fully developed diffuser flow does not occur in diffuser I when the closed-jet test section is installed in the tunnel. The velocity distribution is uniform on the central quarter of both diameters.

The boundary layer has not developed fully because it started initially with a very small thickness.

The velocity distribution at the downstream end of the 9^{o} diffuser following the open-jet test section was determined in the cylindrical section in a plane 2 in. downstream from the end of the diffuser. The flow had evidently separated at the top of the diffuser (Fig. 51); no adverse effects of this separation were apparent other than a slight reduction in the efficiency of the diffuser.

Velocity traverses made at Stations 6 and 7 (upstream and downstream of diffuser II) are presented in Figs. 52 to 55. Since the ratio of end areas of this diffuser was quite small (1.21), the velocity distribution does not change much in passing through the diffuser. The distribution of velocities at these stations will be dealt with in the next section of this report, which is concerned with the studies of the vaned elbows. Velocity traverses upstream and downstream of diffuser III were not made for this study because of the difficulty of obtaining reproducible results immediately downstream of the pump. A traverse taken downstream of the same pump installation is shown in Fig. 5 of reference [7].

C. Energy Loss

The pressure difference across the diffusers was determined from wall pressure manifolds of three taps each at Stations 7, 9, and 10 and from manifolds of four taps at Stations 5 and 6. As mentioned in Part III, when the open-jet test section was installed in the tunnel, it was impossible to determine the average pressure at Station 4 from measurements of the wall pressure. The stream lines were curved so much at the walls that the wall pressure was appreciably lower than the average pressure. Also, this wall pressure was found to be unstable and varied in such a manner from run to run that the computed head loss of diffuser I and the open-jet test section varied over quite wide ranges when the pick-up cone gap was changed. It was therefore decided not to compute the head loss in the diffuser and in the open-jet test section separately, but rather to treat the entire section of the open-jet tunnel between the downstream manifold of the contraction and the end of diffuser I as one component when computing head loss. This is a valid simplification because the head loss in the open-jet test section should not be appreciably affected by a change in Reynolds number and the same is

true of diffuser I. The pressure difference between the manifold at the downstream end of the contraction and Station 5 was thus used to determine the head loss in the diffuser and open-jet test section combination. When the tunnel was operating with the closed jet, the difference in pressure between the downstream end of the test section and the pressure at the end of the diffuser was used to determine the head loss of the diffuser.

The energy loss in the diffusers was determined by measuring the velocity distribution and the difference in pressure upstream and downstream of the diffusers. The loss coefficient, K_o, which expresses the form loss of the diffuser in terms of the mean test section velocity head, was computed from the equation

$$K_o = \alpha_n \left(\frac{A_o}{A_n}\right)^2 - \alpha_{n+1} \left(\frac{A_o}{A_{n+1}}\right)^2 - \frac{\frac{p_{n+1} - p_n + p_f}{w}}{\frac{V_o^2}{2g}}$$

where α is equal to $\frac{\Sigma V^3 \Delta A}{A \bar{V}^3}$,

A_o is the cross-sectional area of the test section (sq ft),
A is the cross-sectional area of flow at a station (sq ft),
p is the pressure at a station (psf),
V_o is the average test section velocity,
n is the station number upstream of a diffuser, and
$n+1$ is the station number downstream of a diffuser.

The term p_f/w represents an assumed pressure drop due to friction on the walls of the diffuser [5] and was computed from the formula

$$\frac{p_f}{w} = \frac{f}{8 \tan\theta} \left(\frac{V_n^2 - V_{n+1}^2}{2g}\right)$$

where θ is the half-angle of divergence of the diffuser, and
f is the friction coefficient.

The friction coefficient was obtained from a standard friction coefficient-Reynolds number diagram. In the main diffuser, the loss due to friction was computed as two separate portions, one due to the smooth wall in the upstream end of the diffuser and the other due to the galvanized steel wall at the

downstream end of the diffuser. The introduction of the term p_f/w is intended to take into account variations in Reynolds number which will be encountered in extrapolating the data and is admittedly only an approximation. This method has been used by many previous investigators with apparently satisfactory results. The total loss coefficients for the prototype diffusers are not greatly changed by the assumed change in skin friction from model to prototype.

The pertinent experimental data used in determining K_o for the diffusers are collected in Tables VI and VII. The form of the tunnel when each test was made may be determined by reference to Table I. Whenever possible, tests were made for each tunnel form at pick-up cone gaps of 0 and 5/8-in. and at three test section velocities.

In computing the head loss in the open-jet and main-diffuser combination, the measured pressure difference in Table VI is the difference in pressure between the reference manifold in the contraction 1 1/2 in. upstream of the test section and Station 5. It was assumed that the velocity distribution was uniform at the reference manifold and thus that $\alpha = 1.000$. The values of α at other stations were determined by graphical integration of velocity traverses made at a test section velocity of approximately 45 fps. When an α-value was not determined directly, it was assumed to be the same as the α-value determined for the most nearly corresponding tunnel form. The ratios $(A_o/A_n)^2$ for all of the traverse stations are given in Table III. The presence of the dynamometer shafts at Station 5 and at the end of the contraction was taken into account in computing the data for runs B, F, and G. Values of K_o and data for the diffuser following the closed-jet test section are also included in Table VI (Form C).

It can be seen that there is some scatter of the data in Table VI, and this scatter is great enough so that no conclusions could be drawn concerning trends and differences in the data without making a statistical analysis. Accordingly, the data in the five runs which include all of the form loss coefficients determined for the 6° 40' diffuser and open-jet combination (runs A, B, E, F, and G) were subjected to a three-factor analysis of variance. This statistical method may be conveniently employed to detect any significant variability that may be contributed to the data by a change in level of the factors under consideration. The factors which might influence the form loss coefficients in Table VI are pick-up cone gap, speed of operation during testing, form of tunnel, and interaction of any two of the three factors mentioned

above. This analysis was based on a 5 per cent level of significance, which means that the probability is one in twenty that the conclusions drawn from the statistical analysis are wrong. Although this significance level may appear to be too rigorous for the intended application, it is the most liberal level used in statistical analysis and the highest level for which tables were available.

The analysis of variance of runs A, B, E, F, and G showed that there was significantly greater variability among runs than would be expected from a homogeneous group of data. In an attempt to reduce variability, run A was eliminated from the data under consideration, and the data for runs B, E, F, and G were then found to be homogeneous with respect to all three factors under consideration. This means that it is impossible to distinguish between values of the form loss coefficient entered in Table VI for these four runs. Therefore, the influences on K_o of the form of the tunnel, pick-up cone gap, and speed of operation during testing are so small that they are hidden by the errors of measurement and no definite conclusions about them can be drawn from the model studies. However, it is quite definite that the form loss coefficient is smaller for run A (6 5/8-in. pick-up cone without dynamometer shaft) than it is for the other four runs (6 5/8-in. pick-up cone and contraction dynamometer shaft, 6 3/8-in. pick-up cone without a dynamometer shaft, and 6 3/8-in. pick-up cone with a diffuser dynamometer shaft supported by either a two-strut or a three-strut system). The average value of K_o for run A is 0.1284 and the average for runs B, E, F, and G is 0.1384.

If the data are averaged across the columns so that speed of testing is not an influencing factor, it will be observed that there is a definite trend in each run for the loss coefficient to increase when the pick-up cone gap is increased from 0 to 5/8 inch. The analysis of variance showed that this increase (amounting on the average to 5 per cent of K_o) is so small that it cannot be claimed to be mathematically significant, and the conclusion is that the cone gap did not influence the head loss in the diffuser. Tests were not made at intermediate pick-up cone gaps because in order to claim significance for the findings, these tests would have to be made for every run. It is not expected, however, that a pick-up cone gap between 0 and 5/8 in. would give mathematically significant higher or lower values of K_o.

The form loss coefficients for the open-jet and 9°-diffuser combination (run D) are significantly greater than the loss coefficients in runs A,

B, E, F, and G. This is to be expected, since all previous research has indicated that the efficiency of diffusers decreases steadily as the total angle of divergence increases beyond 6°. The average value of K_o for the 9° diffuser and open-jet test section was 0.1478.

The data for the 6° 40' diffuser following the closed-jet test section are entered in Table VI as run C. The form loss coefficient for this component is computed for the diffuser alone and does not include any loss in the closed-jet test section. The difference in pressure entered in Table VI was measured between the downstream end of the closed-jet test section and Station 5, and the average of three values of α (α = 1.0037) was used at the upstream end of the diffuser. The form loss coefficients for this diffuser are quite small, the average being 0.0378.

It is interesting to compare the performance of this diffuser with previous experiments made to determine the efficiency of diffusers of different angles of divergence and having different inlet lengths. Interpolating among the values obtained by Peters [21] indicates that the efficiency of the form loss energy conversion should be 0.930. This efficiency is defined by the equation

$$\eta_o = \frac{\dfrac{p_{n+1} - p_n + p_f}{w}}{\dfrac{\alpha_n V_n^2 - \alpha_{n+1} V_{n+1}^2}{2g}} = 1 - \frac{K_o}{\alpha_n \left(\dfrac{d_o}{d_n}\right)^4 + \alpha_{n+1} \left(\dfrac{d_o}{d_{n+1}}\right)^4}$$

and the average value of η_o determined from the tests on the diffuser following the closed-jet test section is 0.9581. More recent investigations carried out at the Ordnance Research Laboratory at Pennsylvania State College define total energy efficiency on a slightly different basis:

$$\eta_e = \frac{\dfrac{p_{n+1} - p_n}{w} + \dfrac{\alpha_{n+1} V_{n+1}^2}{2g}}{\alpha_n \dfrac{V_n^2}{2g}}$$

The average value of η_e for the data for run C was 0.9375, which is somewhat lower than the value η_e = 0.960 which would be expected by extrapolating the data presented in the Pennsylvania State College report [20]. There is a possible explanation for this lowered efficiency in the fact that the area

ratio of the diffuser tested in this model study is approximately 4.0, as compared with an area ratio of 3.0 for the Pennsylvania State College experiments.

Adoption of the smaller pick-up cone in the final prototype design necessitated changing the design angle of the prototype main diffuser to 7° so that the tunnel could be constructed in the space available. This change in divergence angle of 20 minutes will probably increase the head loss of the open-jet and main-diffuser combination slightly. Interpolation between the average values of runs A and D indicates that K_o should be increased by about 0.0030. The predicted K_o for the final prototype open-jet and 7° main diffuser is therefore $K_o = 0.1414$. Reference [20] indicates that the coefficient of form loss of the diffuser with the closed-jet test section installed will be increased by approximately the same amount. The predicted K_o for the prototype main diffuser following the closed-jet test section is therefore 0.0408.

The wall friction loss of the prototype diffusers expressed as a fraction of the test section velocity head is shown in Table XI and was computed from the equation

$$K_f = \frac{\frac{p_f}{w}}{\frac{V_o^2}{2g}} = \frac{f}{8 \tan\theta}\left[\left(\frac{d_o}{d_u}\right)^4 - \left(\frac{d_o}{d_d}\right)^4\right]$$

where d_o is the diameter of test section,
d_u is the diameter at the upstream end of the diffuser,
d_d is the diameter at the downstream end of the diffuser, and
the other symbols were previously defined.

An adjusted value of $\tan\theta$ was computed for the prototype diffuser following the closed-jet test section to account for the added length of the diffuser due to the transition from test section to diffuser. Since the prototype diffuser is intended to be machined throughout its entire length, the value of f, the friction coefficient, for the smooth-pipe law was used. A value of f thought to be representative of the entire diffuser was chosen because the Reynolds number varied continuously along the diffuser.

The form loss coefficients for diffusers II and III in the model tunnel are given in Table VII, along with the pertinent data from which the

coefficients were computed. There is considerable scatter in the data for diffuser II; the form loss coefficient is greater for larger values of α at Station 6. There will be no diffuser in the vertical leg of the prototype water tunnel; however, there will be some head loss in excess of wall friction loss in the vertical leg upstream of the pump due to the inefficient pressure conversion of the high kinetic energy of the stream as it leaves vaned elbow I. It is estimated that in the prototype α will equal 1.30 at a point corresponding to Station 6 in the model and 1.20 at a point corresponding to Station 7. Assuming that one-half of this change in kinetic energy is converted into pressure will give an apparent form loss coefficient in the cylindrical section equal to 0.0030. The average value of the form loss coefficient between Stations 6 and 7 in the model was 0.0103.

Determination of the head loss in the diffuser downstream of the pump (diffuser III) is made difficult by the extremely complicated flow pattern at the discharge side of the pump in the model. As can be seen from Fig. 5, the pump fairwater extends into diffuser III. The stream entering the diffuser undoubtedly has considerable variation in both magnitude and direction of velocity, and this nonuniformity would also cause variations in pressure. In order to obtain an accurate measure of the head loss in this tunnel component, a careful survey of both velocity and pressure would have to be made at the entrance to the diffuser. Since the model pump and diffuser installation did not duplicate the proposed prototype (Figs. 4 and 5) it was thought that this component did not warrant extensive experimental investigation. The form loss coefficients (Table VII) were thus computed with an assumed value of α and with the tacit assumption that the measured wall pressure at Station 9 was equal to the average static pressure in the cross section. The average of 15 values of K_o so determined was 0.0183. It is thought, however, that this coefficient includes some loss which would normally be ascribed to the pump component; it is therefore estimated that the form loss coefficient for the diffuser following the pump in the prototype tunnel will be 0.0120.

D. Conclusions

On the basis of these experimental and analytical studies of the diffusers, it is concluded that:

1. There will be no separation in the 7° main diffuser of the prototype, although separation would probably occur if a 9° main

diffuser were installed. The velocity distribution will not be greatly affected by the presence of the diffuser dynamometer shaft and supporting struts.

2. More than one-half of the energy loss in the open-jet tunnel circuit will occur in the test section and main diffuser. The loss in these components is not appreciably affected by the pick-up cone gap or the presence of the diffuser dynamometer shaft. When the closed-jet test section is installed, the energy loss in the test section and main diffuser will be about one-half of what it is with the open jet installed.

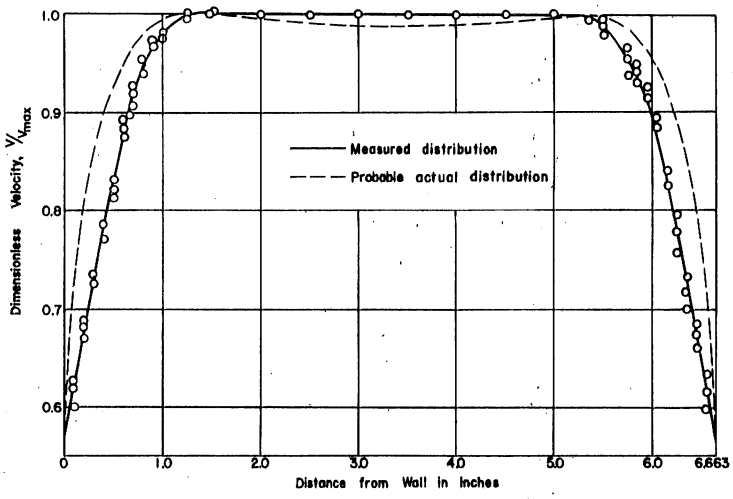

Fig. 46 - Velocity Distribution at Station 4 with 6 5/8-in. Pick-Up Cone (Tunnel Form A)

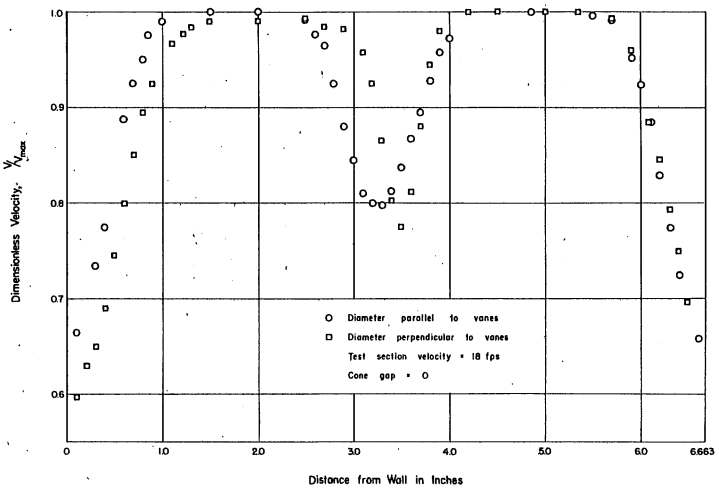

Fig. 47 - Velocity Distribution at Station 4 with 6 5/8-in. Pick-Up Cone and Contraction Dynamometer Shaft (Tunnel Form B)

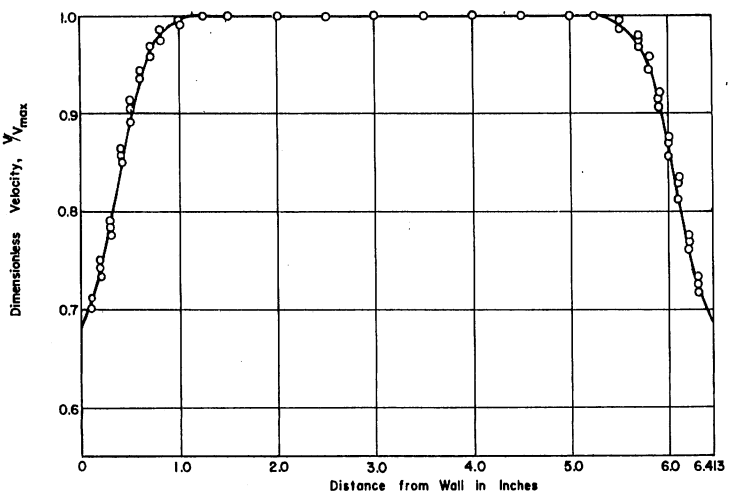

Fig. 48 - Velocity Distribution at Station 4 with 6 3/8-in. Pick-Up Cone (Tunnel Form E)

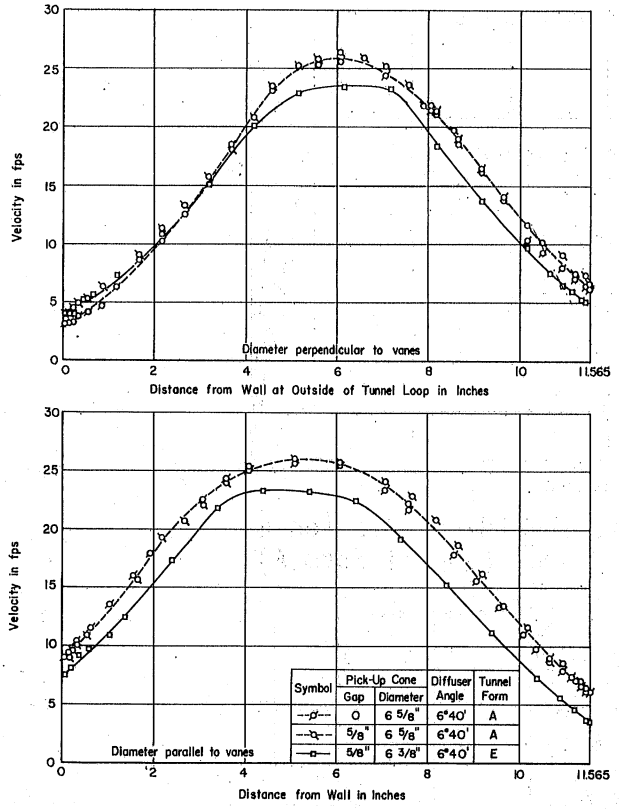

Fig. 49 - Velocity Distribution at Station 5 (Tunnel Forms A and E)

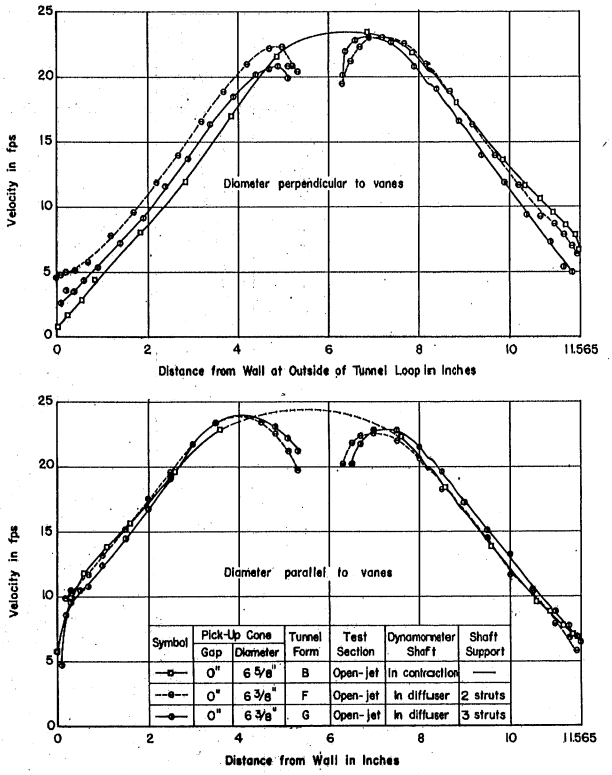

Fig. 50 - Velocity Distribution at Station 5 (Tunnel Forms B,F, and G)

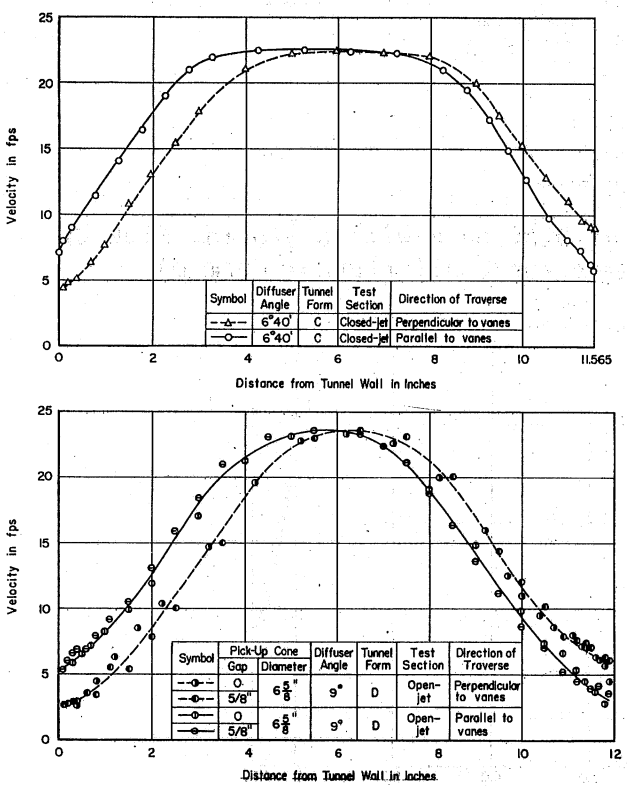

Fig. 51 - Velocity Distribution at Station 5 (Tunnel Forms C and D)

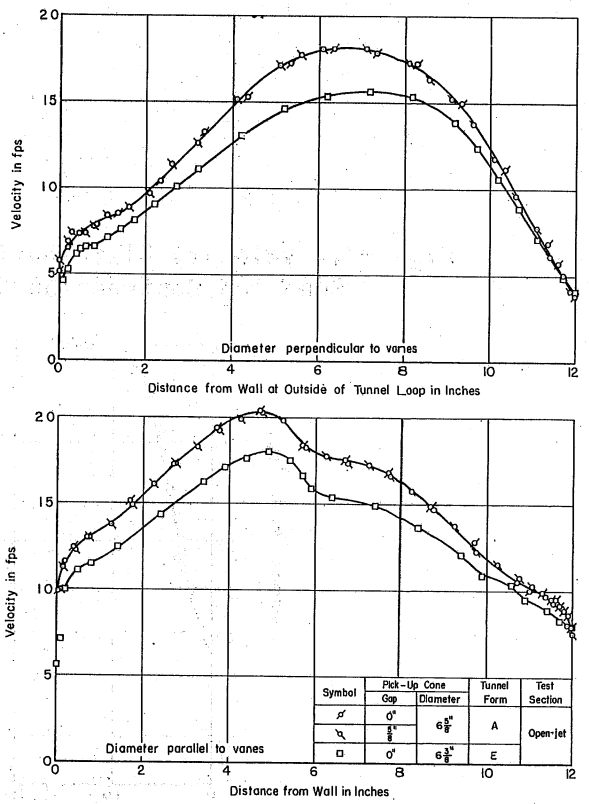

Fig. 52 - Velocity Distribution at Station 6 (Tunnel Forms A and E)

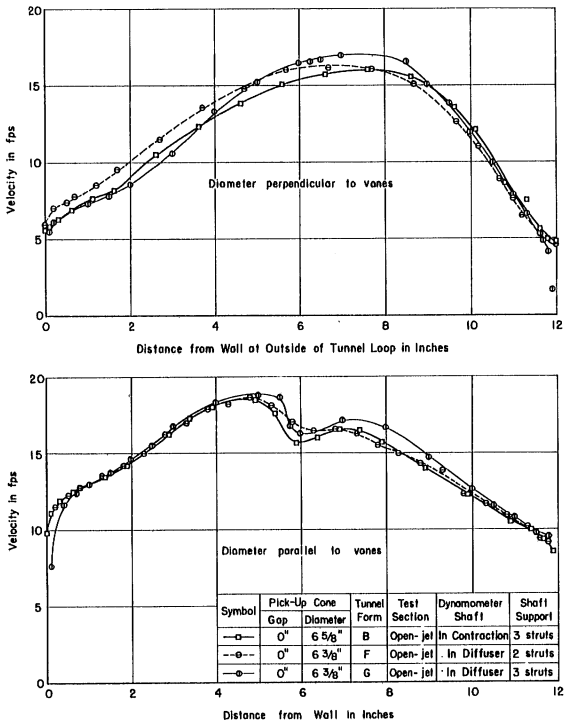

Fig. 53 - Velocity Distribution at Station 6 (Tunnel Forms B, F, and G)

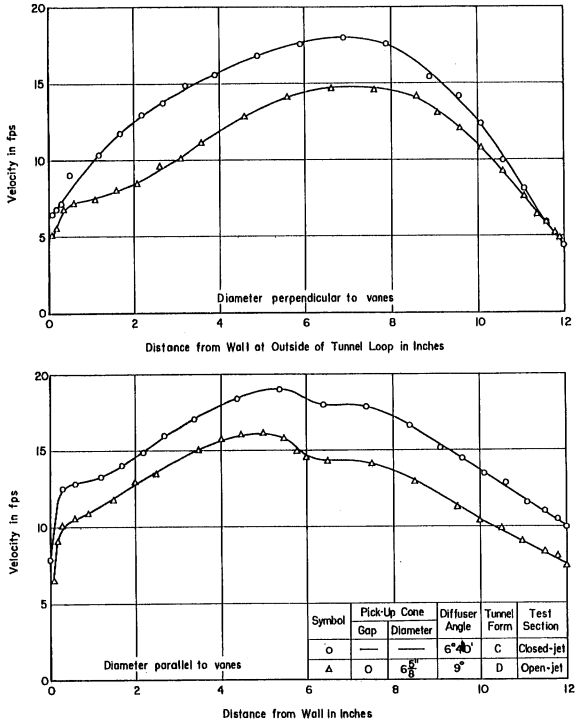

Fig. 54 - Velocity Distribution at Station 6 (Tunnel Forms C and D)

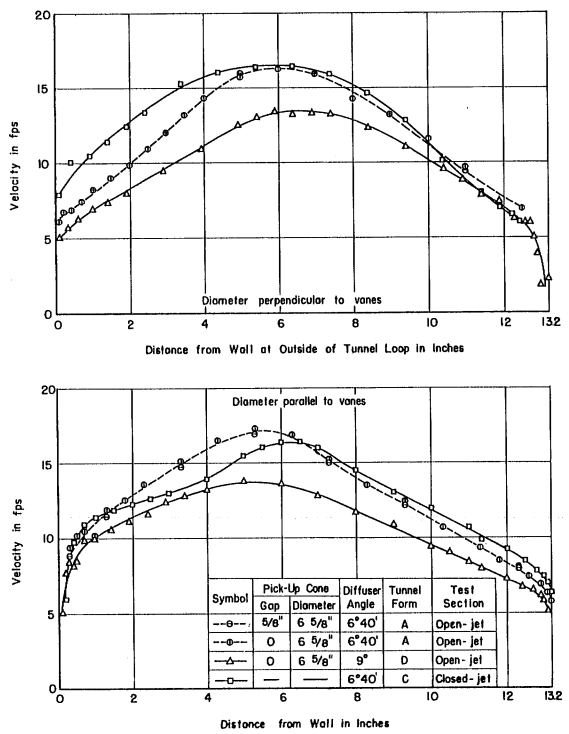

Fig. 55 - Velocity Distribution at Station 7 (Tunnel Forms A, D, and C)

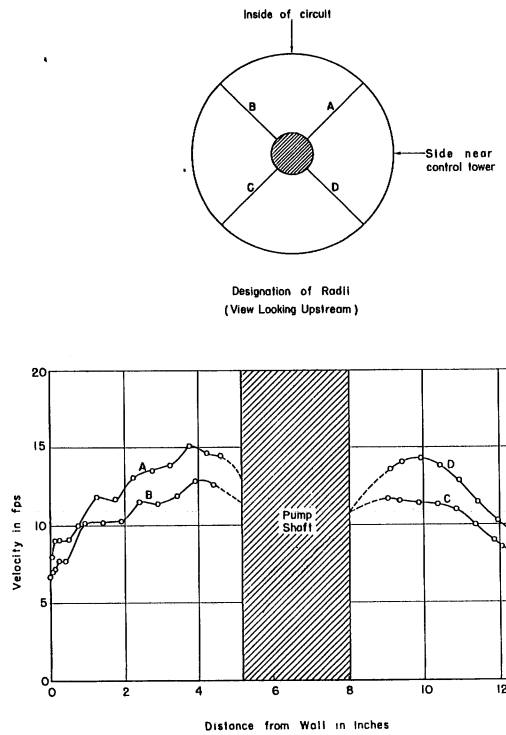

Fig. 56 - Velocity Distribution at Station 8 (Tunnel Form A)

PART VI. VANED ELBOW STUDIES

A. Introduction

The function of the vaned elbows in the water tunnel is to divert the stream through 360° so that it may be returned to the contraction after it leaves the main diffuser. This flow diversion must be accomplished without contributing appreciable distortion to the velocity distribution or causing large-scale vortices. Such disturbances in the flow would cause the test stream to be nonuniform and unsteady. Secondarily, the flow diversion should take place with small energy loss and without cavitation or vibration of the vanes.

The guide vane cascade used in this model study is the same one that was used previously in the model study of the 60-in. prototype closed-jet tunnel. The action of this cascade was thoroughly investigated in the previous study [6] both in the model water tunnel and in a special test stand. The experimental investigations for the present study were mainly concerned with the influence of shafts or shaft fairings intersecting the cascade of vanes.

B. Velocity Distribution

The measured velocity distributions upstream (Station 5) and downstream (Station 6) of vaned elbow I are shown in Figs. 49 to 54. These figures show that the flow diversion is being accomplished with satisfactory outflow velocity distribution. The traverses at Station 5 show that the incoming stream is slightly asymmetrical, with the highest velocity occurring nearest the inside of the bend. The same tendency is apparent at Station 6 in all runs, indicating that the cascade has diverted the flow through the correct angle of 90°. The velocities near the wall are higher and the maximum velocities are lower at Station 6 than at Station 5. This action is beneficial even though the head loss of the cascade is thereby increased, because this smoothing action insures a more uniform stream at the upstream end of the pump. The depression in the velocity distribution on the diameter parallel to the vanes at Station 6 is the wake of the splitter shown in Figs. 5 and 20.

The velocity distribution upstream (Station 7) and downstream (Station 8) of vaned elbow II are shown in Figs. 55 and 56. Although the prototype

will not have a vaned elbow upstream of the pump, the head loss and velocity distribution data on this component are presented because they show the influence of a thick shaft fairing in an elbow. The velocity distribution downstream of the elbow is apparently satisfactory, although a concentration of the flow on the side nearest the control tower is apparent. This distribution is reasonable since the same asymmetry existed upstream of the elbow. The velocity distribution at Station 8 is symmetrical with respect to a horizontal plane, while the stream would be expected to have a higher velocity on the outside of the circuit in view of the velocity distribution at Station 7. This indicates that the elbow is overturning the flow, which is not detrimental in this particular instance. The irregularities in the distribution at Station 8 on radii A and B are probably the wakes of individual vanes, since these radii were quite close to the guide vanes.

No velocity traverses were made upstream of vaned elbow III, but velocity traverses were made downstream of this elbow (and upstream of vaned elbow IV) at Station 11. These traverses (Fig. 57) indicate that the distorted velocity distribution downstream of the pump has been adequately smoothed out by the stilling length downstream of the pump. The velocity distribution downstream of vaned elbow IV at Station 12 (Figs. 58 and 59) indicates some overturning of the flow when the contraction dynamometer shaft was installed. This stream is evidently crowded into the lower half of the downstream conduit by the presence of the shaft; the effect is more apparent with the larger upstream diameter of the shaft. However, the influence of this distortion was not carried through to the flow in the test section. A slight depression was noticeable in the velocity distribution at Station 12 when the contraction dynamometer shaft was removed and the sleeve through which it passed was left in place. This depression left no noticeable trace of a local velocity deficiency in the test section, and installation of the nosepiece and tailpiece in the sleeve did not noticeably change the flow at Station 12 (Fig. 58).

C. Energy Loss

The energy loss in the vaned elbows was determined by measuring the velocity distribution and difference in pressure upstream and downstream of an elbow. The loss coefficient, ζ, which expresses the form loss of the elbows

in terms of the mean velocity head in the conduit upstream of the elbow was computed from the equation

$$\zeta = \frac{\frac{(p_n - p_{n+1})}{w}}{\frac{\bar{V}_n^2}{2g}} + \alpha_n - \alpha_{n+1}\left(\frac{A_n}{A_{n+1}}\right)^2 - f\frac{\ell}{d_n}$$

where α is equal to $\frac{\Sigma v^3 \Delta A}{A\bar{V}^3}$,

A is the cross-sectional area of flow (sq ft),
p is the pressure (psf),
$\bar{V}_n$ is the average velocity upstream of the elbow,
f is the friction coefficient,
ℓ is the centerline length of conduit between Station n and Station n+1,
d_n is the diameter of conduit upstream of the elbow,
n is the station number upstream of the elbow, and
$n+1$ is the station number downstream of the elbow.

The pertinent experimental data used in determining ζ are collected in Tables VIII, IX, and X. The form of the tunnel when each test was made can be determined by comparing the listed run number with the schedule in Table I.

The form loss coefficient for vaned elbow I (Table VIII) is somewhat higher than the usual loss coefficient for a cascade in a uniform stream, which should be about 0.15. The average of 39 determinations of ζ in this elbow was 0.236. However, the increase in form loss is to be expected in this particular installation because of several factors. First, and probably most important, there is a rather large decrease in kinetic energy between the stations upstream and downstream of the elbow. This is due both to the slight increase in area from Station 5 to Station 6, and to the decrease in the value of α of the more uniform stream downstream of the elbow. This change in kinetic energy is manifested in a pressure gain as the stream goes through the elbow, in contrast to the usual pressure drop. Thus, besides diverting the flow, this tunnel component is actually functioning as a diffuser, and it is not surprising that the loss coefficient is higher than in a normal vaned elbow.

A second factor contributing to the increased loss coefficient of the elbow is the splitter, which was installed in the elbow during the entire

testing program. The friction and form drag on the splitter are both included in the coefficient ζ; the splitter also has the detrimental effect of halving the aspect ratio of the flow passages in the cascade. A third factor causing increased energy loss is the fact that if a cascade contains many vanes, the loss coefficient of the cascade in a nonuniform stream should be greater than the loss coefficient in a uniform stream by the factor a, which can be easily demonstrated by considering the losses in individual stream tubes somewhat larger than the vane spacing. However, in an actual guide vane installation this conclusion would have to be modified in view of the relatively few vanes used. Taking all of the above factors into consideration, there are valid reasons for the loss coefficient being as high as it is. The average form loss coefficient of the elbow expressed in terms of the test section velocity head is $K_o = 0.0156$.

The loss coefficients for vaned elbow II (Table IX) are much higher than for vaned elbow I. The average of 39 determinations of ζ was 0.492, which gives $K_o = 0.0210$ if the head loss is expressed in terms of the test section velocity head. This high loss coefficient is thought to be mainly due to the presence of the thick splitter in this elbow which housed the pump drive shaft housing.

The form loss coefficient for vaned elbows III and IV was computed as a single loss coefficient when elbow IV was unobstructed (runs A and C, Table X). The average of nine determinations gave $2\zeta = 0.276$, which corresponds very closely to the value to be expected for these cascades in a uniform stream. When the contraction dynamometer shaft was installed, the average value of ζ for vaned elbow IV was 0.189 with the smaller upstream diameter of the shaft (run B) and 0.225 with the larger upstream diameter of the shaft (run H). The tests made with the sleeve in the cascade but with the dynamometer shaft removed (runs I and J) indicate that the loss coefficient of the elbow is not greatly affected by the presence of the sleeve alone. The average form loss coefficient for vaned elbows III and IV together will be $K_o = 0.0034$, and when the contraction dynamometer shaft is installed this will be increased to $K_o = 0.0042$.

D. Vane Cavitation Analysis

Vaned elbow I will be more susceptible to cavitation than any other elbow since the lowest absolute pressure and highest velocity that act on a

guide vane will occur there. Cavitation cannot occur on the vanes unless the pressure drops to near vapor pressure at some point on the vane. Experimentally, it was determined that the lowest negative pressure coefficient on the vanes is 2.25 [6]. This coefficient is actually the approximate cavitation index at which cavitation will begin on the guide vanes, since the cavitation index is defined by

$$\sigma = \frac{\frac{(p - p_{vp})}{w}}{\frac{V^2}{2g}} \tag{1}$$

where p/w is the absolute pressure head in the undisturbed stream (ft),

p_{vp} is the vapor pressure (ft), and

V is the velocity of the stream impinging on the guide vane (fps),

the critical value of p/w is $2.25\ V^2/2g + p_{vp}/w$. If the cavitation index of the guide vanes does not fall below 2.25, the vanes will not cavitate. This index can be computed quite readily for the tunnel operating with either the open-jet or closed-jet test section installed in the tunnel. If the open jet is installed, the test stream will begin to cavitate noticeably when the pressure head at the crown of the downstream end of the contraction falls below $0.40\ V_o^2/2g + p_{vp}/w$ (Part III). The pressure difference between the downstream end of the contraction and the downstream end of the diffuser can be computed using Bernoulli's theorem, since the head loss between these two points is known (Part IV). The absolute pressure head on the centerline at the downstream end of the prototype diffuser when the test section has begun to cavitate will be

$$\frac{p}{w} = \frac{p_{vp}}{w} + \left[0.40 + \alpha_o - \alpha_5 \cdot \left(\frac{V_5}{V_o}\right)^2 - K_o - K_f\right] \frac{V_o^2}{2g} + 1$$

or

$$\frac{p - p_{vp}}{w} = (0.40 + 1.0000 - \frac{1.65}{16} - 0.1414 - 0.0135)\ \frac{V_o^2}{2g} + 1$$

The model tests showed that, with the open jet installed, the maximum local velocity U at Station 5 was twice the average velocity at this station (equal

to $V_o/2$ since the average velocity at this station is $V_o/4$); hence, the minimum value of the cavitation index on any guide vane will be

$$\sigma = 4.57 + \frac{4}{\frac{V_o^2}{2g}}$$

when cavitation is incipient in the open-jet test section. If it is assumed that the pressure at the top of the 5-ft diameter cylinder surrounding the open jet is vapor pressure, the minimum cavitation index on the guide vanes will be

$$\sigma = 2.97 + \frac{10}{\frac{V_o^2}{2g}}$$

which would make $\sigma = 3.226$ when $V_o = 50$ fps. Thus it is seen that the open-jet test section would have to be cavitating very severely in order to make the minimum σ at the guide vanes fall as low as 3.5, and under no conditions of operation can the cavitation index of the vanes reach a critical value.

When the closed-jet test section is installed, the minimum cavitation index attainable at the guide vanes will be even higher. Assuming that vapor pressure exists at the crown of the downstream end of the closed-jet test section, application of Bernoulli's equation, taking into account friction and form loss in the diffuser, will show that the absolute pressure head at the centerline of the downstream end of the diffuser will be

$$\frac{p}{w} = \frac{p_{vp}}{w} + (1.0045 - \frac{1.411}{16} - 0.0405 - 0.0186) \frac{V_o^2}{2g} + 1 \qquad (2)$$

The model studies showed that the maximum velocity at the downstream end of the diffuser with the closed-jet test section installed will be 1.528 times the average velocity at this section. Substituting $V = 1.528\ V_o/4$ in Eq. (2), Eq. (1) shows that the minimum cavitation index at the guide vanes will be

$$\sigma = 5.88 + \frac{6.86}{\frac{V_o^2}{2g}}$$

Hence, it can be stated that under no form of operation of the prototype tunnel can the guide vanes serve as the initial source of tunnel cavitation. This is borne out by the fact that no cavitation was observed on any of the guide vanes, even under the most severe cavitation conditions of the model tunnel.

E. Vane Vibration and Stresses

Since trouble has been encountered in some water tunnels due to structural failure and excessive vibration of the guide vanes, an approximate analysis of the structural qualities of the prototype vanes was undertaken. Only the longest vane in each of the elbows was analyzed, since it would be subjected to higher stresses and have a lower natural frequency of vibration than any other vane in the elbow. The cross-sectional shape of the vanes is the same as that indicated in reference [6]; in Table III of that report are tabulated the moments of inertia and cross-sectional areas of both solid steel vanes and hollow steel vanes for use in a 60-in. water tunnel. These same physical characteristics for the vanes for a 24-in. tunnel were determined by applying a length ratio (L_r) of 0.4 to the above values; thus, the thickness of sheeting on the hollow vane was computed as 1/2 in. times 4/10, or 0.2 inch. The length of the vane in elbows III and IV was taken as 6 ft, the diameter of the elbow. The length of the vane in elbow I was taken as 2 ft, one-half the diameter of the elbow, because of the fairing which splits this elbow. The vanes were considered to be simply supported with respect to the minor principal axis (approximately parallel to the chord), since there will probably be little restraint in this direction at the supports, and fully restrained at the ends with respect to the major principal axis.

The forces acting on the vane are the lift-drag resultant force and the dead weight in water of the vane. In computing the dead weight in water of the hollow vane, the interior of the vane was assumed to be filled with water. The components of the lift-drag resultant force were obtained using the impulse and momentum principle, since integration of pressure distribution on the vane in the flow diversion apparatus [6] agreed with the results of this principle within a few per cent. The velocities used in computing the lift-drag resultant were based on a test section velocity of 40 knots. The velocity which impinges on the central vane of each elbow was obtained from the average velocity of flow for the given elbow by applying the relationship

between these values obtained from tests of the model. For elbows III and IV, this indicated that the velocity over the central vane would be uniformly 10 per cent larger than the average velocity of flow for the elbow; for elbow I the velocity over the central vane would vary from 95 per cent larger than the average velocity at the center of the elbow to 25 per cent smaller than the bulk velocity at the outside ends of the vane (Fig. 49). The point of application of the lift-drag force was obtained from graphical integration of the pressure distribution. Since this force does not act through the center of gravity of the section, a small amount of torsion will be present in the vane.

The stresses in the vanes resulting from the application of the above forces are very small. The maximum flexural stress does not exceed 2000 psi in either the solid vane or the hollow vane. The maximum flexural stress in the solid vane occurs in elbow III, and the maximum flexural stress in the hollow vane occurs in elbow I. The average support shear stress and the torsional shear stress do not exceed 200 psi; the maximum values occur in the hollow vane in elbow I. The maximum deflection of the vanes occurs in elbow III for both the solid vane and the hollow vane, but does not exceed 0.015 in. for either vane.

It should be noted here that axial compressive stresses will be set up in the vanes if they are not free to expand into the walls of the tunnel when the temperature of the water rises. If the water temperature rises above the room temperature to such an extent that there is a 60° F temperature difference between the vanes and the vane frames, these stresses will become critical and could conceivably cause failure of the vanes due to column-buckling action.

Vibration of the vanes will, in all probability, not be serious unless the natural frequency of one of the vanes is in or near resonance with some regular pulsating force. The vane having the lowest natural frequency of vibration will be the largest vane in elbows III and IV. The natural frequency of a beam can be computed from the equation

$$f = C\sqrt{\frac{gEI}{wL^4}}$$

where, using consistent dimensions,

C is a dimensionless constant, depending on mode of vibration and support of the beam,

g is the acceleration of gravity,

E is the modulus of elasticity,

I is the moment of inertia,

w is the weight per inch vibrated, and

L is the span.

The lowest value C can have for a beam with two supports is 1.57, which is the constant for a simply supported beam vibrating at its fundamental frequency. Vibration of a vane will cause some water to be vibrated with it, thus increasing w and lowering the frequency of vibration. It is assumed that one vane will vibrate the volume of water contained between it and an adjacent vane. Using these assumptions, which are conservative, the lowest frequency of vibration for either a solid or a hollow steel vane is 36 cycles per second; the two have the same frequency because the moment of inertia-weight ratio is the same for both. The frequencies of vibration for other vanes will be higher than this value since the spans are shorter.

There are two possible sources of excitation of a vane, pulses from the impeller and the vortices shed from the vane. The impeller will operate at a top speed of 6.25 rps and will have four blades; hence, the highest frequency of pulsation will be 25 cycles per second. If five straightening vanes follow the impeller, it is possible that a small exciting pulsation of 125 cycles per second will be generated. However, if these pulses occur, they will be small and considerably damped before they reach elbow III. The wake frequency of the vortices shed from the vane can be computed from the Strouhal number

$$S = \frac{fc}{U}$$

where S is the Strouhal number,

f is the frequency of vibration,

c is the chord length, and

U is the velocity of the free stream.

This dimensionless number is sensibly constant for a range of Reynolds number at which vanes operate; experimentally, S = 0.15 for airfoils [22]. The maximum frequency of wake vortices is thus 5 per second for a velocity of 33 fps in elbow I.

The foregoing analysis indicates that the fundamental frequency of vane vibration is higher than the frequency of the primary forces which might excite the vane. While this does not preclude the possibility of vibration of the vanes, it does give some assurance that resonant vibrations will not occur. There remains the possibility that model propellers mounted in the test section will operate at speeds in the range of resonance of the vanes. It is believed that impulses from this source will be sufficiently damped in traveling the length of the diffuser that they will not cause serious vibration of the vanes.

F. Conclusions

On the basis of these experimental and analytical studies of the vaned elbows it is concluded that:

1. The intersection of the dynamometer shafts with the vaned elbows will not cause detrimental velocity distribution or excessive energy loss.

2. The vanes in the elbows will not be subject to cavitation.

3. The vanes will be free from excessive stresses or deflections under all expected conditions of operations, and will not vibrate in resonance with either the tunnel impeller or vortices shed from the vanes.

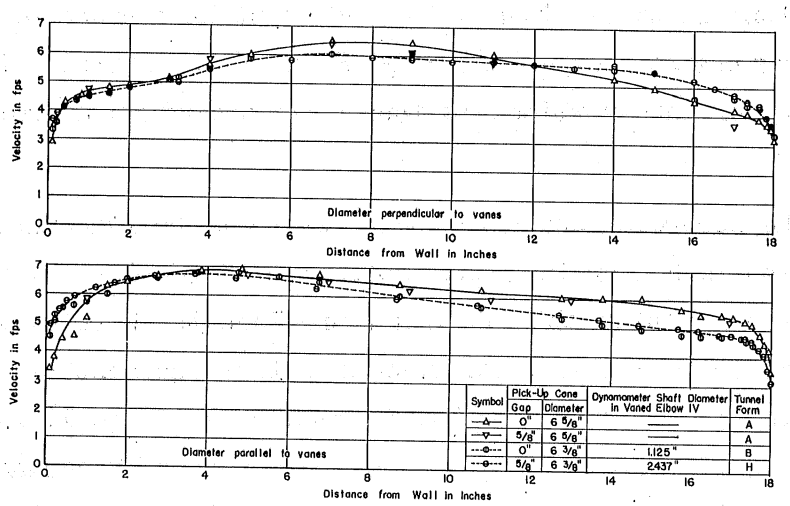

Fig. 57 - Velocity Distribution at Station 11
(Tunnel Forms A, B, and H)

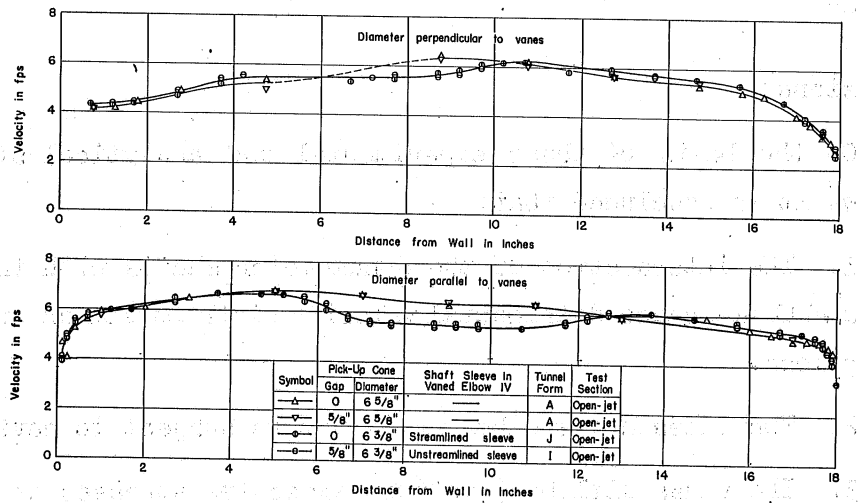

Fig. 58 - Velocity Distribution at Station 12
(Tunnel Forms A, J, and I)

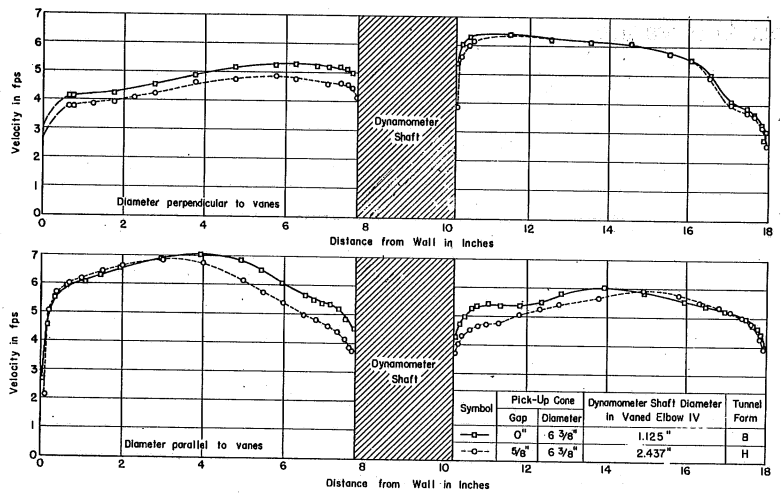

Fig. 59 - Velocity Distribution at Station 12
(Tunnel Forms B and H)

PART VII. PUMP STUDIES

A. Introduction

The purpose of the pump in a water tunnel is to supply energy to the circulating stream so that the resistance of the circuit can be overcome. In most pump installations, the required head-discharge relation is the only important requirement for which the pump is designed; but in a water-tunnel installation, the secondary characteristics of the pump must be carefully controlled. Some of these secondary characteristics which would seriously affect the performance of the water tunnel are pulsation, cavitation, noise level, stream rotation, and outflow velocity maldistribution.

The pump and drive unit of the existing 24-in. water tunnel at Taylor Model Basin is intended to be used in the new 24-in. tunnel. This part of the report will discuss the conditions under which this pump unit will operate in the new installation, and estimates will be made of the limits of operation of the tunnel using the old pumping unit.

B. Head, Discharge, and Power Requirements

The maximum test section velocity obtainable will be limited by the pump and power supply of the existing drive unit. The head to be added to the flow will be approximately proportional to the square of the test section velocity or of the discharge. This head, which will be equal to the total resistance of the circuit, can be computed by adding the resistances of the individual components of the circuit as determined in the model tests. The loss of each component is tabulated in Table XI and, for convenience in summarizing, each individual loss is expressed as a fraction (K_o) of $V_o^2/2g$, the mean test section velocity head. The friction losses of the straight cylindrical conduits were computed from values of $\underline{f}$ for a steel surface obtained from a standard curve of pipe friction against Reynolds number. The sum of the values of K_o and K_f for four different forms of the tunnel are listed at the bottom of Table XI. This summation does not include a loss coefficient for the elbow just upstream of the pump, since this component was undoubtedly considered to be part of the pump in the pump-rating tests. The total head-requirement coefficient given on the last line of Table XI was computed assuming that a cavitating disk 4 inches in diameter and having a coefficient of drag of 1.20 was in the closed-jet test section. This addition simulates the

losses which might be expected from a large, badly formed test body. The form loss coefficient of the main diffuser was increased by 0.0100 $V_o^2/2g$ for this condition.

The total head and power that will have to be added by the pump are shown, for four different conditions, in Fig. 60; the head-discharge curve under which the pump will have to operate is shown in Fig. 61. The available head, discharge range, and power requirements of the 48-in. pump which will be used in the water tunnel are given in reference [1] and are summarized in Fig. 61. The pump is rated as follows:

Revolutions per minute	350
Total dynamic head	19 ft
Gallons per minute	75,000

The pump motor is rated at 750 hp, but the existing power supply limits the actual power which the motor can develop to 400 hp. The power for both the pump drive and the dynamometer is supplied from two separate generators which are driven by a 600-hp synchronous motor. Both generators are equipped for Ward-Leonard control, and weakening of the field of the pump motor provides further speed regulation [23]. It can be seen by examining the curves of Fig. 61 that the pump will be operating throughout the entire range of discharge at heads considerably lower than those for which it was designed. The dashed portions of the rating curves are extrapolations of the pump data given in reference [1] and may be somewhat in error. The extrapolated curves indicate that a test section velocity of 61 fps with the open-jet test section installed and 65 fps with the closed jet installed can be obtained at 350 rpm, if sufficient power can be supplied. Efficiencies of an axial-flow impeller may drop off sharply in this range of operation; extrapolation of the efficiency curves indicates that pump efficiency at 350 rpm will be 68 per cent for the open jet and 52 per cent for the closed jet. Reference to Fig. 60 will show that 288 hp and 212 hp, respectively, will have to be added to the flow by the pump. Dividing these requirements by the above efficiencies will show that the pump drive motor will have to deliver 426 hp to give a test section velocity of 61 fps (36 knots) in the open-jet test section and 408 hp to give a test section velocity of 65 fps (38.5 knots) in the closed-jet test section. Since the test section velocity is very closely a linear function of the cube root of the horsepower, it is estimated that with 400-hp input to the pump,

the maximum test section velocity will be 35 knots in the open-jet test section and 37.5 knots in the closed-jet test section. If the 150 hp normally available to the torque dynamometer could be supplied to the pump drive motor when the dynamometer is not in use and if the speed of the pump drive motor could be increased to about 410 rpm by suitably weakening the field, it should be possible to attain a velocity of 71.5 fps (42.5 knots) in the closed-jet test section. One advantage of operating in the range of low head and high discharge of an axial-flow impeller is that the discharge at a given speed of revolution will change only slightly with an increase or decrease in head. Thus, if the head required of the pump is changed (for instance, by changing the advance ratio of a model propeller), only a slight adjustment of pump speed will be required to keep the test section velocity constant.

C. Velocity Distribution

Uniform distribution of inflow velocity is important to efficient, pulse-free operation of the pump. If the inflow is distorted and has isolated regions of both high and low velocity, an impeller blade will operate at a varying angle of attack during one revolution. This would probably lower the efficiency of the pump and might cause pulsing power demand and pulsing outflow. The pump and the elbow upstream of it in the model studies were not models of the pumping unit that will be used in the prototype; consequently, no summary prediction can be made concerning the distribution of velocity immediately upstream of the pump. However, on the basis of the model studies, it can be predicted that the velocity at the inflow to the elbow upstream of the pump will be essentially symmetrically distributed with a maximum velocity about 30 per cent greater than the average (Fig. 55). This distribution should not in itself be detrimental to operation of the pump. However, the flow passage in the elbow could deform this velocity so that pulsations might be set up in the pump.

The distribution of velocity downstream of the pump will be determined by the inflow distribution to the pump and by the design of the pump straightening vanes and hub fairing. Ideally, the outflow should be free from rotation and as uniform as possible. However, the stilling length of 43.5 ft of 6-ft diameter conduit (combined with the effect of vaned elbows III and IV) will change a maldistributed outflow velocity to the normal turbulent distribution. The smoothing action of the stilling length on the velocity distribution

can be seen by comparing Fig. 57 of this report with Fig. 5 of reference [7]. The latter figure is a velocity traverse made downstream of the same pump and diffuser which were used in this model study, and it will be noted that the velocity distribution downstream of the pump is quite badly distorted. The distribution at Station 11 (in the vertical leg of the stilling length) is satisfactorily uniform, however, as shown in Fig. 27 of this report.

D. Cavitation and Static Pressure

Aside from lowering efficiency and causing pitting of the impeller blades, cavitation of the pumping unit would raise the noise level of the test section. Testing of sonic gear in the test section and use of sonic methods in observing cavitation on a test body make it desirable to maintain a low background noise level. It is of great importance, therefore, that the pump be free from all major cavitation and, as far as possible, free from minor cavitation.

In pump design, the cavitation index, σ, is conventionally defined as

$$\sigma = \frac{\frac{p_i - p_{vp}}{w}}{H}$$

where p_i is the absolute static pressure at the centerline of the pump intake (psf),

p_{vp} is the vapor pressure of the liquid (psf),

w is the specific weight of liquid (lb per cu ft), and

H is the head added by the pump.

Minimum values of p_i will occur for a hypothetical operating condition with vapor pressure at the crown of the downstream end of the contraction. The static pressure at the discharge side of the pump can be computed from Bernoulli's equation modified to account for the head lost between the downstream end of the contraction and the pump discharge,

$$\frac{V_o^2}{2g} + \frac{p_o}{w} + Z_o = \alpha_d \frac{\bar{V}_d^2}{2g} + \frac{p_d}{w} + Z_d - h_\ell$$

where the subscript o refers to the downstream end of the contraction and the subscript d refers to the discharge side of the pump. Substitution of the following values:

$$p_o = p_{vp}$$

$$Z_o - Z_d = 20 \text{ ft}$$

$$\alpha_d = 1.35 \text{ (assumed)}$$

$$V_d = V_o/4$$

$$h_f = 0.0544\ V_o^2/2g \text{ (Table XI)}$$

yields

$$\frac{p_d - p_o}{w} = 0.97 \frac{V_o^2}{2g} + 20 = \frac{p_d - p_{vp}}{w} \tag{1}$$

The static pressure upstream of the pump will be less than that downstream of the pump by the amount of head added to the flow. Thus,

$$\sigma = \frac{0.97 \frac{V_o^2}{2g} - \Sigma k \frac{V_o^2}{2g} + 20}{\Sigma k \frac{V_o^2}{2g}}$$

where Σk is the sum of the head loss coefficients in the tunnel circuit. Assuming that the largest value of Σk will be 0.24, the minimum value of σ will be

$$\sigma = 3.04 + \frac{20}{\Sigma k \frac{V_o^2}{2g}}$$

The smallest value of σ will occur at high test section velocities, and σ will be equal to 4.10 at a test section velocity of 71.5 fps. This minimum value has been computed for more severe conditions of tunnel operation than will probably ever exist, and yet the value is considered high enough to provide the pump with adequate protection against cavitation. The critical values of σ for propeller pumps usually vary from about 1.0 to 1.5 [24] and computations show that the critical value for this particular pump will be $\sigma_{cr} = 0.92$ [1].

The pump imposes another limiting condition on operation of the tunnel in that the pressure in the pump casing must not exceed a safe value.

Quoting from reference [1], "The Worthington Pump and Machinery Corporation stated that the existing pump withstood an internal pressure of 64.7 psia, but recommended that the working pressure be limited to 44.7 psia." Referring to Eq. (1), it will be seen that the pressure at the discharge side of the pump is a function of both the test section velocity and test section pressure. Setting p_d/w equal to 103.3 ft abs (44.7 psia) one obtains

$$\frac{p_o}{w} = 83.3 - 0.97 \frac{V_o^2}{2g}$$

as the maximum allowable absolute pressure at the axis of the test section. This equation is plotted in Fig. 62 and it is apparent that the allowable pressure falls to quite low values at high test section velocities. However, it is entirely possible that pump pressures could exceed the recommended safe limit without causing structural failure of the casing; this would be in part dependent upon the stress in the pump casing caused by the weight of the structure.

E. Temperature of the Tunnel

Because all of the power input to the pump and dynamometers is eventually converted to heat in the tunnel, the temperature of the water will rise during a period of operation. This temperature rise will be dependent upon three factors: the heat-storing capacity of the tunnel and the water it contains, the power input to the tunnel, and the amount of heat lost from the tunnel. The first two of these factors can be quite easily and accurately determined. However, the heat loss from the tunnel is dependent upon many factors: the tunnel wall thickness, area, finish and material, and the motion and temperature of the air around the tunnel.

A theoretical basis for determining the time-temperature curve is available from the consideration that all of the power input to the tunnel is used to raise the temperature of the tunnel or is transferred to the surrounding air. For practical purposes, the amount of heat transferred by conduction, convection, and radiation can be computed from

$$Q' = UA\ (T - T_o)$$

where Q' is the rate of heat transfer (Btu/hr),

A is the area of transfer (sq ft),

T is the temperature of water tunnel (^oF abs),

T_o is the room temperature (^oF abs), and

U is the overall coefficient of heat transmission (Btu/hr/sq ft/^oF).

The value of U is dependent upon both the thermal conductance of and radiation from the tunnel walls and the thermal conductance and convection of the air film outside the tunnel. It can be computed from

$$\frac{1}{U} = \frac{\ell}{K} + \frac{1}{f_o}$$

where ℓ is the tunnel wall thickness (in.),

K is the thermal conductivity for tunnel wall material (Btu/hr/sq ft/^oF/in.), and

f_o is the thermal conductance of the air film (Btu/hr/sq ft/^oF).

The magnitude of f_o is dependent upon the velocity of the air and the radiation from the surface. Standard values range from 2.0 for zero air velocity to 8.0 for air velocity of 25 fps [25] for a semismooth surface such as that of painted steel. An average value of K for steel is 300. Substituting f_o = 2.9 and ℓ = 3/16 in.,

$$U = 2.89 \text{ Btu/hr/sq ft/}^oF$$

Substituting f_o = 2.9 and ℓ = 1 in.,

$$U = 2.87 \text{ Btu/hr/sq ft/}^oF$$

It is seen that the heat transfer from the tunnel to the surrounding air is relatively unaffected by the thickness of the tunnel wall. Therefore, a value of U obtained from a model test should be applicable to the prototype if the prototype is built of steel and is exposed to air at room temperature. The value of U obtained in a model test should be greater than 2.0 since there was some circulation of air by the heating fans in the room in which the model was located.

Based on the consideration that all of the power input to the pump is converted into heat which raises the temperature of the system or is transferred to the surrounding air (which is assumed to remain at a constant temperature), the following differential equation can be written:

$$Q = \frac{dq}{dt} + UA\,(T - T_o) \qquad (2)$$

where Q is the rate of input of heat (Btu/hr), (1 hp = 2546.2 Btu/hr),
q is the absolute heat content of the tunnel (Btu), and
t is the time in hours from start of run.

By definition, q/W = T, where W is the equivalent heat capacity of the water tunnel and the water in it in pounds of water. Thus,

$$\frac{dq}{dt} = W \frac{dT}{dt} \tag{3}$$

Substituting Eq. (3) in Eq. (2) and integrating, assuming that $T = T_o$ when $t = 0$, gives

$$T - T_o = \frac{Q}{UA} \left(1 - e^{-\frac{UAt}{W}} \right) \tag{4}$$

which defines the time-temperature curve of the tunnel when the necessary values are substituted. This equation is plotted in Fig. 63 by substituting the constants given below:

$$U = 2.90 \text{ Btu/hr/sq ft/}^{o}\text{F}$$
$$A = 1858 \text{ sq ft}$$
$$W = 148{,}000 \text{ lb of water}$$

Curves are plotted for five different horsepower inputs. The value of U equal to 2.90 was chosen as the best value to fit the experimental points obtained in tests of the model of the 60-in. water tunnel [7] and should be equally valid for the present model study. Also, since the value of U is not appreciably changed by a change in the thickness of the tunnel wall, the same value should apply to the prototype tunnel. In reality, the prototype heating curve is relatively insensitive to a change in U because only a small percentage of the heat input is conducted away from the tunnel.

The time-temperature relation for the tunnel cooling can be determined by setting Q = 0 in Eq. (2), letting t be the time in hours from the time the pump is shut down and T' be the temperature of the tunnel when the pump is shut down. Equation (4) then becomes

$$T - T_o = (T' - T_o) e^{-\frac{UAt}{W}}$$

This curve is plotted in Fig. 64 for the prototype tunnel using values listed previously.

The temperature variation of the prototype tunnel can be computed by using Figs. 63 and 64. As an example, let it be assumed that the tunnel is operating at a test section velocity of 35 knots with the open jet installed, and that the tunnel is at a room temperature of 72° F at the start of the run. If the torque dynamometer is not being operated, the power input to the tunnel will be 400 hp. At the end of an 8-hr period of operation, the temperature will be 119° F ($T - T_o = 47°$ F) and, if the tunnel is allowed to cool for 16 hours, the final temperature will be 99° F ($T' - T_o = 47°$ F, $T - T_o = 27°$ F). Intermediate curves may be computed for any other horsepower input, but only one cooling curve can be drawn. These curves can, of course, be used if the pump is started while the temperature of the tunnel is above room temperature. It is only necessary to shift the abscissa scale so that zero hours corresponds to the temperature of the tunnel at the start of a run. In using the tunnel cooling curve, the abscissa scale must be shifted so that zero hours corresponds to $T' - T_o$ measured on the ordinate scale.

If the tunnel is used for endurance tests or if the testing of models will require extended periods of operation at high speeds, the temperature rise will be quite severe. This may well be a limiting factor in operation of the tunnel. However, the installation of a cooling system to circulate cooling water through a jacket or through the hollow guide vanes could maintain the tunnel at any desired temperature, depending upon the size of the cooling apparatus. The cooling system would, of course, increase the cost of the tunnel installation, but it would make possible a wider range of testing procedures.

F. Conclusions

On the basis of these experimental and analytical studies of the pump it is concluded that:

1. The maximum test section velocity with power input of 400 hp will be 35 knots with the open-jet test section and 37.5 knots with the closed-jet test section.

2. The stilling length between the pump and the contraction will be sufficient to damp out maldistribution of outflow from the pump before returning the flow to the test section.

3. The minimum cavitation index at the pump will be $\sigma_{min} = 4.10$, which will be high enough to protect the pump from cavitation.

4. There will be a 50° temperature rise if the tunnel is operated continuously for 8 hours at maximum power input.

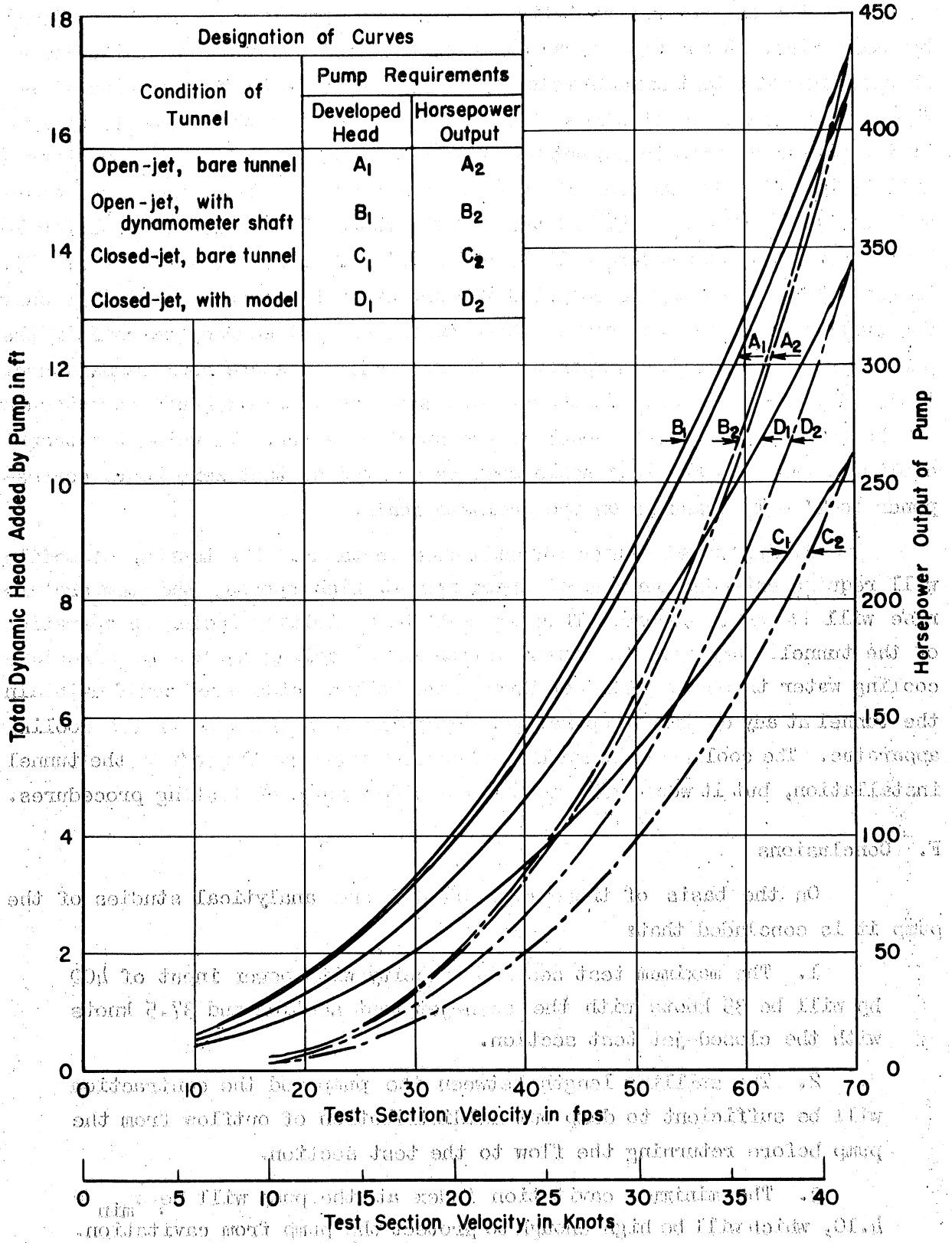

Fig. 60 - Head-Discharge Curves for Prototype Water Tunnel

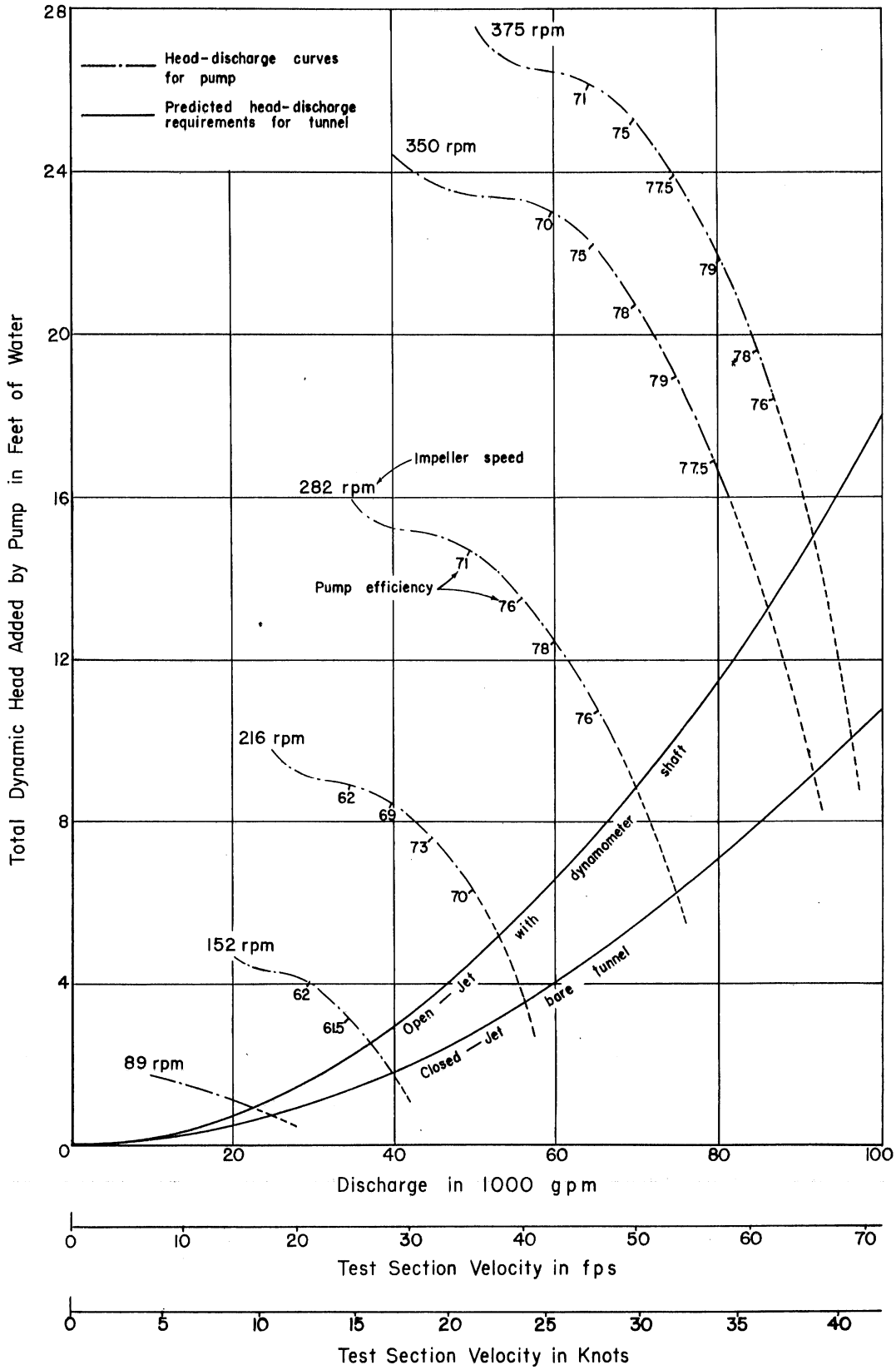

Fig. 61 - Pump Rating Curves and Head-Discharge Curves of Prototype Tunnel

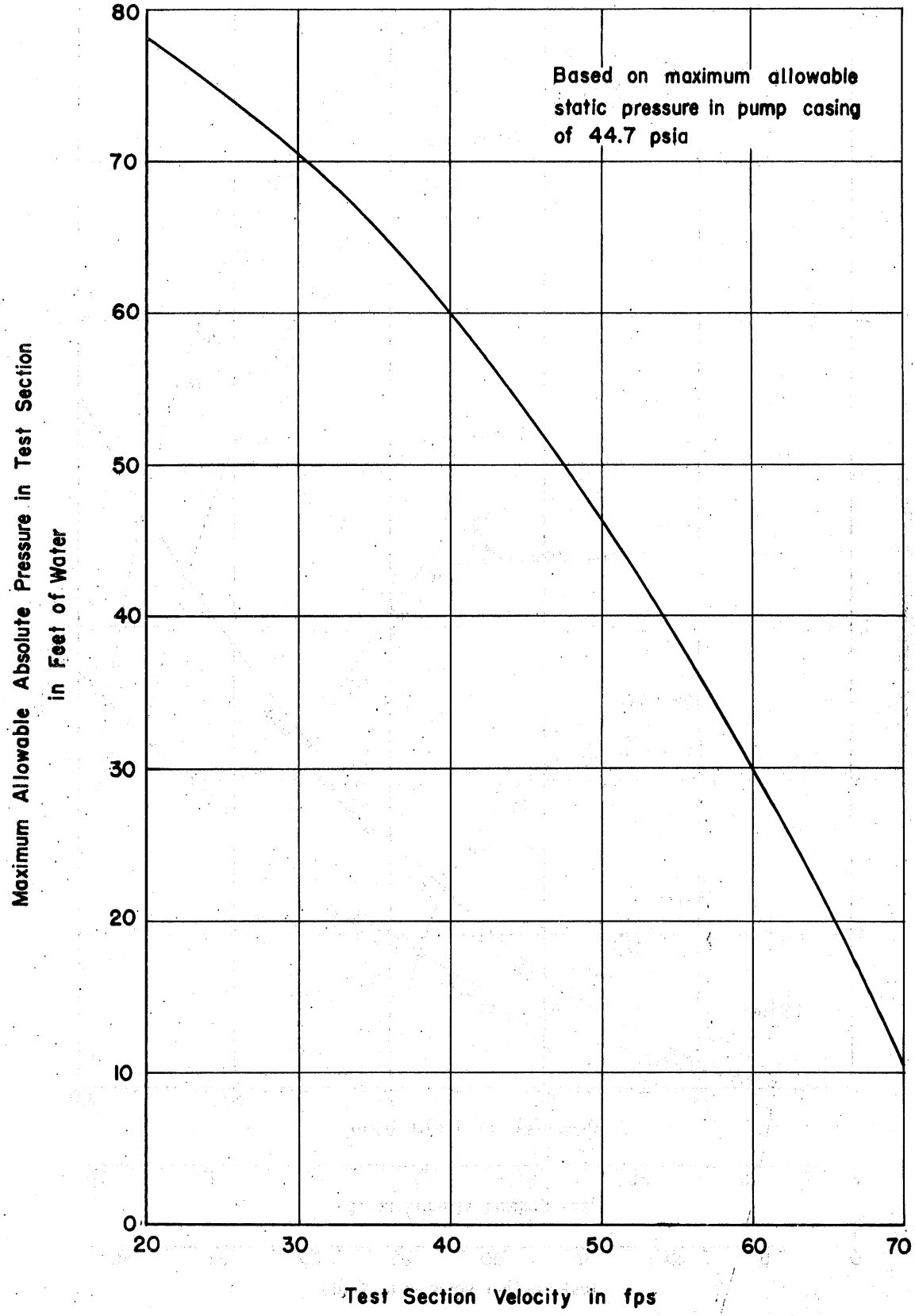

Fig. 62 - Maximum Allowable Pressure in Prototype Test Section As Limited by Pump Casing

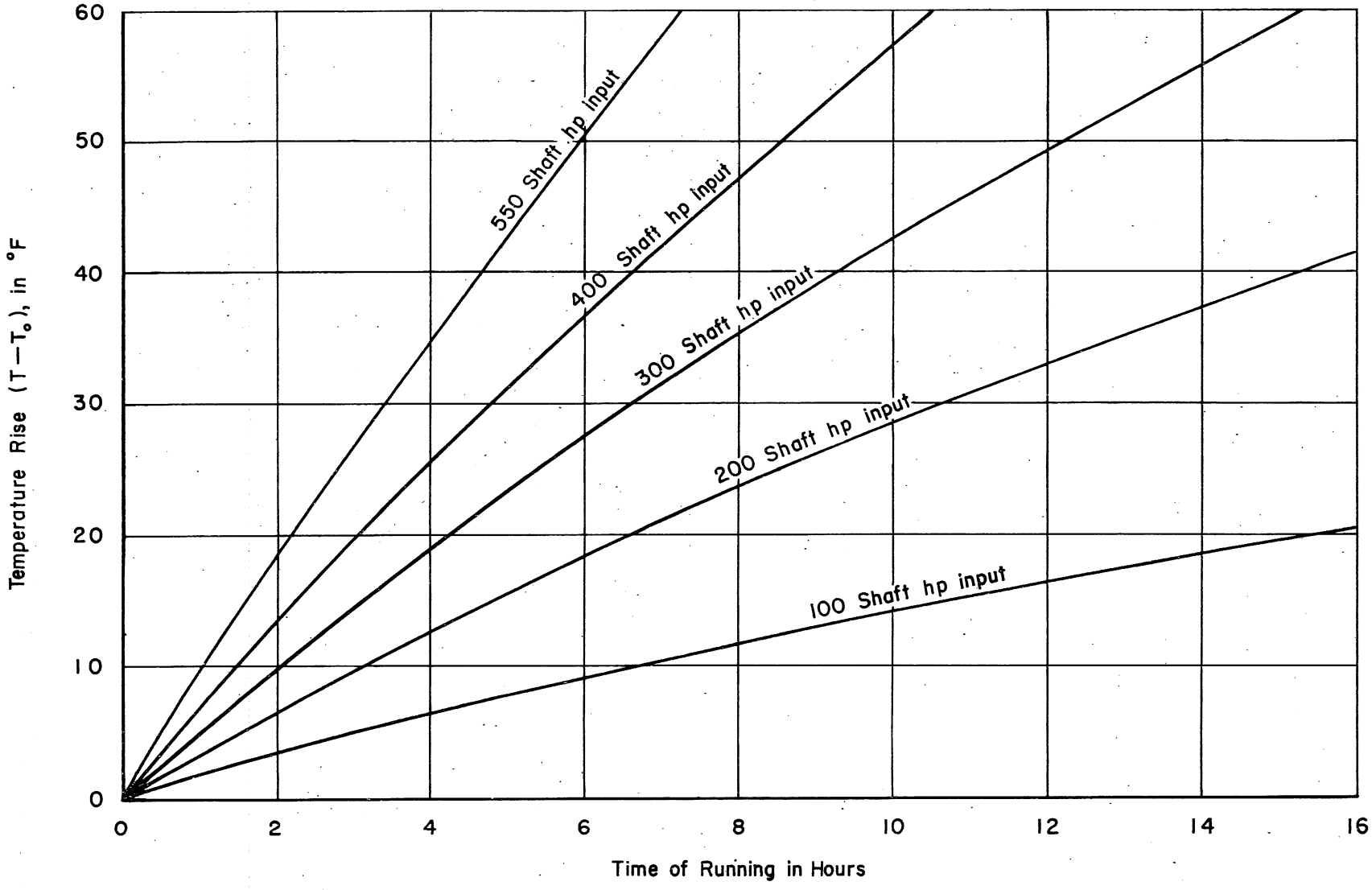

Fig. 63 - Temperature Rise of Prototype Tunnel during Operation

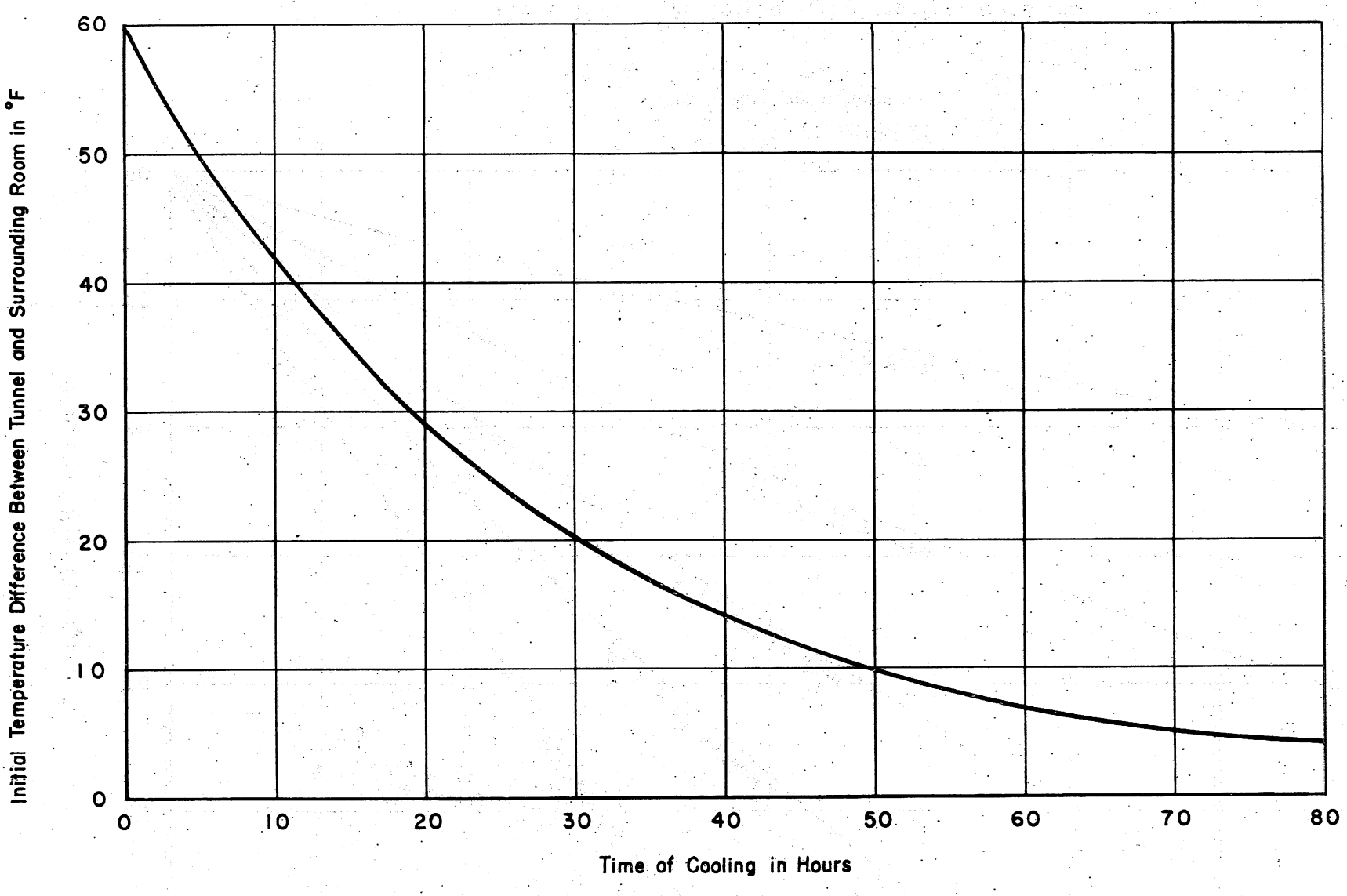

Fig. 64 - Decrease in Temperature during Cooling of Prototype Tunnel

APPENDIX

USE OF THE RELAXATION METHOD IN DETERMINING THE PRESSURE DISTRIBUTION IN THE CLOSED-JET DIFFUSER TRANSITION

The equation of continuity for axially symmetric, steady, incompressible flow is

$$\frac{1}{r}\frac{\delta(rv)}{\delta r} + \frac{\delta u}{\delta x} = 0$$

where x and r are coordinates parallel and perpendicular respectively to the axis of symmetry, and u and v are flow velocities in these directions. By virtue of this equation, a stream function Ψ can be introduced such that

$$u = \frac{1}{r}\frac{\delta \Psi}{\delta r}, \quad v = \frac{-1}{r}\frac{\delta \Psi}{\delta x} \tag{1}$$

If the flow is irrotational at all points,

$$\frac{\delta u}{\delta r} - \frac{\delta v}{\delta x} = 0 \tag{2}$$

and substituting Eq. (1) in Eq. (2) gives

$$\frac{\delta^2 \Psi}{\delta x^2} + \frac{\delta^2 \Psi}{\delta r^2} - \frac{1}{r}\frac{\delta \Psi}{\delta r} = 0 \tag{3}$$

as the equation governing the stream function, and thereby defining the flow at all points once the conditions at the boundaries of the fluid have been specified.

The boundaries of the flow field under consideration consist of a cylindrical section of circular conduit joined to a conical section having a half angle of divergence of 3° 20' by a parabolic transition 1 radius long. This boundary is shown in Fig. 65b; the diagram also defines the center and positive directions of the coordinate system of Eq. (3). Since the flow has axial symmetry, $\Psi = 0$ at $r = 0$, and since there can be no velocity normal to the solid boundaries, Ψ must assume a constant value, Ψ_o, along the boundary. Far upstream of the transition, the velocity must be uniform at all points and parallel to the axis of symmetry, so that $\Psi = 1/2\ V_o r^2$, where V_o is this

uniform velocity and thus has the same significance as it had throughout the main body of this report. The value of Ψ on the solid boundary is thus determined as $\Psi_o = 1/2\ V_o R^2$, where $\underline{R}$ is the radius of the cylindrical conduit (or the radius of the test section). Far downstream of the transition, the velocity distribution in the diffuser will approach the distribution in a spherical segment of source flow, the source being located at the (hypothetical) apex of the diffuser cone. The strength of the source is determined by the consideration that $\Psi = \Psi_o$ on the boundary of the diffuser.

A simple transformation of variables,

$$x = \xi R,\ r = \eta R,\ \Psi = \psi \Psi_o$$

eliminates dimensional considerations from the solution of the governing equations since ξ, η, and ψ are pure numbers. Equation (3) is then transformed to

$$\frac{\delta^2 \psi}{\delta \xi^2} + \frac{\delta^2 \psi}{\delta \eta^2} - \frac{1}{\eta} \frac{\delta \psi}{\delta \eta} = 0 \tag{4}$$

and Eqs. 1 become

$$u = \frac{\psi_o}{R^2 \eta} \frac{\delta \psi}{\delta \eta}$$

$$v = \frac{-\psi_o}{R^2 \eta} \frac{\delta \psi}{\delta \xi}$$

so that

$$\frac{u}{V_o} = \frac{1}{2\eta} \frac{\delta \psi}{\delta \eta} \tag{5}$$

$$\frac{v}{V_o} = -\frac{1}{2\eta} \frac{\delta \psi}{\delta \xi} \tag{6}$$

The conventional method of determining ψ as a function of η and ξ would be to hypothesize a suitable distribution of sources and sinks such that Eq. (4) would be satisfied at all points and the boundary conditions would

be satisfied (at least approximately). The resulting analytical expression for ψ would then determine the pressure and velocity at any point in the flow system. However, no analytical method exists at present for determining the expression for ψ except for very special shapes of boundaries. Of the graphical and other approximate methods available, one developed in the past decade by R. V. Southwell and his collaborators has been chosen. By this method, the value of ψ can be determined to any desired degree of accuracy at a finite number of points in a flow field. The method, called the relaxation method, consists of superimposing a regular network on the plane of the flow field (a plane containing the axis of symmetry in this case) and satisfying to any desired accuracy a finite difference approximation to Eq. (4) at each node of the net. Considering a typical section of a square net with mesh length $\underline{a}$ (Fig. 65c), it can be seen that (approximately),

$$\left(\frac{\delta\psi}{\delta\eta}\right)_o = \frac{\psi_1 - \psi_3}{2a}$$

$$\left(\frac{\delta^2\psi}{\delta\eta^2}\right)_o = \frac{\frac{\psi_1 - \psi_o}{a} - \frac{\psi_o - \psi_3}{a}}{a}$$

$$\left(\frac{\delta^2\psi}{\delta\xi^2}\right)_o = \frac{\frac{\psi_2 - \psi_o}{a} - \frac{\psi_o - \psi_4}{a}}{a}$$

Substituting these values in Eq. (4) yields

$$\left(1 - \frac{a}{2\eta}\right)\psi_1 + \psi_2 + \left(1 + \frac{a}{2\eta}\right)\psi_3 + \psi_4 - 4\psi_o = 0 \qquad (7)$$

as a finite difference approximation to Eq. (4). This equation must be satisfied at every node of a net which has four arms of equal length.

The demonstration given above is a simple method of deriving the finite difference approximation, but it gives no indication of the order of the error involved in making the approximation. If ψ is expanded in a Taylor's series of two variables, ξ and η, Eq. (7) will result if all terms of order

a^3 or higher are suppressed. This expansion is also useful when one arm of the net, such as (0,1), has a length $c \cdot a$, ($c < 1$), a circumstance which arises for nodes near the boundary (Fig. 65d). The finite difference equation then becomes

$$\left(\frac{2}{(1+c)c} - \frac{a}{\eta}\frac{1}{(1+c)c}\right)\psi_1 + \psi_2 + \left(\frac{2}{c+1} + \frac{a}{\eta(1+c)}\right)\psi_3 + \psi_4$$

$$-\left(\frac{2}{c} + 2 - \frac{a(1-c)}{\eta c}\right)\psi_o = 0 \qquad (8)$$

The first step in the relaxation process is to determine the values of ψ around the edges of the net so that the boundary conditions are satisfied, at least approximately; these values are not changed in the course of the computation. In this problem, in order to confine the computations to a finite area, the dimensionless velocity distributions which theoretically exist when $\underline{x}$ approaches minus or plus infinity were assumed to exist exactly at $x = -2.0$ R and approximately at $x = +3.0$ R. It is not believed that significant errors were introduced into the analysis by making these assumptions.

The boundary conditions become $\psi = 0$ at $\eta = 0$, $\psi = 1$ at the conduit boundary and $\psi = \eta^2$ at $\xi = -2.0$. The distribution of ψ at $\xi = +3.0$ can be expressed analytically but is not presented here because it is of a special nature; that is, it depends on the design of the transition and the angle of divergence of the diffuser walls. This distribution can be easily computed, however, once the boundary shape has been specified.

Plausible values of ψ are next assigned at each interior node of the net; these values are then substituted in Eq. (7) or (8) and the residual at each node is computed. The residual is the amount that the left side of Eq. (7) or (8) differs from zero, and is denoted by $\underline{F}$. Considering only nodes for which Eq. (7) is applicable, the residual at any node can be reduced to zero by increasing the value of ψ assigned to that node (ψ_o) by $+F/4$. However, this change in ψ at node 0 affects the residuals at surrounding nodes 1, 2, 3, and 4 by the following respective amounts:

$$+\left(1 + \frac{a}{2\eta}\right)\frac{F}{4}, \quad +\frac{F}{4}, \quad +\left(1 - \frac{a}{2\eta}\right)\frac{F}{4}, \quad +\frac{F}{4}$$

since ψ_o for one segment of the net is ψ_1, ψ_2, ψ_3, or ψ_4 for adjacent segments. The residuals at each node are thus constantly being changed, but the process is convergent so that finally a distribution of ψ is reached whereby the residuals are as small as desired. In actually relaxing the net, certain computational procedures were used which hasten the convergence or simplify the arithmetic, so that the procedure outlined above for liquidating the residuals was not followed exactly. However, the results are the same, and the relaxation process was continued until a change of 0.00001 would increase the value of the residuals or until all residuals were ± 0.00002 or smaller. This high order of accuracy was necessary in order to obtain significant variations in wall pressure. The accepted values of ψ (multiplied by 10^5) are shown in Fig. 65a.

Using the finite difference approximations to Eqs. (5) and (6)

$$\frac{u}{V_o} = \frac{1}{2\eta}\left(\frac{\psi_1 - \psi_3}{2a}\right) \tag{9}$$

and

$$\frac{v}{V_o} = \frac{1}{2\eta}\left(\frac{\psi_2 - \psi_4}{2a}\right) \tag{10}$$

velocity components were computed at each node where Eqs. (9) and (10) could be applied. The resulting velocity distribution (Figs. 41 and 42) were then extrapolated to give the velocity distribution at the wall and the pressure distribution along the wall was computed from Bernoulli's equation

$$\frac{\frac{p_o - p}{w}}{\frac{V_o^2}{2g}} = \frac{u^2}{V_o^2} + \frac{v^2}{V_o^2} - 1 \tag{11}$$

where p_o is the pressure at $\xi = -2.0$. The resulting pressure distribution at the wall of the conduit is plotted as a long-dashed line in Fig. 43 of Part IV of this report. This pressure distribution can be considered to be the absolute pressure distribution of a weightless fluid or the piezometric pressure distribution of a fluid having weight, which accounts for the omission of the elevation term in Eq. (11). It is not necessary to compute the pressure

distribution in the interior of the fluid because a theorem of hydrodynamics states that the point of minimum pressure will be somewhere on the boundary of the fluid.

The same relaxation process must be started anew if it is desired to determine the pressure distribution for another design of the diffuser transition. The method requires a great deal of computation to obtain good accuracy and consequently is not very promising as a design method in this particular case. It is possible, however, that the computations could be completed in a fraction of the time necessary for computations by the conventional relaxation method if a suitable analogue or digital computer were available. Using Eqs. (7) and (8), $\underline{n}$ simultaneous linear equations could be written, each containing five or fewer unknown values of ψ. Solution of this set of equations would result in values of ψ at each node of the net, and if the values could be obtained with sufficient accuracy, the relaxation process would not have to be applied. If the accuracy of the computer were not sufficient, higher accuracy could be obtained by applying the relaxation method to the ψ-values given by the computer. The number of variables which the computer could handle would limit the number of nodes, $\underline{n}$, and thus limit the fineness of the net and the accuracy of the result. Values of ψ could be computed on a finer net by using the relaxation method, starting with the values of ψ determined on the larger net with the computer.

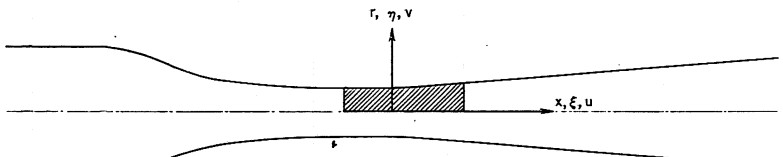

(b) Definition Sketch of Network Coordinate Area

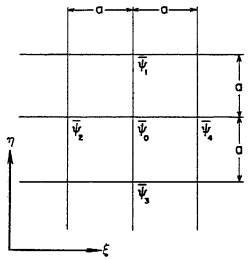

(c) Typical Region of Net at Interior

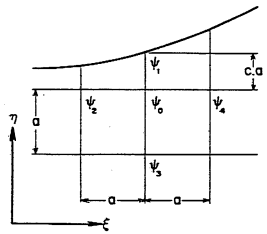

(d) Typical Region near Net Boundary

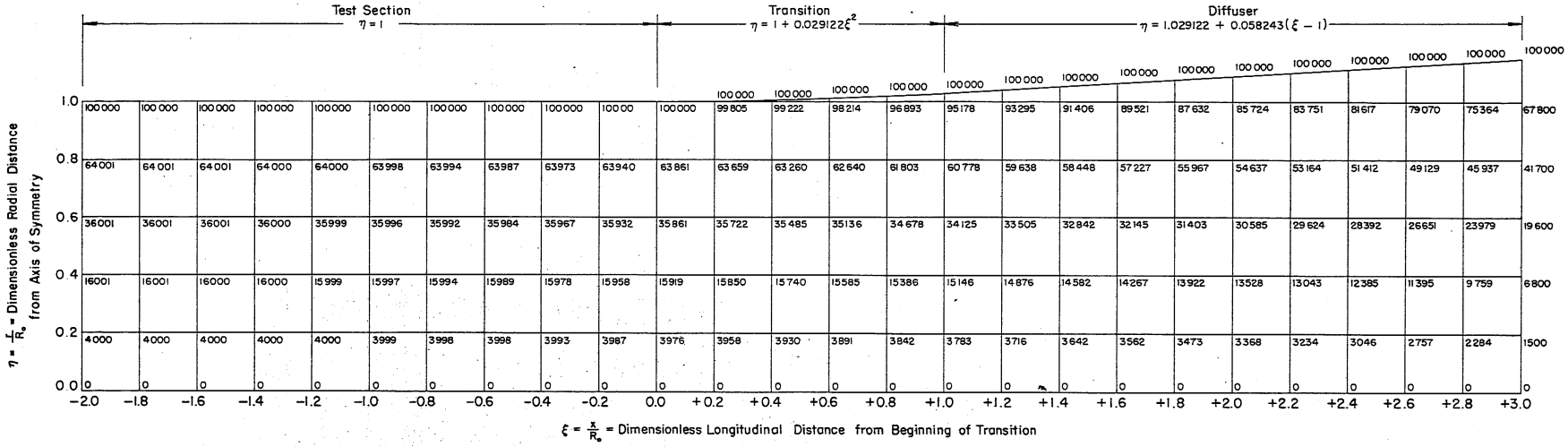

(a) Relaxation Network

Fig. 65 - Values of ψ in the Region of the Diffuser Transition as Determined by the Relaxation Method

TABLE I

TUNNEL FORMS DURING MODEL TESTS

Tunnel Form	Test Section	Main Diffuser Angle	Throat Diameter of Pick-Up Cone	Dynamometer Shaft
A	Open	6° 40'	6 5/8 in.	None
B	Open	6° 40'	6 5/8 in.	Contraction dynamometer shaft. (Shaft diameter = 1.125 in. at vaned elbow IV)
C	Closed	6° 40'		None
D	Open	9°	6 5/8 in.	None
E	Open	6° 40'	6 3/8 in.	None
F	Open	6° 40'	6 3/8 in.	Diffuser dynamometer shaft, two-strut supports.
G	Open	6° 40'	6 3/8 in.	Diffuser dynamometer shaft, three-strut supports.
H	Open	6° 40'	6 5/8 in.	Contraction dynamometer shaft. (Shaft diameter = 2.437 in. at vaned elbow IV)
I	Open	6° 40'	6 3/8 in.	None. Unstreamlined shaft sleeve in vaned elbow IV.
J	Open	6° 40'	6 3/8 in.	None. Streamlined shaft sleeve in vaned elbow IV.

TABLE II

DIMENSIONS OF THE MODEL CONTRACTION DYNAMOMETER SHAFT

x^* (in.)	Shaft Diam (in.)	x^* (in.)	Shaft Diam (in.)
+ 0	2.274	- 0.0	2.274
+ 0.67	2.239	- 0.67	2.308
+ 2.00	2.145	- 2.00	2.358
+ 3.33	2.026	- 3.33	2.392
+ 4.67	1.897	- 4.67	2.408
+ 6.00	1.753	- 6.00	2.420
+ 7.33	1.615	- 7.33	2.429
+ 8.67	1.477	- 8.67	2.437
+10.00	1.359	-20.10	2.437
+11.33	1.249	-20.40	2.415
+12.67	1.158	-20.69	2.393
+14.00	1.086	-20.98	2.350
+15.33	1.020	-21.27	2.274
+16.67	0.965	-21.56	2.145
+18.00	0.923	-21.85	1.963
+19.33	0.891	-22.15	1.730
+20.67	0.867	-22.44	1.409
+22.00	0.850	-22.73	1.190
+23.33	0.837	-23.02	1.125
+24.67	0.828	-39.75	1.125
+26.00	0.821		
+27.33	0.817		
+28.67	0.814		
+30.00	0.812		

*$\underline{x}$ is the distance from the upstream edge of the contraction measured positive in the downstream direction.

TABLE III

DIAMETERS AND AREA RATIOS AT TRAVERSE STATIONS

Station	Conduit Diam (in.)	$(\frac{6.000}{\text{Diam}})^4$
5	11.565	0.07245
5*	11.565	0.07317
5**	11.976	0.06300
6	12.107	0.06032
7	13.20	0.04269
8***	13.20	0.04761
9+	13.75	0.04906
10	18.00	0.01235
11	18.00	0.01235
12	18.00	0.01235
12++	18.00	0.01281

*Area ratio corrected for presence of diffuser dynamometer shaft.

**With 9° diffuser installed.

***Area ratio corrected for presence of pump drive shaft.

+Area ratio corrected for presence of propeller hub fairing.

++Area ratio corrected for presence of contraction dynamometer shaft.

TABLE IV

PRESSURE DISTRIBUTION AT CONTRACTION BOUNDARY

x (in.)	Diam of Cone (in.)	Diam of Shaft (in.)	$\frac{p_{1.5} - p_x}{w} \Big/ \frac{\bar{V}_{1.5}^2}{2g}$									
			Calculated K-1		Open Jet Without Shaft			Open Jet With Shaft			Closed Jet Without Shaft		
			Without Shaft	With Shaft	$\bar{V}_o^*$=49.5	$\bar{V}_o$=30.0	$\bar{V}_o$=18.0	$\bar{V}_o$=47.9	$\bar{V}_o$=29.5	$\bar{V}_o$=17.75	$\bar{V}_o$=51.6	$\bar{V}_o$=29.8	$\bar{V}_o$=18.2
0.00	18.025	2.274	-0.027	-0.021									
1.50	17.902	2.180	0.000	0.000	0.000	0.000	0.000	0.000	0.000	0.000	0.000	0.000	0.000
3.00	17.467	2.056	0.103	0.099	0.071	0.099	0.000	0.0214	0.095	0.079	0.010	0.014	0.090
4.00	16.924	1.962	0.252	0.418	0.144	0.099	0.066	0.0811	0.048	0.000	0.056	0.057	0.129
5.00	16.133	1.861	0.516	0.517	0.302	0.262	0.236	0.0301	0.214	0.158	0.235	0.196	0.309
6.00	15.204	1.753	0.922	0.940	0.608	0.557	0.576	0.578	0.523	0.513	0.547	0.736	0.579
7.00	14.064	1.651	1.625	1.627	1.324	1.294	1.271	1.351	1.307	1.249	1.101	1.214	1.273
8.00	12.945	1.546	2.658	2.667	2.468	2.479	2.555	2.600	2.629	2.617	2.403	2.327	2.366
9.00	12.000	1.447	3.953	3.969	3.946	3.551	4.061	4.111	4.145	4.222	3.871	3.838	3.806
10.00	11.126	1.359	5.703	5.729	5.736	5.431	5.901	5.880	5.990	6.103	5.668	5.725	5.657
11.00	10.375	1.279	7.864	7.904	7.752	7.825	8.070	7.921	8.057	8.404	7.660	7.670	7.766
12.00	9.724	1.204	10.488	10.543	10.341	10.319	10.624	10.559	10.672	11.035	10.270	10.194	10.299
13.00	9.107	1.140	13.932	14.014	13.922	13.955	14.371	14.240	14.320	14.901	13.910	13.817	14.002
15.00	8.070	1.036	23.217	23.390	23.864	23.660	24.183	24.366	24.267	25.502	23.812	24.025	23.826
17.00	7.343	0.955	34.327	33.769	34.849	34.710	35.700	34.914	34.963	36.498	34.658	35.118	34.999
19.00	6.830	0.899	46.198	46.619	47.190	46.375	47.489	47.770	47.322	48.808	45.776	45.431	45.041
21.00	6.480	0.863	57.251	57.820	57.618	56.907	58.310	58.547	58.113	59.909	57.678	57.245	56.947
23.00	6.230	0.841	67.180	67.913	67.265	67.013	68.908	67.933	68.000	70.431	67.325	67.258	67.375
24.00	6.188	0.832	69.049	69.782									
25.00	6.127	0.826	71.881	72.658	70.567	70.035	71.135	70.891	71.124	73.653	72.172	71.841	71.811
27.00	6.027	0.818	76.839	77.708									
28.50	6.000	0.814	78.250	79.132	81.343	79.953	80.646	82.320	81.439	83.530	79.915	79.703	79.756
29.00	6.000		78.250										
30.00	6.000	0.812	78.250	79.118									

*$\bar{V}_o$ is the average velocity in feet per second in a section 6 inches in diameter.

TABLE V

CONTRACTION HEAD LOSS DATA

Run No.	Test Section Velocity fps	$\frac{p_{1.5} - p_{28.5}}{w}$ ft	$\frac{V_o^2}{2g}$ ft	$\frac{\frac{p_{1.5} - p_{28.5}}{w}}{\frac{V_o^2}{2g}}$	$\frac{h_\ell}{\frac{V_o^2}{2g}}$
1	9.539	1.47	1.4129	1.0404	0.0566
2	14.998	3.56	3.4929	1.0192	0.0354
3	19.695	6.10	6.0232	1.0127	0.0289
4	30.634	14.72	14.5720	1.0101	0.0263
5	25.692	10.33	10.2497	1.0078	0.0240
6	9.478	1.43	1.3949	1.0252	0.0414
7	14.989	3.59	3.4887	1.0290	0.0452
8	22.684	8.07	7.9901	1.0100	0.0262
9	26.249	10.75	10.6989	1.0048	0.0210
10	30.762	15.02	14.6941	1.0222	0.0384
11	35.371	19.72	19.4271	1.0151	0.0313
12	39.491	24.58	24.2114	1.0150	0.0312
13	47.411	34.96	34.9038	1.0016	0.0178
14	25.124	9.87	9.8015	1.0070	0.0232
15	29.888	14.00	13.8710	1.0093	0.0257
					0.0315

TABLE VI

FORM LOSS COEFFICIENTS FOR DIFFUSER I AND OPEN-JET TEST SECTION

Tunnel Format†	Pick-Up Cone Gap	α_5	$V_o \cong 18$ fps			$V_o \cong 30$ fps			$V_o \cong 48$ fps		
			$\frac{V_o^2}{2g}$ (in.)	$\frac{p_5 - p_{ref}}{w}$ (in.)	K_o	$\frac{V_o^2}{2g}$ (in.)	$\frac{p_5 - p_{ref}}{w}$ (in.)	K_o	$\frac{V_o^2}{2g}$ (in.)	$\frac{p_5 - p_{ref}}{w}$ (in.)	K_o
A	0	1.627	60.37	44.77	0.1227	167.70	123.09	0.1312	447.39	336.68	0.1134
A	5/8	1.563	60.37	44.62	0.1299	167.70	122.28	0.1391	434.70	319.05	0.1347
B	0	1.566	58.38	44.73	0.1403	161.39	122.33	0.1493	425.75	335.51	0.1200
B	5/8	1.502*	58.38	44.72	0.1451	162.16	124.82	0.1422	429.36	334.42	0.1338
C	--	1.411	61.31	50.43	0.0371	166.17	136.41	0.0386	497.89	409.35	0.0377
D	0	1.761	61.19	43.74	0.1470	166.64	118.72	0.1494	420.25	300.85	0.1459
D	5/8	1.878	61.37	43.69	0.1428	167.46	119.26	0.1425	416.49	294.33	0.1593
E	0	1.655	60.72	43.71	0.1397	167.46	120.78	0.1393	424.48	315.38	0.1184
E	5/8	1.657	61.07	44.32	0.1338	167.58	120.07	0.1441	423.89	303.21	0.1463
F	0	1.503	61.07	45.18	0.1291	167.11	121.63	0.1421	426.36	310.70	0.1423
F	5/8	1.543	60.72	43.40	0.1515	167.23	120.89	0.1447	423.89	309.64	0.1380
G	0	1.606	69.05	50.64	0.1279	167.93	121.17	0.1410	425.54	309.26	0.1367
G	5/8	1.605	61.07	43.83	0.1436	167.81	120.63	0.1436	423.89	311.38	0.1289

†Table I gives description of tunnel circuit during run.

*Estimated.

TABLE VII

FORM LOSS COEFFICIENTS FOR DIFFUSERS II AND III

Tunnel Form†	Pick-Up Cone Gap	α_6	α_7	DIFFUSER II								
				$V_o \cong 18$ fps			$V_o \cong 30$ fps			$V_o \cong 48$ fps		
				$\frac{V_o^2}{2g}$ (in.)	$\frac{p_7 - p_6}{w}$ (in.)	K_o	$\frac{V_o^2}{2g}$ (in.)	$\frac{p_7 - p_6}{w}$ (in.)	K_o	$\frac{V_o^2}{2g}$ (in.)	$\frac{p_7 - p_6}{w}$ (in.)	K_o
A	0	1.334	1.223	60.37	0.74	0.0145	167.70	2.05	0.0146	447.39	6.03	0.0133
A	5/8	1.303	1.223*	60.37	0.72	0.0130	167.70	2.56	0.0097	434.70	6.00	0.0111
B	0	1.338	1.223*	58.38	0.69	0.0151	161.39	2.22	0.0133	425.75	5.75	0.0135
B	5/8	1.303*	1.223*	58.38	0.69	0.0130	162.16	2.33	0.0105	429.36	5.70	0.0116
C	--	1.212	1.215	61.31	0.75	0.0075	166.17	2.21	0.0065	497.89	6.61	0.0065
D	0	1.234	1.226	61.19	0.77	0.0080	166.64	1.95	0.0090	420.25	5.48	0.0076
D	5/8	1.234*	1.226*	61.37	0.77	0.0081	167.46	2.15	0.0078	416.49	5.22	0.0081
E	0	1.215	1.223*	60.72	0.73	0.0135	167.46	2.47	0.0108	424.48	6.71	0.0097
E	5/8	1.215*	1.223*	61.07	0.89	0.0109	167.58	2.40	0.0112	423.89	6.62	0.0099
F	0	1.229	1.223*	61.07	0.72	0.0086	167.11	2.23	0.0081	426.36	6.01	0.0063
F	5/8	1.344	1.223*	60.72	0.70	0.0158	167.23	2.78	0.0108	423.89	5.93	0.0134
G	0	1.261	1.223*	69.05	0.97	0.0083	167.93	2.25	0.0090	430.12	6.01	0.0084
G	5/8	1.246	1.223*	61.07	0.78	0.0087	167.81	2.29	0.0078	423.89	5.99	0.0073
				DIFFUSER III								
		α_9	α_{10}		$\frac{p_{10} - p_9}{w}$			$\frac{p_{10} - p_9}{w}$			$\frac{p_{10} - p_9}{w}$	
A	0	1.35*	1.12*	60.37	1.62	0.0237	167.70	5.31	0.0188	447.39	14.51	0.0181
A	5/8	1.35*	1.12*	60.37	1.97	0.0179	167.70	5.36	0.0185	434.70	13.77	0.0188
B	0	1.35*	1.12*	58.38	1.78	0.0200	161.39	5.16	0.0185	425.75	15.14	0.0149
B	5/8	1.35*	1.12*	58.38	2.00	0.0162	162.16	5.07	0.0192	429.36	13.49	0.0191
C	--	1.35*	1.12*	61.31	1.93	0.0190	166.17	5.25	0.0189	497.89	15.36	0.0196

†Table I gives description of tunnel circuit during run.

*Estimated.

TABLE VIII

FORM LOSS COEFFICIENTS FOR VANED ELBOW II

Tunnel Form†	Pick-Up Cone Gap	a_5	a_6	$V_o \cong 18$ fps			$V_o \cong 30$ fps			$V_o \cong 48$ fps		
				$\frac{V_o^2}{2g}$ (in.)	$\frac{p_5 - p_6}{w}$ (in.)	ξ	$\frac{V_o^2}{2g}$ (in.)	$\frac{p_5 - p_6}{w}$ (in.)	ξ	$\frac{V_o^2}{2g}$ (in.)	$\frac{p_5 - p_6}{w}$ (in.)	ξ
A	0	1.627	1.334	60.37	-0.85	0.272	167.70	-2.59	0.255	447.39	-6.67	0.263
A	5/8	1.563	1.303	60.37	-0.59	0.294	167.70	-2.71	0.207	434.70	-7.20	0.202
B	0	1.566	1.338	58.38	-0.85	0.203	161.39	-2.30	0.209	425.75	-5.82	0.217
B	5/8	1.502*	1.307*	58.38	-1.07	0.115	162.16	-1.77	0.219	429.36	-7.05	0.143
C	--	1.411	1.212	61.31	-0.62	0.212	166.17	-1.80	0.204	497.89	-5.38	0.205
D	0	1.761	1.234	61.19	-1.04	0.257	167.70	-3.10	0.235	420.25	-8.68	0.201
D	5/8	1.878	1.234*	61.37	-1.19	0.336	167.46	-4.07	0.249	416.49	-10.06	0.263
E	0	1.655	1.315	60.72	-1.04	0.274	167.46	-2.56	0.298	424.48	-6.18	0.311
E	5/8	1.657	1.315	61.07	-0.86	0.315	167.58	-2.45	0.310	423.89	-6.71	0.293
F	0	1.503	1.229	61.07	-0.81	0.254	167.11	-2.53	0.234	426.36	-6.45	0.135
F	5/8	1.543	1.344	60.72	-0.90	0.182	167.23	-2.78	0.159	423.89	-6.98	0.162
G	0	1.606	1.261	69.05	-1.00	0.318	167.93	-2.53	0.211	430.12	-7.11	0.192
G	5/8	1.605	1.246	61.07	-1.06	0.292	167.81	-2.77	0.205	423.89	-7.01	0.305

†Table 1 gives description of tunnel circuit during runs.

*Estimated.

TABLE IX

FORM LOSS COEFFICIENTS FOR VANED ELBOW II

Tunnel Form†	Pick-Up Cone Gap	α_7	α_g	$V_o \cong 18$ fps			$V_o \cong 30$ fps			$V_o \cong 48$ fps		
				$\frac{V_o^2}{2g}$ (in.)	$\frac{p_7 - p_g}{w}$ (in.)	ξ	$\frac{V_o^2}{2g}$ (in.)	$\frac{p_7 - p_g}{w}$ (in.)	ξ	$\frac{V_o^2}{2g}$ (in.)	$\frac{p_7 - p_g}{w}$ (in.)	ξ
A	0	1.223	1.110	60.37	1.00	0.341	167.70	3.64	0.463	447.39	9.01	0.527
A	5/8	1.223*	1.110*	60.37	1.42	0.504	167.70	3.76	0.480	434.70	8.81	0.430
B	0	1.223*	1.110*	58.38	1.69	0.632	161.39	4.29	0.578	425.75	10.25	0.520
B	5/8	1.223*	1.110*	58.38	1.56	0.579	162.16	4.04	0.538	429.36	10.08	0.506
C	--	1.215	1.110*	61.31	1.49	0.514	166.17	3.68	0.466	497.89	10.35	0.435
D	0	1.226	1.110*	61.19	1.54	0.546	167.70	3.07	0.387	420.25	9.59	0.493
D	5/8	1.226*	1.110*	61.37	1.80	0.643	167.46	3.69	0.474	416.49	9.14	0.473
E	0	1.223*	1.110*	60.72	1.70	0.610	167.46	3.78	0.484	424.48	8.97	0.451
E	5/8	1.223*	1.110*	61.07	1.43	0.501	167.58	3.59	0.457	423.89	8.82	0.543
F	0	1.223*	1.110*	61.07	1.05	0.348	167.11	3.73	0.470	426.36	9.22	0.454
F	5/8	1.223*	1.110*	60.72	1.38	0.478	167.23	3.70	0.465	423.89	8.84	0.436
G	0	1.223*	1.110*	69.05	1.65	0.513	167.93	3.66	0.465	430.12	8.99	0.545
G	5/8	1.223*	1.110*	61.07	1.45	0.510	167.81	3.66	0.466	423.89	8.75	0.439

†Table I gives description of tunnel circuit during runs.

*Estimated.

TABLE X

FORM LOSS COEFFICIENTS FOR VANED ELBOWS III AND IV

Tunnel Form†	Pick-Up Cone Gap	α_{10}	α_{12}	VANED ELBOWS III AND IV								
				$V_o \cong$ 18 fps			$V_o \cong$ 30 fps			$V_o \cong$ 48 fps		
				$\frac{V_o^2}{2g}$ (in.)	$\frac{p_{10} - p_{12}}{w}$ (in.)	2ζ	$\frac{V_o^2}{2g}$ (in.)	$\frac{p_{10} - p_{12}}{w}$ (in.)	2ζ	$\frac{V_o^2}{2g}$ (in.)	$\frac{p_{10} - p_{12}}{w}$ (in.)	2ζ
A	0	1.120*	1.110	60.37	0.27	0.278	167.70	0.73	0.273	447.39	1.44	0.182
A	5/8	1.120*	1.110*	60.37	0.44	0.506	167.70	0.80	0.306	434.70	1.66	0.232
C	0	1.120*	1.110*	61.31	0.30	0.312	166.17	0.73	0.276	497.87	1.20	0.117

VANED ELBOW IV

		α_{11}			$\frac{p_{11} - p_{12}}{w}$	ζ		$\frac{p_{11} - p_{12}}{w}$	ζ		$\frac{p_{11} - p_{12}}{w}$	ζ
B	0	1.067	1.084	58.38	0.23	0.222	161.39	0.64	0.226	425.75	1.41	0.174
B	5/8	1.067*	1.084*	58.38	0.20	0.181	162.16	0.42	0.155	429.36	1.42	0.174
H	0	1.058	1.123	58.84	0.25	0.188	160.93	0.66	0.178	421.15	2.40	0.308
I	0	1.058*	1.068	61.55	0.12	0.109	168.80	0.35	0.121	432.21	0.91	0.124
J	0	1.058*	1.057	61.55	0.15	0.159	168.80	0.38	0.146	432.21	0.77	0.107

†Table I gives description of tunnel circuit during runs.

*Estimated.

TABLE XI

SUMMATION OF LOSS COEFFICIENTS IN PROTOTYPE TUNNEL

Element of Circuit	Form Loss Coefficient (K_o)	Friction Loss Coefficients (K_f)			
		V_o = 18 fps	V_o = 30 fps	V_o = 50 fps	V_o = 70 fps
Contraction without shaft	0.0290				
Contraction with shaft	0.0358				
Main diffuser and open-jet test section	0.1414	0.0147	0.0136	0.0125	0.0120
Closed-jet test section		0.0155	0.0140	0.0127	0.0118
Main diffuser (closed jet installed)	0.0408	0.0206	0.0190	0.0176	0.0166
Vaned elbow I	0.0156				
4-ft diam conduit	0.0030	0.0036	0.0035	0.0035	0.0035
Pump diffuser	0.0120	0.0013	0.0013	0.0013	0.0013
Vaned elbows III and IV (without shaft)	0.0034				
Vaned elbows III and IV (with shaft)	0.0042				
6-ft diam conduit		0.0012	0.0012	0.0011	0.0011
Test installation	0.0333				
Summation of loss coefficients:					
Open-jet tunnel (bare)		0.2252	0.2240	0.2228	0.2223
Open-jet tunnel (with shaft)		0.2328	0.2316	0.2304	0.2299
Closed-jet tunnel (bare)		0.1460	0.1428	0.1400	0.1381
Closed-jet tunnel (with test installation)		0.1893	0.1861	0.1832	0.1814

REFERENCES

[1] Brownell, W. F. PRELIMINARY HYDRAULIC DESIGN STUDIES FOR ALTERATIONS TO THE 24-INCH VARIABLE-PRESSURE WATER TUNNEL. Navy Department, David Taylor Model Basin, February, 1948.

[2] Purdy, Harry D. MODEL EXPERIMENTS FOR THE DESIGN OF A SIXTY-INCH WATER TUNNEL, PART I - DESCRIPTION OF APPARATUS AND TEST PROCEDURE. St. Anthony Falls Hydraulic Laboratory, University of Minnesota, Project Report No. 10, September, 1948.

[3] Ripken, John F. and Holdhusen, James S. MODEL EXPERIMENTS FOR THE DESIGN OF A SIXTY-INCH WATER TUNNEL, PART II - CONTRACTION STUDIES. St. Anthony Falls Hydraulic Laboratory, University of Minnesota, Project Report No. 11, September, 1948.

[4] Holdhusen, James S. MODEL EXPERIMENTS FOR THE DESIGN OF A SIXTY-INCH WATER TUNNEL, PART III - TEST SECTION AND CAVITATION INDEX STUDIES. St. Anthony Falls Hydraulic Laboratory, University of Minnesota, Project Report No. 12, September, 1948.

[5] Holdhusen, James S. MODEL EXPERIMENTS FOR THE DESIGN OF A SIXTY-INCH WATER TUNNEL, PART IV - DIFFUSER STUDIES. St. Anthony Falls Hydraulic Laboratory, University of Minnesota, Project Report No. 13, September, 1948.

[6] Holdhusen, James S. and Lamb, Owen P. MODEL EXPERIMENTS FOR THE DESIGN OF A SIXTY-INCH WATER TUNNEL, PART V - VANED ELBOW STUDIES. St. Anthony Falls Hydraulic Laboratory, University of Minnesota, Project Report No. 14, September, 1948.

[7] Holdhusen, James S. MODEL EXPERIMENTS FOR THE DESIGN OF A SIXTY-INCH WATER TUNNEL, PART VI - PUMP STUDIES. St. Anthony Falls Hydraulic Laboratory, University of Minnesota, Project Report No. 15, September, 1948.

[8] Silverstein, Abe. "Wake Characteristics and Determination of Profile Drag by the Momentum Method." PROCEEDINGS OF THE FIFTH INTERNATIONAL CONGRESS FOR APPLIED MECHANICS. New York: John Wiley and Sons, Inc., pp. 403-09. 1939.

[9] Tollmien, Walter. CALCULATION OF TURBULENT EXPANSION PROCESSES. NACA TM 1085, September, 1945.

[10] Corrsin, Stanley. Discussion of "Diffusion of Submerged Jets." PROCEEDINGS, American Society of Civil Engineers, Vol. 75, No. 6, pp. 912-14. June, 1949.

[11] Kuethe, Arnold M. "Investigations of the Turbulent Mixing Regions Formed by Jets." JOURNAL OF APPLIED MECHANICS, Vol. 2, No. 3, pp. A-87-A-95. September, 1935.

[12] Dryden, H. L., Schubauer, G. B., Mock, W. C., Jr., and Skramstad, H. K. MEASUREMENTS OF INTENSITY AND SCALE OF WIND-TUNNEL TURBULENCE AND THEIR RELATION TO THE CRITICAL REYNOLDS NUMBER OF SPHERES. NACA Rept 581, 1937.

[13] Hoerner, S. TESTS OF SPHERES WITH REFERENCE TO REYNOLDS NUMBER, TURBULENCE, AND SURFACE ROUGHNESS. NACA TM 777, October, 1935.

[14] Dryden, Hugh L. and Schubauer, G. B. "The Use of Damping Screens for Reduction of Wind-Tunnel Turbulence." JOURNAL OF AERONAUTICAL SCIENCES, Vol. 14, No. 4, pp. 221-28. April, 1947.

[15] Dryden, Hugh L. and Abbot, Ira H. THE DESIGN OF LOW-TURBULENCE WIND TUNNELS. NACA TN 1755, November, 1948.

[16] Corrsin, Stanley. INVESTIGATION OF FLOW IN AN AXIALLY SYMMETRICAL HEATED JET OF AIR. NACA ACR 3L23, December, 1943.

[17] Taylor, G. I. "Some Recent Developments in the Study of Turbulence." PROCEEDINGS OF THE FIFTH INTERNATIONAL CONGRESS FOR APPLIED MECHANICS. New York: John Wiley and Sons, Inc., pp. 294-310. 1939.

[18] Liepmann, Hans W. and Laufer, John. INVESTIGATIONS OF FREE TURBULENT MIXING. NACA TN 1257, August, 1947.

[19] Robertson, J. M. and Ross, Donald. WATER TUNNEL DIFFUSER FLOW STUDIES, PART I - REVIEW OF LITERATURE. Pennsylvania State College Ordnance Research Laboratory, Serial No. NOrd 7958-139, May 16, 1949.

[20] Robertson, J. M. and Ross, Donald. WATER TUNNEL DIFFUSER FLOW STUDIES, PART II - EXPERIMENTAL RESEARCH. Pennsylvania State College Ordnance Research Laboratory, Serial No. NOrd 7958-143, July 8, 1949.

[21] Peters, H. CONVERSION OF ENERGY IN CROSS-SECTIONAL DIVERGENCIES UNDER DIFFERENT CONDITIONS OF INFLOW. NACA TM 737, March, 1934.

[22] Freberg, C. R. and Kemler, E. N. AIRCRAFT VIBRATION AND FLUTTER. New York: John Wiley and Sons, Inc., 1944. p. 132.

[23] Mumma, A. G. "The Variable-Pressure Water Tunnels at the David W. Taylor Model Basin." TRANSACTIONS OF THE SOCIETY OF NAVAL ARCHITECTS AND MARINE ENGINEERS, Vol. 49, pp. 45-57. 1941.

[24] Wislicenus, G. F. FLUID MECHANICS OF TURBOMACHINERY. New York: McGraw-Hill Book Company, 1947. pp. 82 and 87.

[25] HEATING, VENTILATING, AIR CONDITIONING GUIDE. American Society of Heating and Ventilating Engineers, 1947. p. 122.